A Semiconductor Compton Camera Investigation

Thesis submitted in accordance with the requirements of the University of Liverpool for the degree of Doctor in Philosophy

by

Alexander Newton Grint

Oliver Lodge Laboratory

2009

For my Family

If nothing else works, a total pig-headed unwillingness to look facts in the face will see us through.

General Melchett

Abstract

This thesis describes the development of a Compton camera system designed to produce a 3D source image. This technique can be applied within the field of medical imaging to improve the efficiency of SPECT (Single Photon Emission Computed Tomography) scans without compromising image quality. Through improving efficiency it is proposed that either shorter patient scan times or a reduction in patient dose can be achieved.

Two Compton camera systems were investigated. The initial system consisted of two planar, double sided germanium strip SmartPET detectors. The second system substituted one of the SmartPET detectors for a double-sided silicon strip detector (DSSSD), with the intention of facilitating the scatter of low energy photons through to the absorber detector and allow images to be created.

Images were created by reconstructing incident gamma photons using the energy deposited and the position of photon interaction in each detector. Position sensitivity of the interactions is responsible for the location of the eventual reconstruction and therefore the higher the precision with which this value can be determined, the higher the quality of the resultant image.

The desire for a high degree of position sensitivity focused the initial work toward improving the position of interaction sensitivity beyond that previously achieved with the SmartPET detectors, and to attempt to improve the position of interaction sensitivity in the DSSSD beyond that of the electrical segmentation. In order to achieve this, the DSSSD and a SmartPET detector have been scanned with a 1 mm collimated source allowing the detector response as a function of interaction position to be determined. Through the application of pulse shape analysis, the depth of interaction sensitivity was improved beyond the previous limit of 4 mm toward 1 mm for the SmartPET detectors, however, excessive noise prohibited any position sensitivity refinement in the DSSSD.

Following the position sensitivity investigations, data were collected and images re-

constructed for the two Compton camera systems. Each reconstruction was localised in 3D space via two 2D images for each data set; one in the x-y plane and one in the z plane. The position resolution of each image was assessed in terms of FWHM (Full width at half maximum) and FWTM (Full Width Tenth Maximum) parameters which describe the spread of the image intensity and allow a quantitative comparison between images constructed through differing pulse shape analysis criteria.

For the dual SmartPET system, both a ^{137}Cs point source and a distributed ^{22}Na line source were reconstructed. For the ^{137}Cs source, the increased position sensitivity improved the FWHM of the image from 21 mm using the existing characterisation to 18.5 mm using the new characterisation. For the ^{22}Na line source, the 511 keV gamma ray energy was used. The new characterisation improved the FWHM from 57 mm to 50.5 mm.

For the second Compton camera investigated, a silicon strip planar detector was utilised as the system's scatter detector. Data were taken firstly using a ^{152}Eu point source and secondly a ^{137}Cs point source. For the ^{152}Eu reconstructions the new characterisation yielded the highest resolution image with a FWHM of 54 mm. For the reconstructions of the ^{137}Cs points source the original characterisation achieved the highest image resolution, with a FWHM of 24 mm.

From the experimental data taken further characterisation of the SmartPET 1 detector has been performed to improve the localisation of gamma ray interactions through the depth of the detector beyond that previously attained. This improved characterisation has been implemented in image reconstruction. For the initial system consisting of two SmartPET detectors, the latest depth characterisation has been shown to improve the image resolution beyond that previously achievable. For the DSSSD/SmartPET system the characterisation was less successful. This is assumed to be due to low experimental statistics and high levels of noise present in the DSSSD. Furthermore, the motivation for introducing the silicon detector was to facilitate low energy Compton imaging; this goal was unobtainable with the noise levels present in the detector.

Acknowledgments

Firstly, thanks to Prof. P.J. Nolan for allowing me to carry out this research at the University of Liverpool.

Thanks to Dr. Andy Boston for his supervision and patience during my time as a PhD student and to Dr. Helen Boston for her help and advice, especially in the lab.

Thanks to the EPSRC, for providing the necessary financial support for this research project and the funds to visit laboratories around the world.

I would like to acknowledge all collaborators involved in this research, in particular Tom Davinson at the University of Edinburgh for the loan of his DSSSD and RAL preamps in my hour of need. I would also like to thank Sami Rinta-Antila and Dave Wells for their hard work and expertise which were much needed to get the DSSSD operational. I'd also like to acknowledge our antipodean associates John Gillam and Toby Beveridge at Monash University for much needed imaging advice and discussions - good on ya fella's. Thanks are also due to the IT support, Dr. John Cresswell, Ms. J. Sampson and Mr. M. Norman.

Thanks to fellow students and postdocs for their friendship during my time; Craig Gray-Jones, Jimmy, Danielle, Gerard, Andy Mather, Barry McGuirk, Ste Moon, Heidi, Harkness, Gez, Fay, Phillipos, Pete, Petts, Sapple, Carl, Mike, John, Ed and to the Scheck (who iz zis person?).

Thanks to those fellow footballers, from the glory days of CMP vs Nuclear to wednesday nights at Archbishop, in particular Si Lee, Mick, Ben Fowler, Carlos Chavez, Herring, Bowfield and Gallagher.

I would also like to give and extra mention to the following without whom my time in Liverpool wouldn't have been the same...

- Reggie, my house mate for several years which resulted in a surge in local hob nob and milkshake sales and a full Donald. This cat was also present on numerous PhD excursions to many far reaching places including Australia and Vancouver, (where he foolishly claimed he could train a Beluga whale with ease; for the

record, no you couldn't lad!).

- Matt Dimmock, who accompanied me to many a morning gym sesh. Never has any man spent so long claiming to be "just coming through the door now". I must also thank Matt for all the help he provided me with during my time, from MT sort to DAQ - much appreciated lad.

- Scraggo, who's unique take on life can never be predicted. Remember the green chairs? Here's to sun, tranquility and olive trees.

- Al Brownrigg, my housemate for the final few months and the most feared man throughout the 5-a-side community. Close shave that lad, give my regards to the Gentleman.

- Dave Oxley, Thanks for the discussions and friendship throughout, the films, the massive pizzas and our liberating trip to the beach.

- Ben Peitras, for ROOT aid and, along with Martin Jones, provided occasional accommodation, lively (Martin!) discussions, friendship and beers. ROCK!

I'd especially like to thank Laura for all your love and support throughout, for which i'll be forever grateful. Thanks also for your coding skills, which saved the day on many occasions! And to Emma; Cool beans.

Finally I'd like to thank my family, my Mum and Dad for all their encouragement and support from day one, it will always be appreciated, and my brother Chris.

COYBB!

Contents

List of Figures

List of Tables

Chapter 1

Introduction

1.1 Nuclear Medicine

Nuclear medicine is a branch of treatment that administers radioactive material to the patient to diagnose or treat a variety of diseases. Nuclear medical imaging techniques allow diagnosis to be performed by creating an image of internal parts of the body. This is achieved by administering a radioactive tracer (radiotracer) to the patient which, over a specific period of time, will accumulate in the organ or the area of the body to be imaged. The gamma radiation emitted from the radiotracer is subsequently detected using a multitude of detector and software techniques and an image is created.

Imaging techniques are generally considered to belong to one of two imaging modalities, functional or structural. Structural imaging methods, such as CT scans, provide extremely accurate anatomical images but provide no information regarding the functioning of the organ or tissue of interest. Knowledge of the organ or tissue function can prove to be crucial both in obtaining an accurate diagnosis and in prescribing the most suitable treatment. Nuclear imaging is known as a functional imaging modality, meaning it provides important details regarding the functioning of the target organ or tissue. It is usually used to complement a structural image by providing information

not present in the structural image, such as; tumour metabolism, aneurysms (weak spots in blood vessel walls), irregular or inadequate blood flow to various tissues, blood cell disorders and inadequate functioning of organs.

Two prominent nuclear imaging techniques are positron emission tomography (PET) and single photon emission computed tomography (SPECT), which use different properties of radioactive isotopes to create an image [Web88].

1.1.1 Positron Emission Tomography (PET)

PET scans involve the administration of a radiotracer which undergoes positron decay. The subsequent annihilation of the positron results in the emission of two coincident 511 keV gamma ray photons, which are emitted at an angle of 180^0 with respect to each other. The detection of these coincident events allow an image to be created from the reconstructed lines of response from many events providing 3D radiotracer maps.

1.1.2 Single Photon Emission Computed Tomography (SPECT)

SPECT scans use radiotracers which associate only one gamma emission with each decay. A 3D image is created by rotating the collimated detector to acquire a 360^0 profile of the patient by collecting data at many angular intervals. The detector (typically a scintillator, such as sodium iodide), is collimated so that only those events whose trajectory from the source is parallel to the collimated holes are detected, and so provide directional sensitivity. As all detected photons are parallel to the collimator, lines of response can be generated for each position datum recorded about the patient and a 3D image of the distributed source can be generated.

1.2 Semiconductor Compton Camera - Project outline

This research is a development of the SmartPET (Small Animal Reconstruction Tomograph for Positron Emission Tomography) system. This was designed as a proof of principle for the application of high purity germanium (HPGe) detectors to small animal imaging by operating as a dual head PET camera. This work was presented in the theses of Mather [Mat06] and Cooper [Coo07]. The system can be easily arranged to operate in SPECT configuration, where the use of cone beam reconstruction techniques, provides electronic collimation. A system which operates in such a fashion is known as a Compton camera. The original proposal applying this technique to medical imaging is documented in [Tod74]. This removes the requirement for a mechanical collimator currently required in commercial SPECT systems. Therefore there is the potential to vastly increase the efficiency of the system, while the excellent energy resolution of germanium detectors provides the opportunity for multi-tracer SPECT studies [Sin83].

Previous work to characterise the SmartPET detectors was presented in the thesis of Turk [Tur06] and previous research using the SmartPET detectors as a Compton camera was presented in the thesis of Gillam [Gil06] and Scraggs [Scr07]. Limitations observed were that the thickness of a SmartPET detector is prohibitive for a low energy Compton camera study, i.e. for photon energies similar to those currently used in SPECT scans (141 keV), and that the localisation of a photon interaction within the detectors was limited to a volume of $1 \times 1 \times 4$ mm^3.

The principal aims of the work presented in this thesis are as follows:-

- To improve the 4mm localisation of a photon interaction through the depth. This was be done by acquiring and analysing characterisation data for the SmartPET 1 detector and is discussed in Chapter Four.

- To quantify the effect of this improved depth localisation on image quality. Details of the effect on image quality are presented in chapter five, where Compton camera data was collected for both a point and distributed radiation source using the two SmartPET detectors.

- To collect Compton camera data at low photon energies by the introduction of a thin, double-sided silicon strip detector (DSSSD).

- Evaluate the performance of the system based on the experimental measurements taken and analysis performed and use this evaluation to make recommendations for future work.

Chapter 2

SPECT

2.1 Gamma Camera

2.1.1 Background

Single photon emission computed tomography (SPECT) is the method by which a 3D image of a distributed radiation source within the body is created. The modern detection system has been developed over the years from the original idea by Hal Anger [Ang58]. The basic detection system consists of a parallel hole collimator masking several scintillators, which are coupled to an array of photomultipliers and is known as a *Gamma camera.* The use of a parallel hole collimator together with a multitude of photomultiplier tubes, allows a degree of position sensitivity to be assigned to the γ-ray interaction, and a 2D image of the radiation source can be created. To obtain a 3D image, the detection system is rotated to cover 360 degrees around the subject, acquiring 2D images from multiple angles. These are usually at 2 degree increments through the full 360 degree range about the patient. The 3D image is subsequently generated by applying a tomographic reconstruction algorithm to the many 2D images. The presence of a collimator greatly reduces the efficiency of the system, where it is commonly observed that only about 1 in 10,000 emitted photons are detected during a SPECT scan [Wer04a]. The spatial resolution of the image is largely a result of

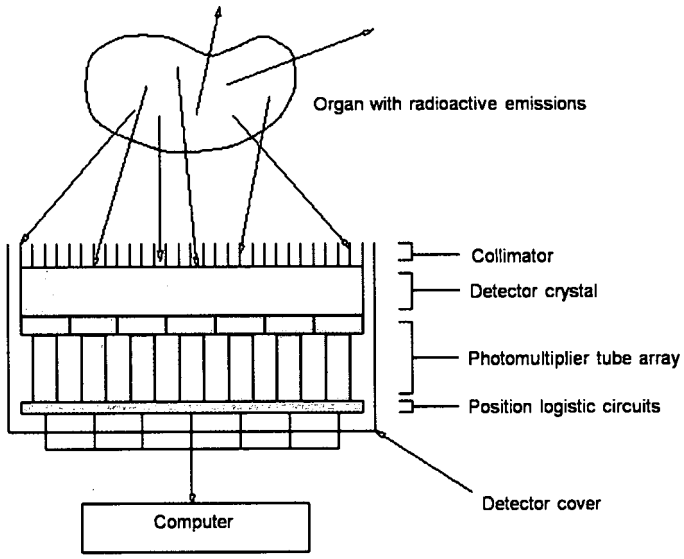

Figure 2.1: Diagram of a conventional Gamma camera. The collimator ensures that gamma rays detected correspond to a source position parallel to the collimator apertures. The Gamma camera system is then rotated 360 degrees about the patient to create a 3D reconstruction of the source image which represents the location and distribution of radiotracer within the patient.

the collimator dimensions and is currently around 7mm FWHM. This figure is based on detecting 141 keV photons, a collimator hole diameter of 1.2 mm and the source located at 20 cm from the collimator [Wer04b].

Both SPECT and PET scans are considered as *functional imaging modalities*, distinguishing them from other imaging modalities such as X-ray CT which primarily depict the body's anatomical structure. Functional imaging modalities image aspects of the body's physiology by representing the spatial distribution of properties such as glucose metabolism, blood flow and receptor concentrations. This allows SPECT and PET to detect tumours, locate areas of the heart affected by coronary artery disease and identify brain regions influenced by drugs providing invaluable diagnostic information compared to non-functional imaging.

The isotope of choice currently used in hospitals to perform SPECT scans is ^{99m}Tc, which emits γ-ray photons of energy 141 keV. It is inexpensive, easily produced and readily available from ^{99}Mo generators, which are generally located on the hospital site. ^{99m}Tc activities typically range from 500 to a 1000 MBq. SPECT has the potential for multiple tracers to be used. These are useful for a wider variety of functional study during the same scan by tagging different isotopes to different tracers which in turn target different organs and tissues. It may also be desirable to use isotopes with longer half lives in parts of the world where access to a ^{99}Mo generator is limited. Most other nuclides which are commonly used generally emit higher γ energies. These higher energies are less subject to scatter and attenuation prior to detection. However, in order to use higher energy isotopes with the current SPECT systems, the collimator must be altered by increasing both its thickness and the separation between collimator apertures to ensure only photons with a trajectory parallel to the collimator apertures are detected. This results in an unwanted reduction in the sensitivity of the procedure. The 141 keV γ-rays are easily stopped by lead, meaning thinner collimators with more apertures can be used effectively, thereby increasing the efficiency of a particular scan.

It is desirable for the SPECT imaging system to have both improved sensitivity for conventional ^{99m}Tc scans and the facility to use higher energy isotopes without a further loss in efficiency. A proposed solution to this problem is the implementation of *electronic collimation*, known as a Compton camera, making the need for a mechanical collimator obsolete. The sensitivity gain has been estimated to be as much as between two and three orders of magnitude, depending on the incident photon energy, when compared with equivalent collimated systems [Mih04]. A Compton camera is also capable of producing a 3D image without the need for rotation about the subject, which can degrade the image through rotation orbit misalignments.

2.2 Compton Camera

The application of the electronic collimation concept to medicine was first proposed by Todd in 1974 [Tod74]. The basic method requires that the incident photon undergo at least two interactions in the detection system; a Compton scatter followed by a photoelectric absorption. The Compton camera described in this paper consists of two energy and position sensitive planar detectors. The detectors are arranged one behind the other, with the detector closest to the source labeled the *scatter* detector, and behind, the *absorber* detector. The creation of a 3D image from the Compton camera requires gamma ray photons emitted from the source with an energy, E_0, to Compton scatter through the scatter detector, depositing a finite energy, E_1, and be fully absorbed by the absorber detector, depositing the remainder of its energy, E_2, and so E_0 is equal to the sum of the two deposited energies. The image is reconstructed by creating a cone, projected in the direction of the source, where the perimeter of the cone base provides all the possible locations of the gamma ray, shown as the dashed ring in Figure 2.2. Ultimately an image will be created by performing this cone reconstruction for many events, with the source said to be located at the area containing the greatest overlap of cone base perimeters (Figure 2.3).

The cone angle is double the angle of scatter. The scatter angle is calculated by introducing the energy deposited by the scatter (E_1) and the scattered photon energy deposited in the absorber (E_2), to the Compton scatter formula, Eqn 2.1

$$cos\theta = 1 - m_0c^2\left(\frac{1}{E_2} - \frac{1}{E_1+E_2}\right) \tag{2.1}$$

where m_0c^2 is the rest mass energy of the electron (0.511 MeV).

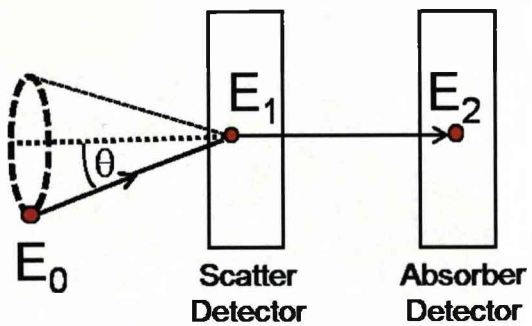

Figure 2.2: Diagram to describe the creation of a reconstruction cone from a single gamma ray photon. The gamma ray is emitted from a source with an energy E_0, Compton scatters through the scatter detector depositing an energy E_1 and is absorbed in the absorber detector, where the remainder of its energy is deposited, E_2. The two deposited energies are then used to calculate the angle of scatter which is half the angle of the reconstruction cone apex. The positions of the interaction are responsible for the direction and location of the reconstructed cone. The perimeter of the cone base provides all the possible source locations which could have produced the interactions recorded in the detectors. An image is created from many events being reconstructed, with the source assigned to the position of most common overlap of the cone base perimeters, as illustrated in Figure 2.3.

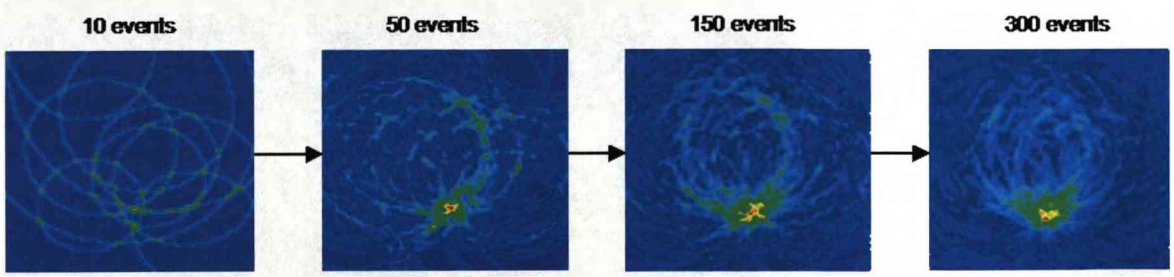

Figure 2.3: Cone beam reconstructions showing increasing localisation of the source as number of events used increases [Los05].

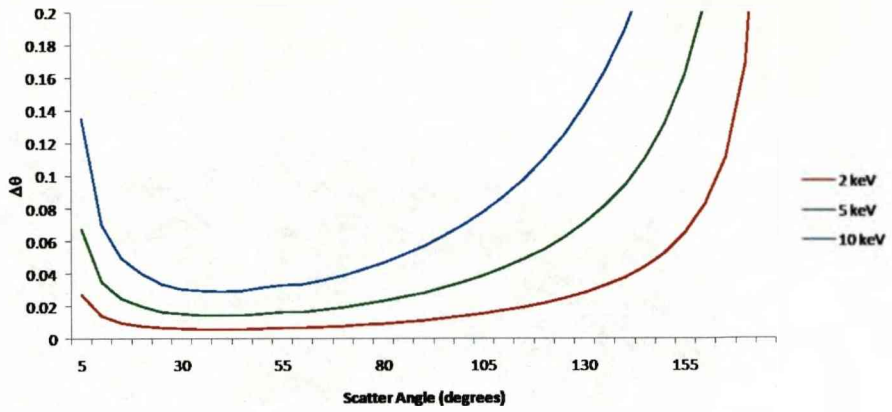

Figure 2.4: Contribution to the angular uncertainty of a scatter from a 140 keV γ-ray due to the finite energy resolution (2 keV, 5 keV and 10 keV) of the scatter detector.

2.2.1 Factors affecting Compton camera image quality

There are several factors which govern the quality of image produced by a Compton camera. The principle effect of any factor is to alter the uncertainty with which either the angle of scatter is calculated, which will contribute to uncertainty in the position of the cone base, or to reduce the accuracy with which the reconstructed cone is positioned and directed. Both of these effects will result in blurring of the final image. Uncertainty associated with the scatter detector determination arises from independent contributions of;

Energy resolution of the scatter detector

From equation 2.1 it can be seen that the energy deposited in the scatter detector, E_1 is used to calculate the angle through which the photon has scattered. Uncertainty in this energy deposition will manifest itself as uncertainty in the calculated scatter angle. Figure 2.4 is a plot of the angular uncertainty as a function of scatter angle for three hypothetical detector resolutions for an incident photon energy of 662 keV. Detector energy resolution is discussed in Chapter Three.

The Doppler broadening effect

The Doppler effect [Ord98], arises because the bound atomic electron from which the gamma ray scatters is not at rest, as assumed in equation 2.1, causing a dispersion of the deposited energy. For low energy incident photons, i.e. energies of up to a few 100 keV, the Doppler broadening effect gives a high uncertainty in the measurement of the incident photon scatter angle, which often dominates over the uncertainty due to energy and position measurement errors of the detectors. This uncertainty is reduced by increasing the photon energy and decreasing atomic number of the scatter detector.

The system geometry

The geometry of the system also contributes to the observed angular uncertainty. The geometry of the system refers to the source to scatter detector distance and also the detector separation. In general, increasing the distance of both variables reduces the angular uncertainty [Ord99]. However, increasing the distances between detectors also decreases the solid angle of the absorber subtended by the scatterer, and decreases Compton efficiency, an important consideration when developing a Compton camera.

The position of interaction sensitivity

The final primary contributor to the angular uncertainty is the uncertainty in the locations of the initial Compton scattering event in the scatter detector and the subsequent scatter in the absorber detector. The interaction locations are responsible for defining the position and direction of the axis about which the reconstructed cone will be situated and as such will have a significant impact on the resolution achievable in the final image [Ord99]. Chapter Four describes the acquisition and analysis of experimental data to improve the position sensitivity of the detector beyond the current limit.

Chapter 3

Principles of Radiation Detection

3.1 Interactions of γ rays with matter

Knowledge of γ ray interaction processes in matter is required to understand detector response. Most interactions are due to one of three mechanisms [Dav52]: (1) The photoelectric effect, (2) Compton scattering and (3) Pair production.

3.1.1 Photoelectric Effect

The photoelectric effect is the most common interaction in germanium for incident photons with energies less than 200 keV. During the process, the energy of the incident photon is totally transferred to a bound atomic electron (usually in the K - shell) and a photoelectron is produced with an energy(E_e) equal to

$$E_e = E_\gamma - E_b, \tag{3.1}$$

where E_γ is the energy of the incident photon and E_b is the binding energy of the atomic electron (E_b =12 keV for germanium and 2 keV for silicon). The probability of the photoelectric effect occurring for a photon of a given energy is approximately

$$P_{Photoelectric} = constant \times \frac{Z^n}{{E_\gamma}^{3.5}} \tag{3.2}$$

where n varies between 4 or 5.

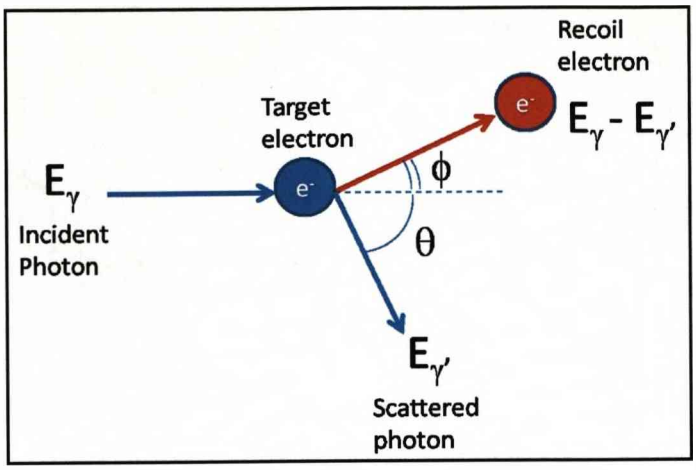

Figure 3.1: Schematic of a photon scattering through an angle θ, transferring some of its energy to the electron, which subsequently recoils through an angle ϕ

3.1.2 Compton Scattering

Compton scattering takes place between the incident γ ray photon and an electron in the absorbing material. An illustration of the Compton scattering process is shown in Figure 3.1. In germanium, Compton scattering is the dominant interaction for photon energies of approximately 200 keV to 2 MeV, with the probability of γ ray photons interacting via the Compton scattering process increasing linearly with Z. The incident photon transfers some of its energy to the electron and is deflected through an angle θ with respect to its original direction.

The energy of the scattered γ ray (E_γ') can be calculated using the Compton scattering formula:

$$E_\gamma{}' = \frac{E_\gamma}{1 - \frac{E_\gamma}{m_0c^2}(1 - cos\theta)} \tag{3.3}$$

where E_γ is the energy of the incident γ ray, θ is the angle through which the γ ray is scattered and m_0c^2 is the rest mass energy of the electron (0.511 MeV). The angular distribution of scattered gamma rays is predicted by the *Klein-Nishina*

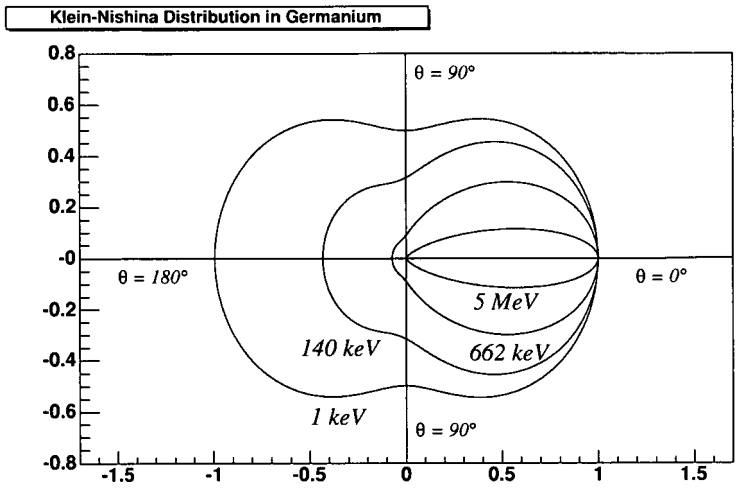

Figure 3.2: A polar plot of the scattering profile for a range of photon energies, incident from the left.

formula [Kno00] for the differential scattering cross section $d\sigma/d\Omega$:

$$\frac{d_\sigma}{d_\Omega} = Z{r_0}^2 \left(\frac{1}{1+\alpha(1-cos\theta)}\right)^2 \left(\frac{1+cos^2\theta}{2}\right) \left(1+\frac{\alpha^2(1-cos\theta)^2}{(1+cos^2\theta)[1+\alpha(1-cos\theta)]}\right) \quad (3.4)$$

where $\alpha \equiv h\nu m_0 c^2$ and r_0 is the classical electron radius. The Klein-Nishina profile is shown graphically in Figure 3.3 for a range of gamma energies incident on germanium. It shows that the higher the energy of the incident gamma photon, the greater the probability of scattering in the forward direction.

3.1.3 Pair Production

Pair Production is the process by which an incident photon creates an electron-positron pair in the coulomb field of an atomic nucleus. The subsequent annihilation of the positron with a free electron results in the emission of two 511 keV gamma rays at an angle of 180 degrees with respect to each other. In order for this process to be energetically feasible the incident gamma photon must have at least 1022 keV (i.e. twice the rest mass of an electron), with any energy over this value shared between the electron-positron pair as kinetic energy. The probability of this reaction however,

remains very low until the energy of the gamma photon approaches the order of a few MeV.

3.1.4 Linear Attenuation

The three interaction processes described above are the predominant methods by which a photon is attenuated in a medium. The total interaction cross section of a photon is the sum of the cross sections from each of the three interaction processes:

$$\sigma_{Total} = \sigma_{PE} + \sigma_{CS} + \sigma_{PP} \tag{3.5}$$

To determine the number of incident photons that will traverse a given material, one must first calculate the linear attenuation coefficient, μ. This is the product of the total interaction cross section (eqn 3.6) and the density of atoms in the material.

$$\mu = N\sigma_{Total} = \left(\frac{N_A \rho}{A}\right) \sigma_{Total} \tag{3.6}$$

where N_A is Avagadro's number, ρ the material density and A the atomic weight. This linear attenuation coefficient can now be used (eqn 3.7) to calculate the fraction of photons incident on a material that will penetrate through,

$$I = I_0 e^{-\mu t}. \tag{3.7}$$

3.2 Basic Semiconductor Physics

The selection of solid state detectors for gamma-ray spectroscopy applications rather than gas based devices is primarily due to the increased density offering a greater efficiency for gamma-ray detection. Solid state detectors are commonly either scintillator or semiconductor material. While scintillators generally posses a greater efficiency for stopping gamma rays, semiconductors provide vastly superior energy resolution, confirming them as the material of choice in the field of gamma-ray spectroscopy.

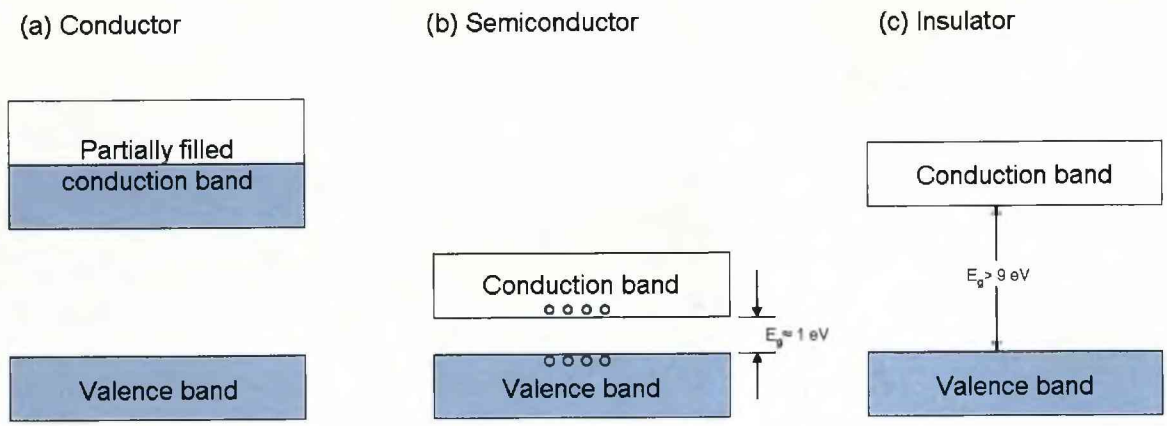

Figure 3.3: Diagram illustrating energy band gap theory for (a) conductors, (b) semiconductors and (c) insulators [Sze01].

Solid materials are commonly described by their electrical conductivity properties, grouping them as either a conductor, a semiconductor or an insulator. The band theory of solids is used to understand the difference between these three groups. The periodic lattice present in crystalline materials will only support certain values of quantised electron momenta, hence certain values of electron energy, giving rise to an energy band structure containing bands of allowed energies and bands of forbidden energies.

The valence band is the highest filled energy band at 0 K and the conduction band is the first allowed band above the valance band. For conduction to occur an electron must be able to move within the conduction band (i.e. the conduction band is not empty), or from the valence band to the conduction band, upon the application of an electric field. In a conductor the bands either overlap or are adjacent to each other, so even small values of electric fields can provide enough energy to promote the electrons into higher states, where they will be available for conduction.

In the case of insulators and semiconductors, at 0K the valence band is full and the conduction band is empty. These bands are separated by an energy gap (E_g) between

the valence band and the conduction band, containing forbidden energy levels. It is the magnitude of this energy gap that generally determines whether a material is classed as an insulator or a semiconductor. For semiconductors E_g is usually of the order of 1 eV (e.g. 0.67 eV for germanium and 1.12 eV for silicon) at room temperature, whereas for insulators, E_g values of 4 eV and above are typical. At low temperatures semiconductors behave like insulators, however at higher temperatures some electrons can be thermally excited into the conduction band which is observed as leakage current. The promotion of an electron from the valence band to the conduction band leaves an empty energy level in the valence band. This empty energy level is known as a *hole* which also takes part in conduction as a positive charge carrier. Electrons and holes flow in opposite directions in an electric field, though they contribute to current in the same direction since they are oppositely charged.

3.2.1 Semiconductor Doping

An *intrinsic* semiconductor is pure enough that any impurities that happen to be present do not appreciably effect its electrical behaviour by changing the number of charge carriers available for conduction. In this case, all carriers are created due to thermally excited electrons (in the absence of ionising radiation), from the full valence band into the empty conduction band. Therefore equal numbers of electrons and holes are present in an intrinsic semiconductor. In an intrinsic semiconductor, the Fermi level lies in the centre (at $T = 0\,K$) of the energy gap. At higher temperatures, some electrons have enough energy to cross the energy gap E_g, and subsequently take part in conduction. To alter the energy needed for conduction to take place, impurities, known as dopants, can be added to the crystal lattice. Semiconductors that have had impurities added to them are known as *extrinsic* semiconductors. Dopants can either:-

- Provide electrons which sit in an energy level just below the conduction band. Less energy is needed to promote an electron to the conduction band and so conductivity increases. Impurity atoms which do this are known as *donors* and

semiconductors with these electron donating impurities are known as *n-type* semiconductors.

- Provide vacant energy levels just above the full valence band. Less energy is needed to excite an electron from the valence band to this energy level and so conductivity increases. Impurity atoms which do this are known as *acceptors* and semiconductors with these electron accepting impurities are known as *p-type* semiconductors.

Two commonly employed semiconductors, silicon and germanium, belong to group IV of the periodic table. To dope these semiconductors, one would need to add atoms which either donate electrons (which lie just below the conduction band) or provide *holes* (which lie just above the valance band). Atoms which donate electrons have a spare electron after being covalently bonded to the other semiconductor atoms in the lattice (taking the place of a semiconductor atom in the lattice). These donating atoms are typically provided by elements from group V of the periodic table (e.g. phosphorous). Similarly, atoms which introduce holes to the lattice have one less electron than the semiconductor atoms, and so one of the covalent bonds between the dopant atom and the semiconductor atoms is created by a single electron. These atoms are usually group III elements (e.g. boron).

3.2.2 The p-n Junction

The p-n junction is the fundamental element of all semiconductor detectors and is formed when a p-type and n-type semiconductor meet in good thermodynamic contact. Its main electrical property is that it rectifies, i.e. allows current to flow easily in one direction only. At the junction between the two materials, there is a net diffusion of electrons from the n-type region of high electron concentration to the p-type region of low electron concentration. The electrons from the n-type material and holes in the p-type material combine creating a net positive space charge on the

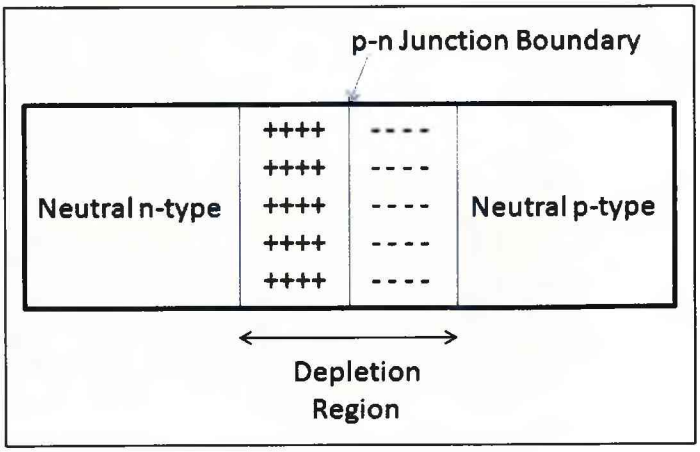

Figure 3.4: Illustration of the space charge regions created in a p-n junction at thermal equilibrium.

n-type side and a net negative space charge on the p-type side, as shown in Figure 3.4. For HPGe detectors, the crystal is cut from a zone-refined high purity crystal that has a given impurity gradient. Whether the crystal is mildly p-type or n-type depends on the section from which the detector crystal is cut. The p-n junction is formed at the boundary between the crystal and its opposingly doped contact.

This volume of space charge depleted of free charge carriers is termed the depletion region, and extends into both sides of the junction. The interaction of gamma rays in the small depletion region of the junction results in the generation of charge carriers in the form of electron-hole pairs. However, the electric field is not sufficient to prevent trapping and recombination. For a semiconductor to operate as a radiation detector the charge carriers created by an interaction must be collected. In order to be able to discriminate between interactions of differing energy the charge collected must be proportional to the energy deposited by the interaction. To satisfy these statements, a semiconductor must be operated in such a way that the charge liberated by an interaction in the depletion region is collected as efficiently as possible, minimising the possibility of charge trapping and recombination. This can be achieved by applying

a *reverse bias* to the detector by either:

- A negative voltage applied to the p-type side. This attracts the free holes to the p-type contact away from the junction, pushing the negative electrons away from the p-type side.

- A positive voltage applied to the type n-type side. This attracts the free electrons away from the junction, pushing the positive holes away from the p-type side.

This application of a reverse bias voltage to the diode increases the width of the depletion region and little if any current can exist. The higher the reverse voltage the wider the depletion region becomes. The width of the depletion region in a typical semiconductor detector can be calculated using equation 3.8,

$$d = \sqrt{\left(\frac{2\epsilon V}{eN}\right)}, \tag{3.8}$$

where d is the depletion region width, ϵ is the dielectric constant of the semiconductor material, V is the reverse bias voltage applied, e is the electronic charge and N is the acceptor or donor concentration in the bulk material. It can be seen from equation 3.8 that to achieve large depletion widths, and therefore larger detecting volumes, it would be desirable for the applied voltage, V, to be large and for N to be small, i.e. the material must be of high purity. Ionising radiation interacting in this depletion region will create free electron-hole pairs, which will be swept to the detector contacts under the influence of the electric field.

3.2.3 Charge Carrier Production

The photoelectron resulting from the photon interactions described earlier can lose energy through two processes; collision ionisation and/or radiative emission, such as Bremsstrahlung.

$$\frac{dE}{dx_{Total}} = \left(\frac{dE}{dx}\right)_{Coll} + \left(\frac{dE}{dx}\right)_{Rad}. \tag{3.9}$$

These processes result in the creation of secondary charged particles that generate the detector response (e.g. electron-hole pairs in semiconductors). The energy loss of the photoelectron can be described by the sum of the two processes (eqn 3.9). Bremsstrahlung emission produces photons of 10 keV which will likely be absorbed via the photoelectric effect close to the site of interaction. Generally, electrons resulting from photon energies <1 MeV will have a range of 1 mm and lose energy predominantly through collision ionisations. The energy loss due to collision ionisations can be described as a function of its path length by the Bethe-Block formula [Leo93].

The number of secondary charged particles generated has a direct effect on the signal to noise ratio of a spectrometer. Because of this, an important parameter for semiconductor detectors is the average energy required to make one electron-hole pair, ϵ_{pair}. For Germanium and Silicon ϵ_{pair} ~2.96 eV and ~3.76 eV respectively. The number of electron-hole pairs, N_{pair}, created per absorbed photon, with energy E_γ, is given by,

$$N_{pair} = \frac{E_\gamma}{\epsilon_{pair}}. \tag{3.10}$$

Experimentally, the statistical spread in the number of electron-hole pairs produced differs from that of simple Poisson statistics. This is because Poisson statistics assume independent events, however in the process of charge carrier formation, the creation of one electron-hole pair is responsible for the creation of another, and so it can no longer be assumed that the events are independent. The Fano factor (F) [Fan47] was introduced to account for this deviation and is given by,

$$\Delta N_{pair} = \sqrt{F N_{pair}} = \sqrt{F \frac{E_\gamma}{\epsilon_{pair}}}. \tag{3.11}$$

The Fano factor is estimated ~0.08 for germanium [Peh69] and between 0.085 and 0.137 for silicon [Zul70] at 77 K.

3.2.4 Energy Resolution

Both germanium and silicon detectors exhibit energy resolution superior to that of most detectors manufactured from other materials. In particular, germanium energy resolution is typically between 1.7 - 2.3 keV FWHM for an incident gamma ray energy of 1332 keV [Kno00]. Silicon is less proficient, generally providing energy resolution in the region of approximately 3 percent. The spectroscopic performance of germanium is due to a higher number of charge carriers produced per unit of deposited energy, as the average energy required to produce a charge carrier pair (ϵ_{pair}) is 2.96 eV. This means that more charge carriers are produced per event when compared to other devices, reducing the contribution of statistical fluctuations to the FWHM value. For silicon, ϵ_{pair} is 3.76 eV, which, although higher than the corresponding value for germanium, it is still low enough to have a spectral advantage over many other detectors. The intrinsic spectroscopic energy resolution ($\Delta {E_{int}}^2$), of a semiconductor can be calculated using equation 3.12, where the three factors which contribute to spectral broadening are summed in quadrature,

$$\Delta {E_{int}}^2 = \Delta {E_D}^2 + \Delta {E_X}^2 + \Delta {E_E}^2. \tag{3.12}$$

The term $\Delta {E_D}^2$, represents the peak width observed due to the fluctuations in the number of charge carriers created per interaction, $\Delta {E_X}^2$ accounts for incomplete charge collection and $\Delta {E_E}^2$ represents the contribution from electronic noise arising either in the detector, (such as surface leakage, bulk leakage or Johnson noise), or in the associated pulse processing circuitry post detection.

3.2.5 Signal Generation

The signals observed from a photon interaction in a semiconductor are generated as the electron and hole charge clouds are swept from the interaction position to the contacts. The charge clouds move under the influence of the electric field, due to the reverse bias applied to the detector contacts. The arrival of charge at a contact induces a signal measured via a charge sensitive preamplifier. The pulse is characterised by a quick leading edge, corresponding to the charge collection time, and a long fall time, corresponding to the discharge of the preamplifier. The height of the pulse is proportional to the amount of charge collected. The structure of the observed pulse results from two processes:

- Collection of the charge carriers as they arrive at the contact.
- Induced charge due to the charge cloud moving within the vicinity of the contact.

The collection of the charge carriers corresponds to the steepest part of the pulse slope [Mih04], and is uniform across all contacts of the same bias (i.e. for contacts collecting the same charge carriers, electrons or holes). The induced components of the pulse however, are not uniform but vary as a function of distance from the collecting contact. The total charge induced on an electrode by a moving point charge can be determined as a function of instantaneous position of the moving charge within the detector. This was originally done by calculating the instantaneous electric field at each point of the moving charge's trajectory and integrating the normal component of the electric field over the surface of the electrode. To attain good precision with this method, one would need to use a large number of points along the point charge's trajectory. This laborious procedure can be avoided by using a simpler method of calculating the charge induced on an electrode which was developed, independently, by Shockley [Sho38] and Ramo [Ram39]. The instantaneous value of the induced current, i(t), from a point charge, q, moving in an electric field $E_{(x)}$, is given by

$$i(t) = q\frac{E_{(x)}v_d(x,t)}{V_{(x)}}, \tag{3.13}$$

where $V_{(x)}$ is the electric potential, v_d is the drift velocity of the charge carriers, which is dependant on the carrier mobility and the electric field strength. In order to calculate the induced current in a multi electrode device, such as a semiconductor strip detector, Green's reciprocity theorem must be applied. This theorem is an extension to that of Shockley and Ramo and introduces the hypothetical concept of the weighting field, allowing the relationship of the electrostatic coupling between the moving point charge and the electrode of interest to be quantified. Using Green's reciprocity theorem, the induced charge measured at an electrode can be calculated by

$$i(t) = qE_w v_d(x,t) \tag{3.14}$$

where E_w is the weighting field.

Current is induced at the electrodes by the Coulomb fields which emanate from each charge cloud. The Coulomb fields are not homogeneous and as the charge cloud moves through the detector volume, the strength of the Coulomb field at the electrodes varies, as can be seen in Figure 3.5. This results in differing amounts of charge induced from each charge carrier at different times throughout the charge collection. This means that the shape of the pulse created from the charge collection will vary depending on the distance of the charge cloud creation from the electrodes, as described by the plots situated at the bottom of Figure 3.5. These observations form the basis of the analysis in Chapter Four with the aim of calibrating the position of interaction through the depth of a the SmartPET planar detector from the analysis of the pulse shape.

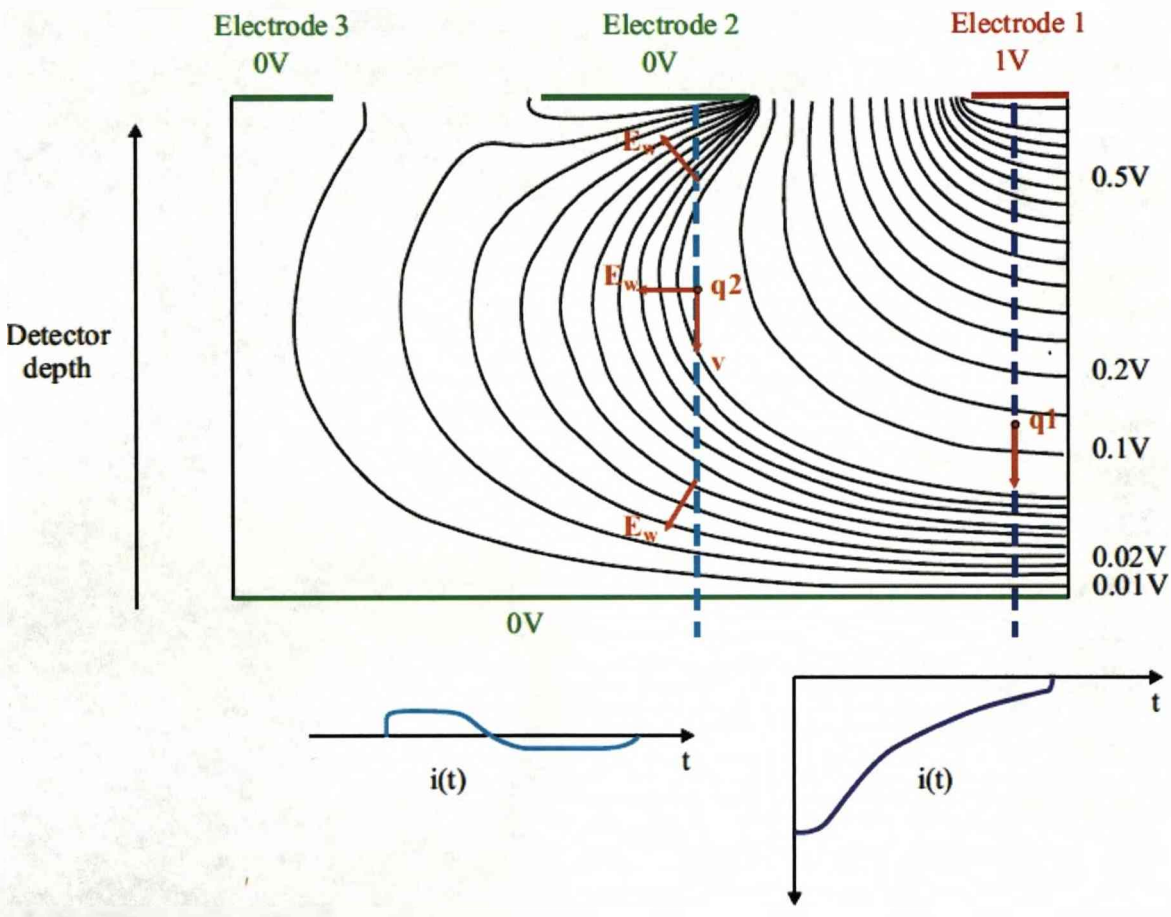

Figure 3.5: The weighting potential distribution for a multi electrode planar HPGe detector [Rad88]. The potential surfaces are represented by the black lines with the spacing between the lines denoting the potential of the gradient. Electrode 1 is at unity and all other electrodes are grounded. q1 and q2 are charges resulting from interactions at those positions. The plots show the current induced on electrode 1 by the subsequent movement of these charges to their collecting electrodes.

3.3 Application of Semiconductor Detectors

In this thesis two types of semiconductor material, germanium and silicon, are investigated and implemented in Compton camera measurements.

3.3.1 Germanium

Germanium is a commonly used semiconductor in gamma ray spectroscopy applications due to its excellent energy resolution and reasonable efficiency. It belongs to group IV of the periodic table and has an atomic number (Z) of 32 and has a face centered cubic structure. It has a small band gap ($\sim$0.67 eV) and as a result requires cooling to cryogenic temperatures (77 K) to operate as a γ ray detector.

3.3.2 Silicon

Silicon also belongs to group IV of the periodic table and, as with germanium, exhibits a face centered cubic structure. Silicon is more commonly associated with charged particle detection rather than gamma ray detection. Its lower density, (Z=14), and poorer energy resolution than that of germanium make it a less popular material for general gamma ray spectroscopy. However, when implemented as a the scatter detector in a low energy Compton camera measurement, silicon can be a competitive alternative to germanium. At low gamma energies (of the order of 100 keV), silicon can display superior energy resolution due to the reduced contribution from Doppler broadening [Ord98] where the FWHM of the Doppler-broadened energy spectrum corresponding to 45^0 scatters of 141 keV photons is 1.39 keV for germanium and 0.93 keV in silicon. Its lower density also acts in its favour as the Compton scattering cross section for low energy photons is higher. This increases the probability of the photons scattering through the scatter detector allowing them to reach the absorber, as opposed to photoelectric absorption in a higher density scatter detector such as germanium. Couple these facts with the ability to operate at room temperature, silicon

has the potential to become the semiconductor of choice for a low energy Compton camera. General properties of germanium and silicon are summarised in table 3.1.

Property	Germanium	Silicon
Atomic Number Z	32	14
Atomic Mass A	72.6	28.1
Stable Isotope Mass Numbers	70-72-73-74-76	28-29-30
Atoms /cm^2	4.41 $\times 10^{22}$	4.96 $\times 10^{22}$
Density (300 K) g/cm^3	5.32	2.33
Dielectric Constant	16	12
Intrinsic Carrier Density (300 K) cm^{-3}	2.4×10^{15}	1.5×10^{10}
Intrinsic Resistivity Ω.cm	47	2.3×10^{5}
Energy Gap (300 K) eV	0.665	1.115
Energy Gap (0 K) eV	0.746	1.165
Ionisation Energy (77 K) ϵ_{pair} eV	2.96	3.76
Fano Factor (77 K)	0.058	0.16
Electron Mobility (300 K) cm^2/V.s	3900	1350
Hole Mobility (300 K) cm^2/V.s	1900	480
Electron Mobility (77 K) cm^2/V.s	3.6×10^{4}	2.1×10^{4}
Hole Mobility (77 K) cm^2/V.s	4.2×10^{4}	1.1×10^{4}

Table 3.1: Physical properties of germanium and silicon [Kno00].

3.4 Detector Efficiency

The efficiency of a detector is closely related to its density and volume. It can be described using one of the following sections;

3.4.1 Absolute Efficiency

Is given by the ratio of the number of photons emitted by the source to the number of photons detected,

$$\epsilon_{abs} = \frac{\text{Number of detected photons}}{\text{Number of emitted photons}}. \tag{3.15}$$

The absolute efficiency is heavily influenced by the detector geometry, and for this reason is more commonly used to comment on the efficiency of a detection system, as opposed to an individual detector.

3.4.2 Intrinsic Efficiency

The intrinsic efficiency is given by the ratio of the number of photons detected to those incident on the detector,

$$\epsilon_{int} = \frac{\text{Number of detected photons}}{\text{Number of photons incident on the detector}}. \tag{3.16}$$

As it is the ratio of those photons detected to those incident, the intrinsic efficiency is independent of the source-detector geometry and as such, is a much more useful metric to compare detectors of different geometries.

3.4.3 Relative Efficiency

The relative efficiency is an absolute efficiency measurement which compares the detector's performance with that of a 76mm diameter by 76mm length sodium iodide (NaI) detector, detecting 1.33 MeV photons from a source situated 25cm away.

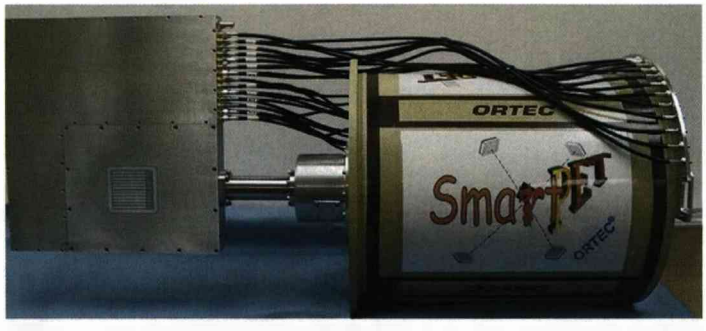

Figure 3.6: Photograph showing a SmartPET detector.

3.5 The SmartPET detectors

Two SmartPET (HPGe planar) detectors were to be used in this study. Each SmartPET detector consists of a single $74 \times 74\,\mathrm{mm}^2$ crystal of which the active volume is $60 \times 60 \times 20\,\mathrm{mm}^3$. 7 mm of the extra germanium surrounding the active area is also instrumented to maintain the uniformity of the electric field toward the edges of this area. This is known as the guard ring. The crystal is electrically segmented into 12 strips on both the AC and DC coupled faces, creating a strip pitch of 5mm and an intrinsic spatial resolution of $5 \times 5 \times 20\,\mathrm{mm}^3$. The AC coupled contacts are $0.3\,\mu$m thick and have a separation of $180\,\mu$m while the DC coupled contacts are segmented with $50\,\mu$m thick strips separated by $300\,\mu$m. The impurity concentration of the crystals is approximately $6{\times}10^9$ with the variation through the depth less than 5 percent. One of the SmartPET detectors can be seen in Figure 3.6. The dewars hold 12 litres of LN_2 providing cooling for up to 72 hours. Details of the initial SmartPET 1 characterisation are documented in [Tur06].

In order to localise the γ ray interaction sites beyond that of the volume achievable from the detector's segmentation ($5 \times 5 \times 20\,\mathrm{mm}^3$), shown in Figure 3.7, it is necessary to use information contained in the charge pulse created from the strip in which the charge was collected, (real charge pulses) and from the pulses created in the adjacent strips, (image charge pulses). This process is known as pulse shape analysis (PSA)

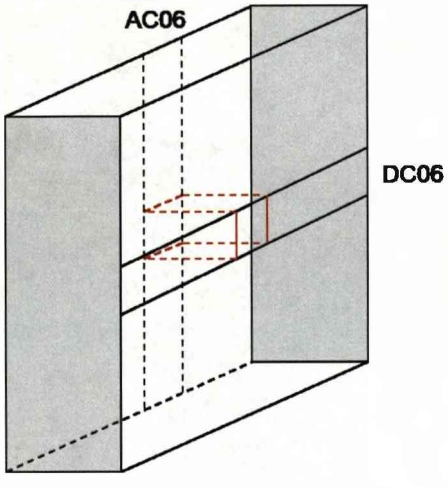

Figure 3.7: Diagram to illustrate the effective voxel/pixel created by opposing contacts. [Lie01].

3.5.1 Real Charge

Real charge is a common term used to describe the time varying charge pulse associated with the collection of either charge species at the electrode. The amplitude of the pulse is proportional to the energy deposited and the shape of the leading edge is used to determine the distance of the interaction site from the collecting electrode. The electrode that collects the charge is known as the *hit* segment or strip. An example of a real charge pulse collected on a planar germanium strip can be seen in the centre plot of Figure 3.8.

3.5.2 Image Charge

The image charge (also known as transient charge, mirror charge or spectator charge), is the term used to describe the charge induced on electrodes in the vicinity of the hit strip by the movement of the charge species from the point of interaction to the hit strip electrode. With increasing distance from the hit strip the magnitude of the image charges diminishes to such a point that they become difficult to discrim-

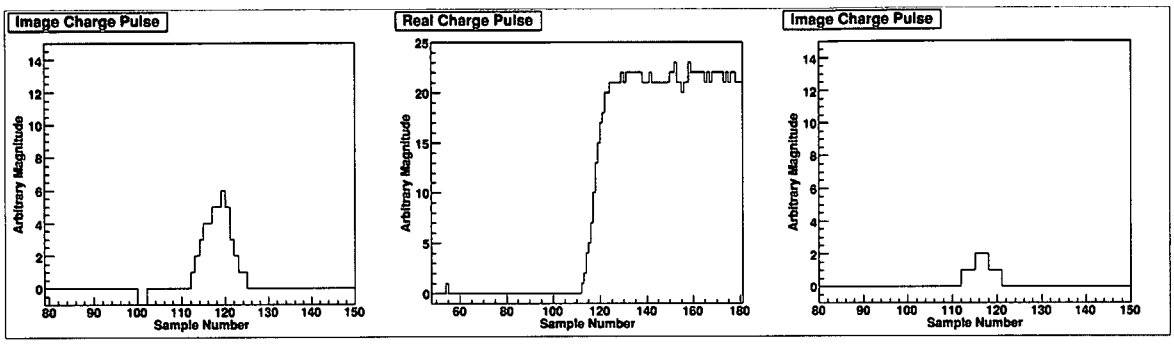

Figure 3.8: Pulses recorded from three neighbouring strips after a γ ray interaction in the SmartPET detector. The real charge is recorded from the hit strip (centre strip) in which the charge from the interaction was collected and is represented by the centre plot. The image charges are induced charges, originating from the movement of charge from the interaction site to the collecting electrode, in the strips adjacent to the hit strip. These are represented by the plots to the left and right of the figure. The ratio of the areas of these image charges is used to assign an interaction position across the face of the hit strip, where the larger the area of the induced charge, the closer the proximity of the interaction to the strip of that image charge. By observing the above response it would be presumed that the interaction occurred closer to the left side of the hit strip than the right.

inate from the noise. Therefore image charges in this thesis will only be used from those strips immediately adjacent to the hit strip. Examples of image charges can be seen in the plots to the left and right in Figure 3.8.

The induced charges observed from an interaction can be exploited to determine the interaction position to a higher precision than the physical size of the electrodes. The closer the proximity of the moving charge to the neighbouring electrode, the greater the magnitude of the induced charge on that neighbouring electrode. The asymmetry observed between net areas of image charges observed on the strips either side of the hit strip can be used to determine the lateral position of an interaction in the hit strip. By acquiring data from collimated photons at finite positions across the strips of the detector [Tur06], one can assume knowledge of the interaction position. This procedure allows the area asymmetry between the two image charges to be used to calibrate the position of interaction. The area asymmetry is calculated in the form of the asymmetry parameter, A,

$$\mathrm{A} = \frac{A_{left} - A_{right}}{A_{left} + A_{right}}, \tag{3.17}$$

where A_{left} is the area of the image charge to the left of the hit strip, and A_{right} is the area of the image charge in the strip to the right of the hit strip. This method has been applied to the SmartPET planar detector and has been demonstrated to locate the position of interaction to within $1 \times 1\,\mathrm{mm}^2$, [Tur06], compared to the raw strip segmentation of $5 \times 5\,\mathrm{mm}^2$.

Chapter 4

Depth of Interaction Characterisation

4.1 Introduction

The ability to localise the position of interaction through the depth of the SmartPET crystal is important for Compton image reconstruction, as discussed in Chapter Two. Figure 4.1 is a hypothetical representation of different source locations that are reconstructed for two events which interact in the same lateral plane, deposit the same energy in both detectors, but with different depths of interaction. The position at which the cone base touches the reconstruction plane is considered to be the location of the source. Many events with little or no knowledge of the depth of interaction in the detectors can result in uncertainty in the source location and subsequently be observed as blurring (parallax image broadening). Similarly, Figure 4.2 represents the different source locations calculated for events which interact at the same depth as each other in the detector but at different lateral locations.

In order to determine the depth of an interaction in SmartPET, pulse shape response is characterised by controlling the interaction position with a collimated radiation source mounted on a scanning table. A scan is performed over the entire detector side (i.e. the $20 \times 60\,\mathrm{mm}^2$ face between the contacts) in 1 mm increments using a collimated beam of γ photons. By attributing γ-ray interactions to the position of the

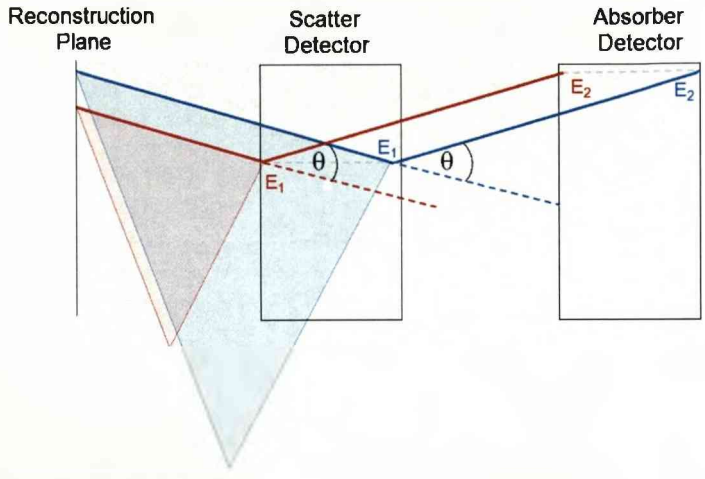

Figure 4.1: A 2D diagram of a Compton camera viewed from the side in 2D. The red and blue triangles are 2D slices through reconstructed cones created by events from two separate gamma rays of equal energy. The path of each gamma ray is shown by the red and blue lines which are emitted from a position level with the reconstruction plane. Both gamma rays interact in the same lateral position as each other, and scatter through the same angle (θ), thereby depositing identical energies in both detectors (E1 in the scatter detector and E2 in the absorber detector). The only difference between the two sets of events is the depth of interaction. The perceived reconstruction position of the source of each gamma ray is the point at which the cones touch the reconstruction plane. For this example, the differences in the reconstruction positions are due to the differing interaction depths of the respective gamma rays.

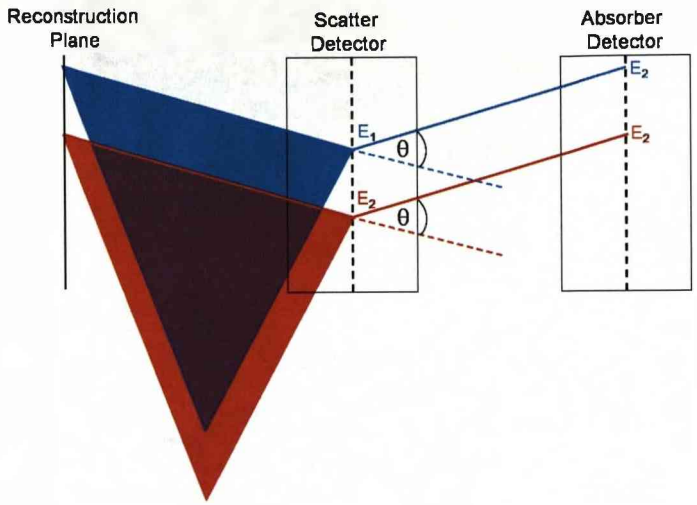

Figure 4.2: A 2D diagram of a Compton camera viewed from the side in 2D. The red and blue triangles are 2D slices through reconstructed cones created by events from two separate gamma rays of equal energy. The path of each gamma ray is shown by the red and blue lines which are emitted from a position level with the reconstruction plane. Both gamma rays interact at the same depth in the detectors as each other, and scatter through the same angle (θ), thereby depositing identical energies in both detectors (E1 in the scatter detector and E2 in the absorber detector). The only difference between the two sets of events is the position of interaction in the lateral plane. The perceived reconstruction position of the source of each gamma ray is the point at which the cones touch the reconstruction plane. For this example, the differences in the reconstruction positions on the reconstruction plane are due to the differing interaction positions in the lateral plane of the respective gamma rays.

collimator at the time of detection the pulse shape response can be calibrated to yield the position of interaction. Diagrams of the scanning set up are shown in Figures 4.5 and 4.6. In this work the pulse shape response is measured by risetime parameters, which are defined as the time taken for a signal pulse to increase from 10 percent of its final magnitude to a greater fraction of its final magnitude. These risetime parameters can be employed via two methods; a constant fraction method, or the time difference method [Amm00], the latter of which is more commonly applied to planar detectors. These methods will be discussed in more detail later in this chapter.

Previous experiments and analysis [Tur06], [Coo07], [Bos09] to localise the position of interaction through the depth of the SmartPET detector yielded an event by event depth sensitivity of 4mm. It has been demonstrated that sub-millimeter depth sensitivity has been achieved in other HPGe planar detectors [Wul02] using parameters derived from the risetime of the collected pulse. The subsequent analysis presented in this chapter aims to improve the depth sensitivity from 4mm to 1mm using these techniques.

It was observed [Tur06], [Coo07], [Bos09], that the response of the SmartPET detector varies between each of the strips, or for different positions across individual strips, as interactions from the centre of the detector are compared with those toward the edges of the active volume. This is suggested [Tur06] to be due to changes in the electric field toward the edges of the detector, referred to as edge effects, implying that characterisation of the pulseshape response as a function of depth will have to be performed for each region that exhibits a different response, in order to improve the imaging capability of the SmartPET system. To gain a good understanding of the generic pulseshape response for a specific region one would require a high number of statistics in all regions. A previous side scan experiment [Tur06] was conducted with a 70.2 MBq ^{137}Cs source resulting in 35 photopeak counts per second emanating from the collimator. Figure 4.3 shows the average counts detected per scan step for

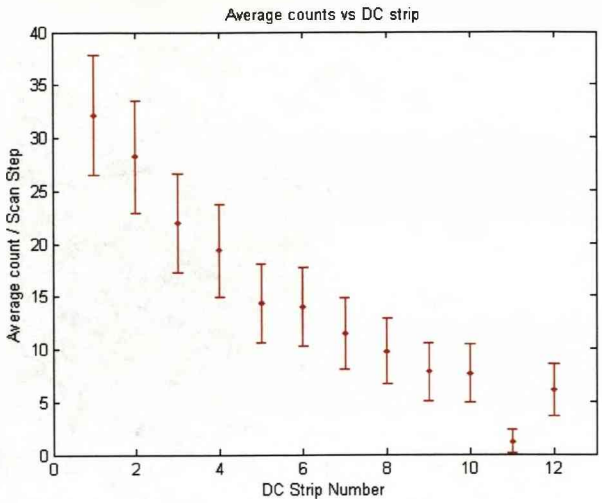

Figure 4.3: The average number of photopeak interactions per scan step for each strip. The DC strips are perpendicular to the collimator where DC01 corresponds to the strip closest to the collimator, and DC12 to the strip farthest from the collimator.

each DC strip, where each scan step was stationed for 120 seconds. The orientation of the strips with respect to the collimator can be seen in Figure 4.6. It can be seen that DC12 (i.e. the strip furthest from the collimator), averages about 6 counts per scan step. This number of counts was not high enough to provide a sufficient level of confidence in the characterisation of the detector in the areas that were far from the collimator.

With low statistics in some regions of SmartPET in the data set used in [Tur06], it was decided to replicate the side scan experiment to achieve adequate statistics in all regions of the detector.

4.1.1 Data Acquisition System

The requirement to analyse the shape of the pulses produced by the charge sensitive preamplifiers on an event-by-event basis, requires the use of a digital electronics system. The DAQ system is based on 8 VME GRT4 modules designed by Daresbury

Laboratory [Laz04]. Each 4 channel card has a sampling rate of 80MHz over a 14 bit dynamic range with one Field-Programmable Gate Array (FPGA) for each channel. The GRT4 modules are programmed with the moving window deconvolution (MWD) algorithm [Geo93] that extracts precise energy information from the sampled data with minimum processing dead time.

4.1.2 Trigger

The GRT4 cards are triggered externally using the pulses from the AC coupled side and conventional analogue timing electronics. The trigger was achieved by passing the twelve signals from the AC side through Timing Filter Amplifiers (TFAs), Ortec models 474 and 863, which were set with a differentiation time of 200ns and an integration time of 50ns. From the TFAs, the signals were passed through Constant Fraction Discriminators (CFDs), (Ortec models 473 and 934), set with a 10ns time delay, into a logical OR unit and then to a gate and delay generator (Ortec 416), as illustrated in Figure 4.4. The trigger signal was then input to the GRT4 cards and the data read out from the twenty-four channels (12 AC coupled channels on one face, and 12 DC coupled channels on the opposing face). Whilst the GRT cards are processing data an inhibit signal is sent to the gate and delay unit to prevent any further trigger signals being sent until all the data has been read out. For each channel 3.2 μs (256 samples) of data is recorded. The trigger (CFD threshold) was set at $\approx 60\,\text{keV}$, using the 60 keV the gamma ray from ^{241}Am corresponding to roughly 10 percent of the photopeak energy from the ^{137}Cs source (662 keV).

4.1.3 Experimental Setup

The detector was positioned above a 1mm diameter, 80mm long tungsten collimator at a total distance of 83mm from the collimator. The detector was orientated so that the side of the detector would be scanned (Figure 4.5). The detector side will be equivalent to the detector depth when photons are incident through either the AC

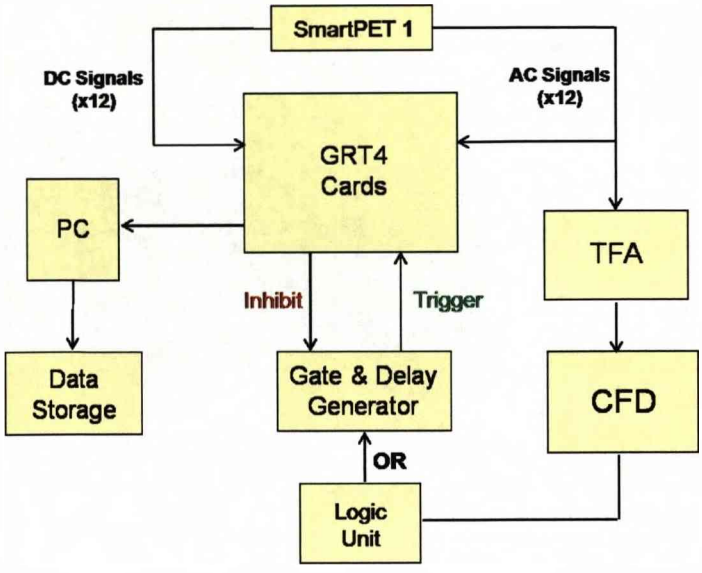

Figure 4.4: A diagram of the trigger set up for the side scan of SmartPET.

or DC face, as in a Compton camera measurement. The isotope used for the scan was ^{137}Cs, as before, however this source had an activity of 994 MBq, compared to 70.2 MBq in the previous scan.

The count rate observed from the collimator using a NaI scintillator detector was ≈ 700 counts/second, however the actual count rate that could be recorded by SmartPET was limited to 120 counts/second by the digital acquisition system. The total distance between the detector and collimator aperture of 83 mm was due to the detector casing (62 mm), and restrictions due to a detector mounting frame surrounding the scanning setup (21 mm). Monte Carlo simulations have shown a FWHM of the beam spread to be approximately 1.3 mm at the centre of the detector [Oxl09]. To ensure the detector is shielded sufficiently from the source, 17 cm deep, 36 cm diameter lead disk was been placed in between the detector and the source. The lead disk had an aperture bored through it in which the collimator was situated. The source was mounted in a lead brick machined for this purpose and placed beneath the aperture of the lead disk. The lead, source and collimator are sitting on top of an x-y positioning

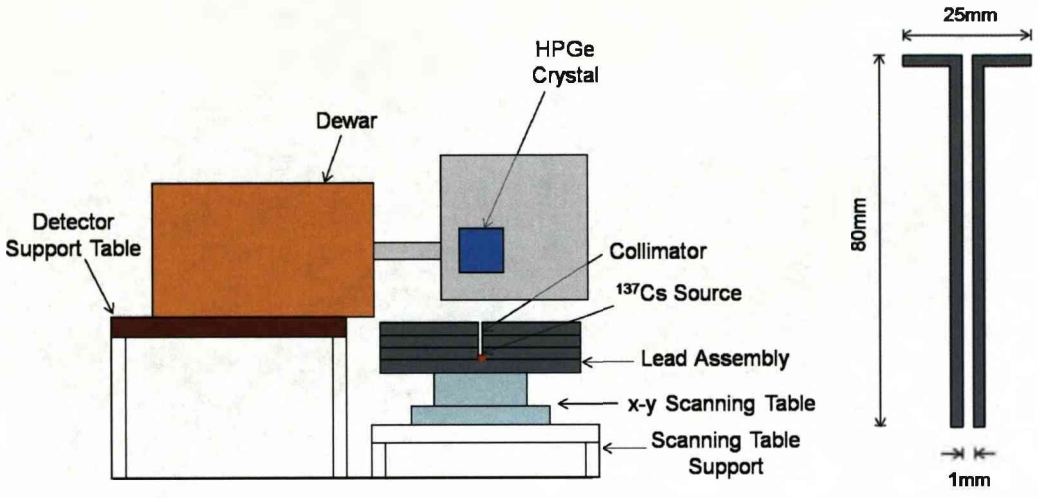

Figure 4.5: Diagram of the SmartPET detector's positioning above the scanning table. A diagram of the collimator and its basic dimensions are to the right of this figure. The detector was positioned so that the depth of the crystal would be scanned. The orientation of the strips from each face with respect to the collimated photon beam can be seen in Figure 4.6.

table. The positioning table is used to move the collimator with respect to the detector, and is driven by two stepper motors which position the table with a precision of 100 μm. The source was raster scanned over the entire side face of the SmartPET crystal in 1 mm steps for a duration of 610 seconds per position, increased from 120 seconds per position in the previous scan [Tur06]. The use of a higher activity source in conjunction with a longer scan time increased the statistics throughout the detector as desired. The statistics recorded from this scan and the previous scan are compared in Figure 4.7.

The active area of the crystal is identified by the increased number of accepted events in Figure 4.8. The DC contacts are at depth 0 mm and the AC contact at depth 20 mm. The lower intensity under the AC strip boundaries is apparent as the side scan was performed with the AC strips parallel to the collimated beam. There are two reasons for the lower intensity on the interstrip boundary:

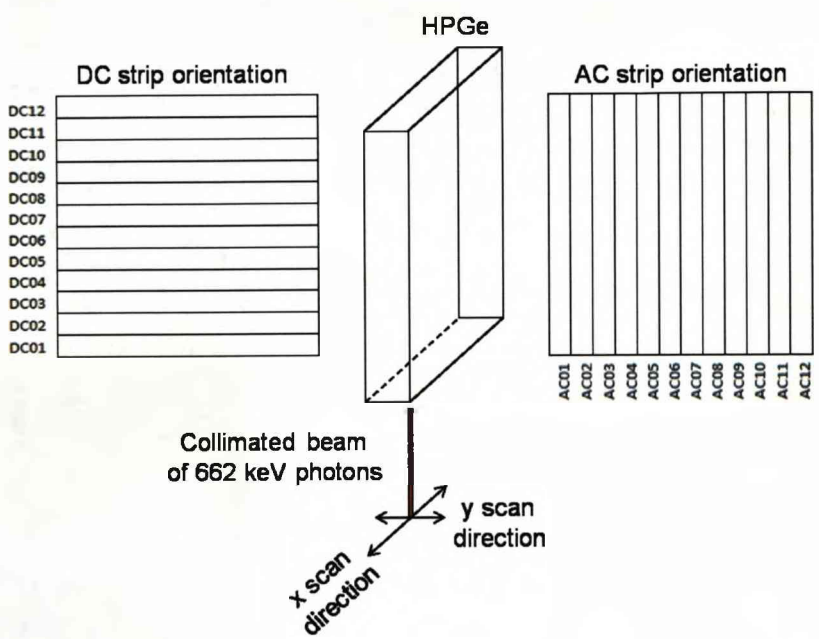

Figure 4.6: Diagram to illustrate the SmartPET detector volume and strip orientation with respect to the scanning table. The AC strips are parallel and the DC strips orthogonal to the collimated photon beam which is incident on the side of the detector and represented by the red arrow.

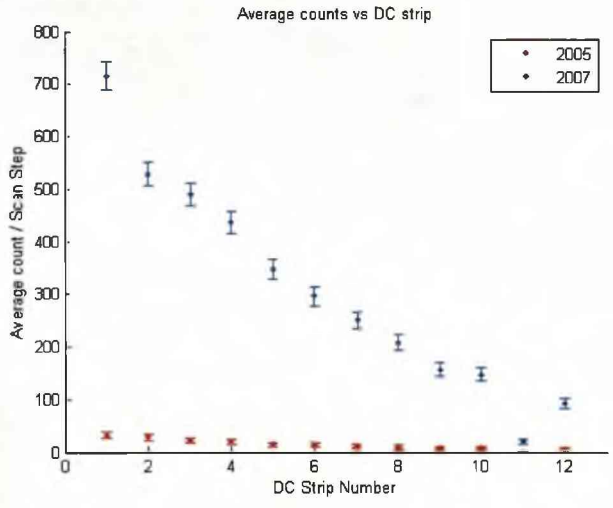

Figure 4.7: A comparison of the number of photopeak events recorded between the present and previous side scan measurements of SmartPET1. Average number of photopeak interactions per scan step are plotted for each strip. Again, the DC strips are perpendicular to the collimator where DC1 corresponds to the strip closest to the collimator, and DC12 to the strip furthest from the collimator (see Figure 4.6). The dip in statistics at DC11 is suspected to be due to a fault with the contact. It was observed in previous research ([Tur06], [Coo07]), that there is a problem with DC11 in the form of significant charge sharing, double peaking of the photopeak, long risetimes and significantly less statistics than observed in neighbouring strips.

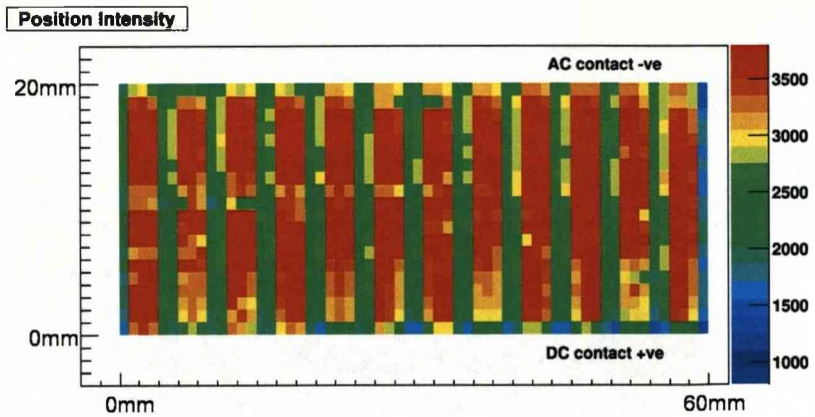

Figure 4.8: Intensity map of the sidescan. All events are fold 1 on each face and energy gated (654 - 667 keV) for all strips except DC11, which required larger energy gates as it suffered from degraded energy resolution and double peaking attributed to a strip contact fault (DC11 gate: 650 - 678 keV).

- Charge sharing due to the finite size of the electron cloud. Whenever a γ ray interacts close to a strip boundary, the created electron cloud is likely to overlap into the adjacent strip. This causes two strips to share the energy [Kro99].

- Compton scattering into an adjacent strip.

In both cases, the gates for a valid event, fold 1 on both faces and full energy deposition, are not met and hence these events will be excluded from the intensity maps. The *fold* in this thesis refers to the number of strips on a detector face recording a real charge pulse for a single event, where a fold 1 event refers to a single strip on each face recording an interaction.

4.2 Signal Analysis

The shape of a pulse collected at a contact varies as a function of the depth of interaction; at different distances from a detector contact the observed pulse will take different amounts of time to reach the same fraction of its total pulse height. This

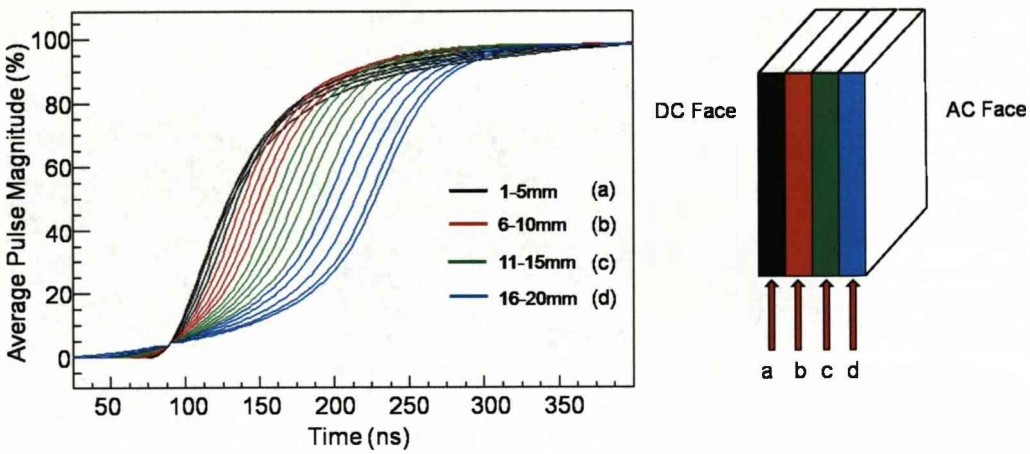

Figure 4.9: Average pulse shapes calculated at each mm through the depth for interactions detected in the voxel created by strips AC06 and DC06 (Figure 4.12). 1 mm corresponds to the first millimetre by the DC face and 20 mm corresponds to the millimetre adjacent to the AC face. The pulses are coloured according to which region of the detector they belong to: 1-5mm = Black; 6-10mm = Red; 11-15mm = Green; 16-20mm = Blue. The diagram to the right illustrates to which region each of the depths and colours belong. The red arrows represent the position of the collimated photon beam, where a = 1-5mm, b = 6-10mm, c = 11-15mm and d = 16-20mm.

observation is commonly used to determine the interaction position through the depth of a planar detector.

To illustrate the change in pulseshape as the depth of interaction changes from one face to the other, average pulseshapes calculated from each millimeter of one scan line through the centre of the detector (strips AC06 and DC06, described by Figure 4.12), are shown in Figure 4.9. The pulses have been normalised and time aligned at 5 percent of their total magnitude. The pulses are normalised to account for the statistical fluctuation of recorded energies. They have been time aligned to ensure equal fractions of the total charge to be collected correspond to the same sample number for each individual pulse collected, allowing a more accurate average pulse to

be constructed. There are 20 average pulses shown in the figure, where each average pulse is created using pulses from each scan position through the 20 mm depth of the detector. They have been coloured by depth region to show the variation in pulse shape response as the collimator moves through the depth. The black pulses correspond to the region of the detector between 1 and 5 mm from the DC face, red to region 6 to 10 mm, green to region 11 to 15 mm and blue to region 16 to 20 mm. It can be seen that as the collimator moves through the depth of the detector, the shape of the pulses varies. By calculating the time taken to reach certain fractions of the final pulse height at different depths, it is possible to assign these times to particular depths, effectively calibrating the risetime response of the detector to the depth of interaction. Two risetime analysis methods commonly used in detector characterisation are the T30T90 method (a constant fraction method) and the T50 time difference method.

4.2.1 T30T90 Risetime method

This method utilises the T30 and T90 parameters, which are the time taken for the pulse to rise from 10 percent of its final magnitude to 30 percent (T30) and to 90 percent (T90) respectively, shown in Figure 4.10.

Both of these parameters vary depending on the depth of interaction. Figure 4.11 shows the average risetime values observed from both the AC and DC contacts, for both parameters, at all positions across the depth of the detector. The units of colour scale to the right of each plot are nanoseconds. It can be clearly seen that both the T30 and T90 plots exhibit trends in risetime value that change as the scan position moves from one contact to the other, and that these observed trends are different depending on which contact is providing the response. It can also be seen that the trend at the edges differs from that of the main body of the detector. This difference indicates that a particular risetime value will not always correspond to the same depth in all areas of the detector, and this observation will need to be accounted for when assigning a risetime value for an interaction to a depth. It must also be noted that

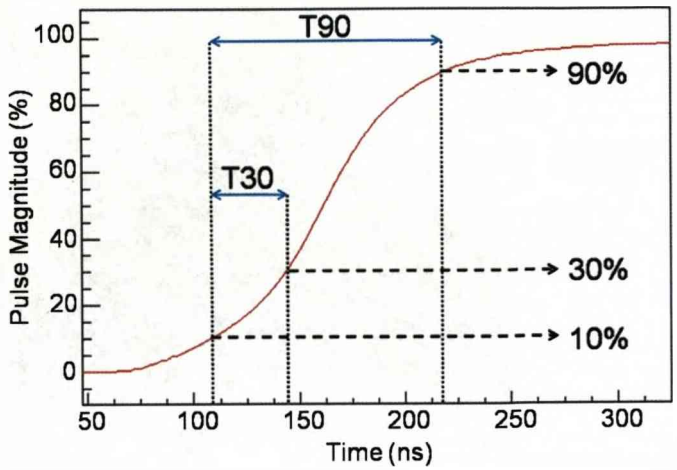

Figure 4.10: A diagram describing the risetime parameters used for depth of interaction analysis. T30 is the time for a pulse to rise from 10 percent to 30 percent of its total magnitude and T90 is the time for a pulse to rise from 10 percent to 90 percent of its total magnitude.

the AC risetime response differs from that of the DC so pulseshapes from each face will need to be investigated separately.

In order to demonstrate a parameters variation with depth of interaction more clearly, the average values for one scan line from the DC face to the AC face were plotted against the depth and are shown in Figure 4.13. The error bars represent the standard error on the mean. The scan line was chosen to be from the centre of a strip in the centre of the detector, in this case the voxel created by the AC06 DC06 contacts. Figure 4.12 illustrates how a strip from each face of the detector creates a single voxel.

From Figure 4.13 it can be seen that there are areas of insensitivity where the risetime is similar for a small range of depths (e.g. 1 - 6 mm for the AC response), or areas of ambiguity, where the same risetime value can represent two different depths (e.g. between 4 - 6 mm and 12 - 14 mm for the T90 DC response). Ideally, a method

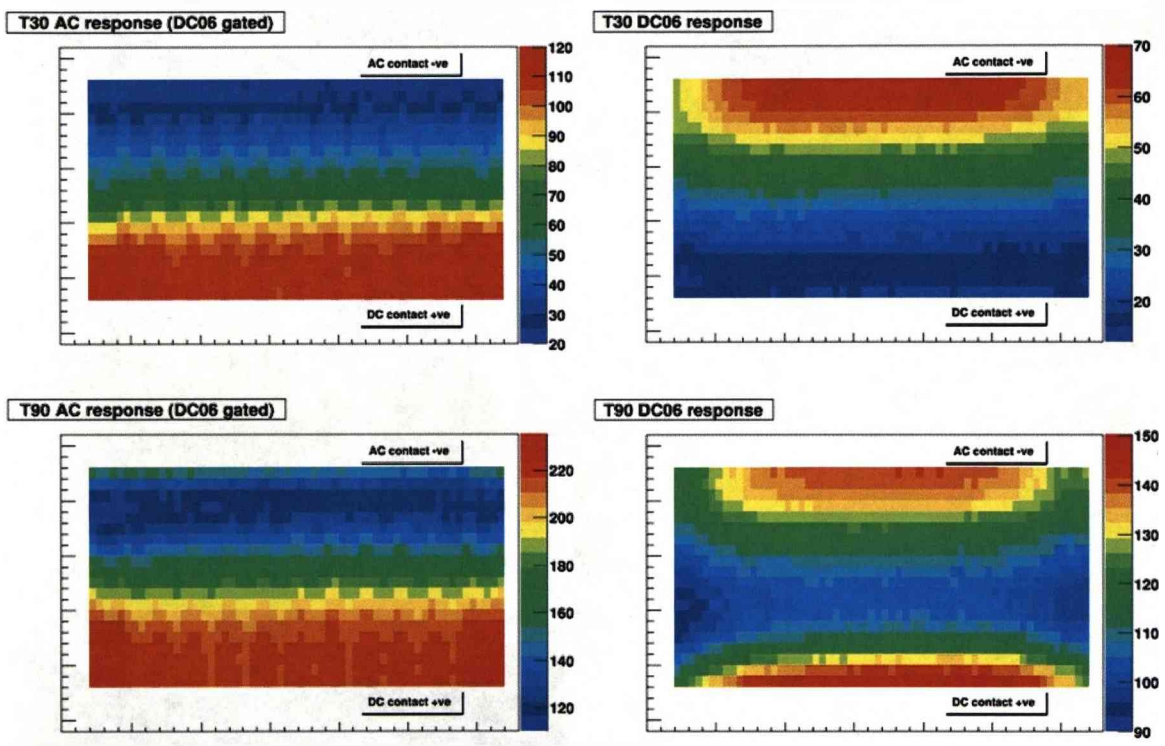

Figure 4.11: Average T30 (top) and T90 (bottom) values as a function of scan position for both the AC response (left), and the DC response (right). The colour scale is in units of nanoseconds.

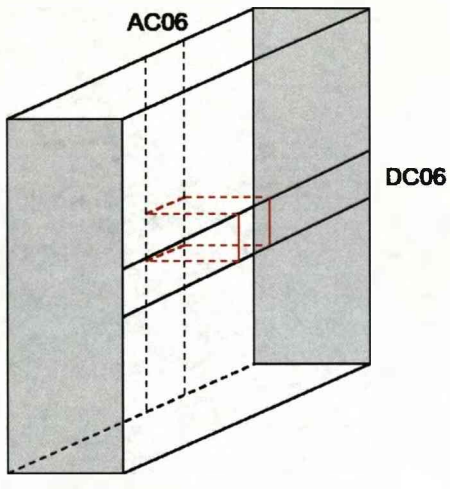

Figure 4.12: Diagram to illustrate the effective voxel/pixel created by the AC06 and DC06 contacts.

using these risetimes to determine the depth of interaction would have no areas of insensitivity or risetime values which correspond to completely different depths. To be able to use these T30 and T90 risetimes and overcome these problems, one parameter is plotted against the other (T30 against T90). This is shown in Figure 4.14 where the values from Figure 4.13 are plotted against each other, rather than against the depth, for both the AC and DC faces. It must be noted that for the AC response the points to the left of the plot represent the depths by the AC contact and to the right, the depths by the DC contact. This is in contrast to the DC response, where to the left of the plot the points represent the depths by the DC contacts, and to the right, the depths by the AC contacts. As in Figure 4.13, the error bars displayed are the standard error on the mean. Each point on each graph in Figure 4.14 corresponds to a particular depth.

It can be seen that almost all points are easily resolvable from each other. So, by combining the T30 and T90 parameters, rather than plotting them individually against the depth, a specific depth can to be assigned to each combination of average T30T90 risetimes without the regions of insensitivity or ambiguity previously observed.

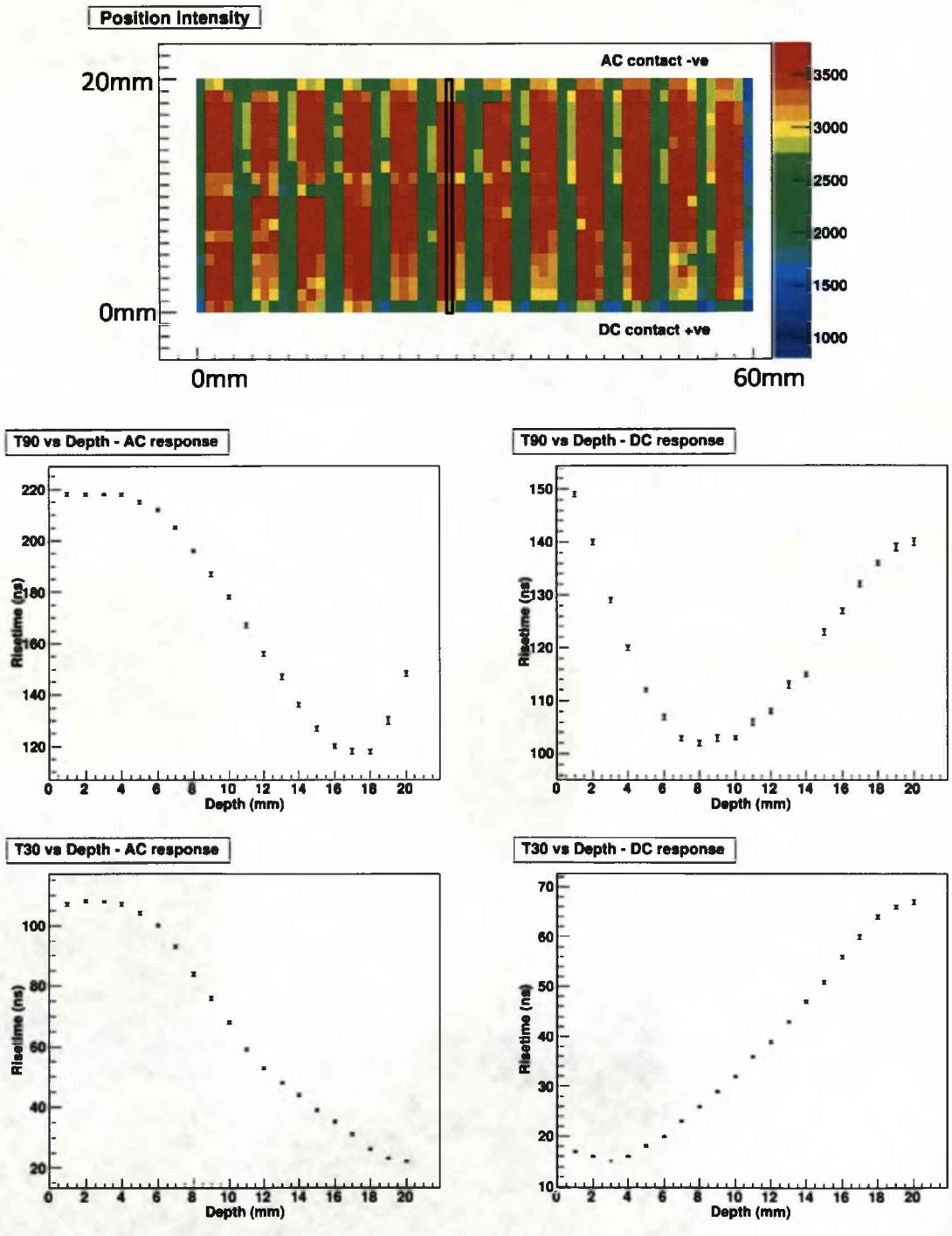

Figure 4.13: Top: Plot of the position intensity as shown in Figure 4.8. The black rectangle highlights the scan positions used to create the average values shown in the plots below. Bottom: Plots showing variation of the risetime parameters T30 and T90 versus depth, where 1 mm corresponds to the millimetre adjacent to the DC face and 20 mm to the millimetre adjacent to the AC face. All the risetime values are average values with associated errors (calculated as the standard error on the mean).

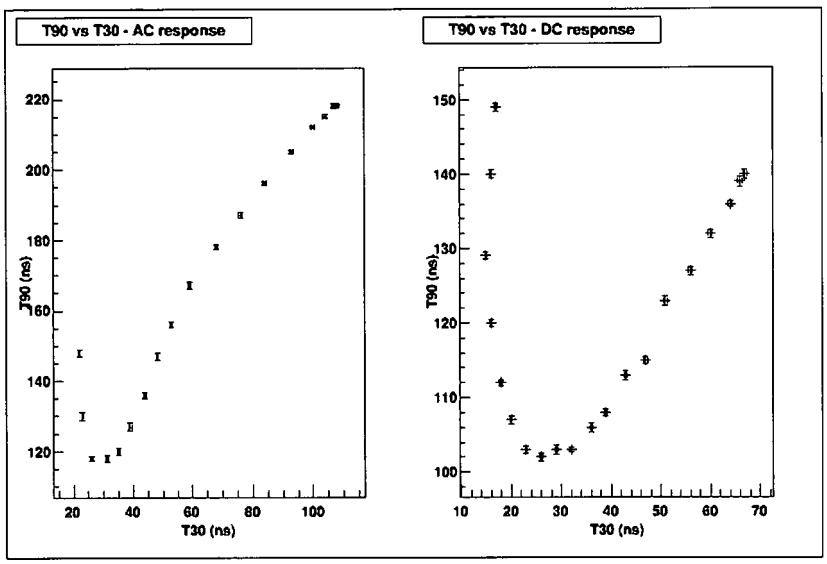

Figure 4.14: T30 vs T90 for both the AC and DC responses. Each point on the graph corresponds to a particular depth. For the AC response, the points to the left are from the positions by the AC face (at the 20 mm position), and the points to the right near to the DC face (at the 1 mm position). This is the opposite way round for the DC response, where the points to the left represent the positions near the DC face (1 mm position), and the points to the right near to the AC face (20 mm position)

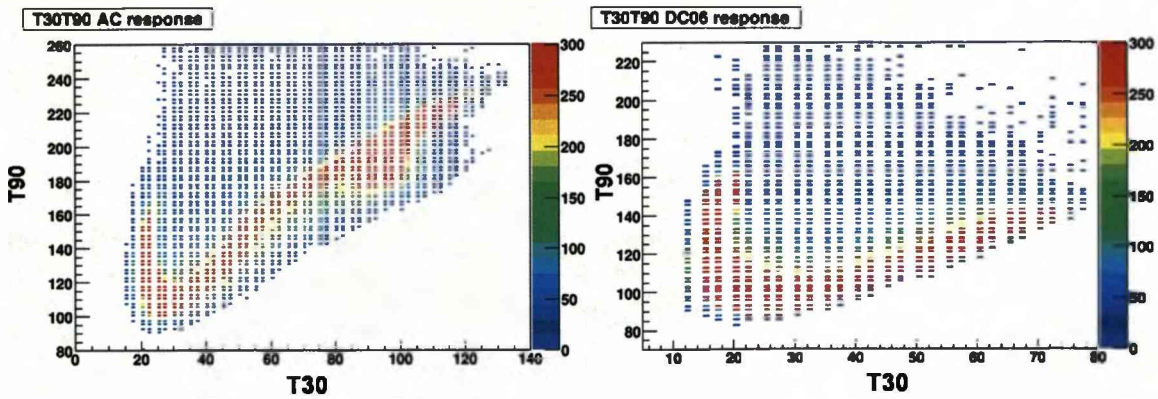

Figure 4.15: Distribution of T30 vs T90 events from centre strip contacts, AC06 and DC06 (Figure 4.12). Along the x-axis are the T30 values (ns) and along the y-axis are the T90 values (ns) with the colour scale showing the intensity of the frequency events. All events in these plots are energy and fold 1 gated.

This method is required to provide depth sensitivity for events which are to be individually reconstructed from the depth position assigned. In order to progress toward the 1 mm depth sensitivity target of this investigation, a method was needed to assign any one event to a depth. The distribution of events that were used to calculate the average values is shown in Figure 4.15. Each average T30 and T90 point calculated has a range of values for each parameter associated with it. In order to allocate a depth to any one event, finite areas (corresponding to ranges of T30 and T90 values), of the distribution shown in Figure 4.15 must be defined and assigned a depth. Therefore any event that occurs within a particular area is assigned that area's depth. To do this, the distributions from each depth which contributed to Figure 4.15 must be plotted and used to create polygonal gates around the distribution area. This results in the creation of 20 polygonal gates, 1 for each millimeter through the depth.

Figures 4.16 and 4.17 are plots showing the total distribution of events for every other scan position through the depth of the SmartPET detector. A selection of scan depths have been used for ease of display whilst continuing to illustrate the change

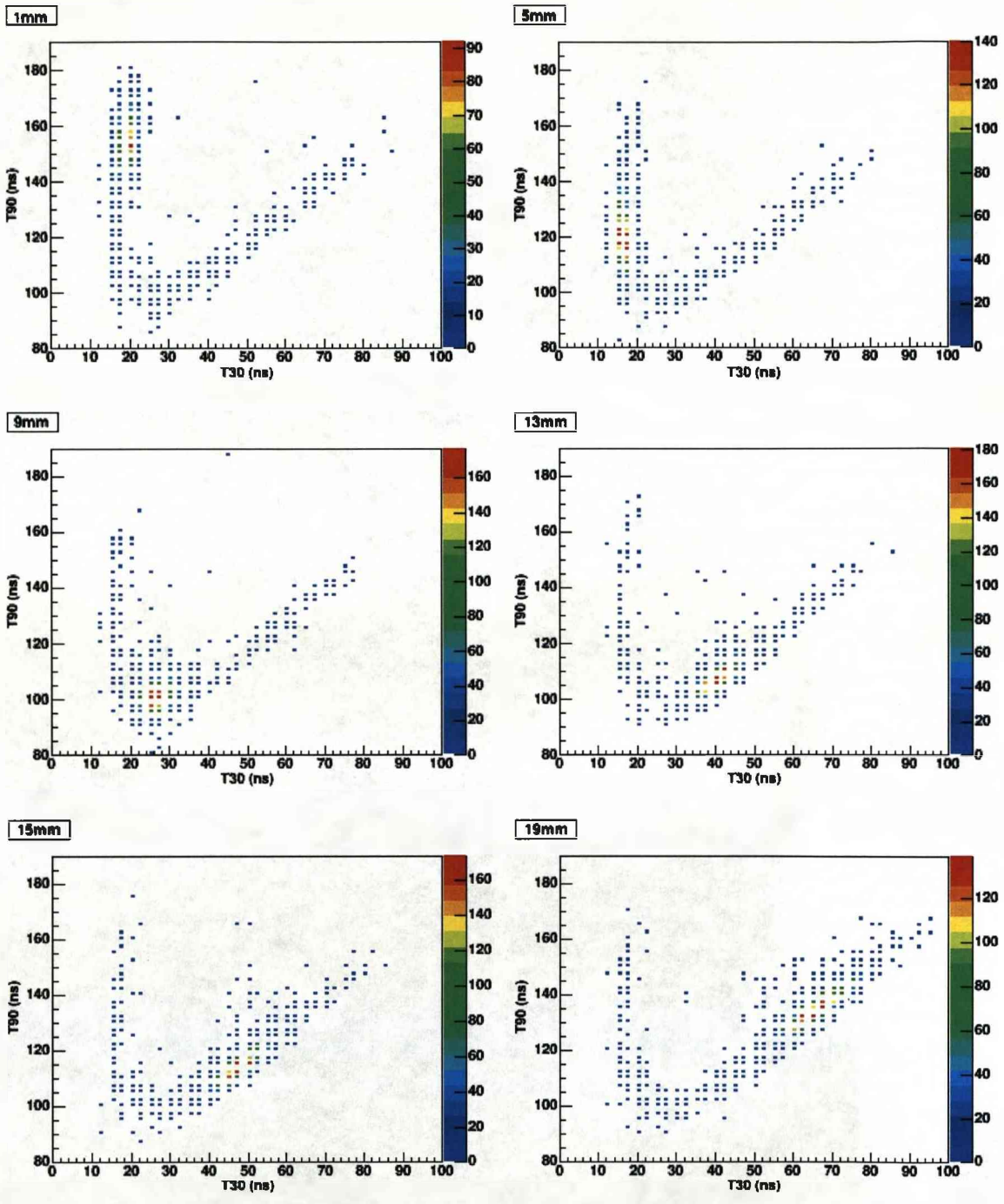

Figure 4.16: T30 versus T90 plots of the DC06 response for a selection of depths through SmartPET from 1mm to 19mm inclusive, where the colour scale represents the intensity of counts. T30 values plotted along the x axis and T90 values plotted along the y axis. All events are energy and fold 1 gated.

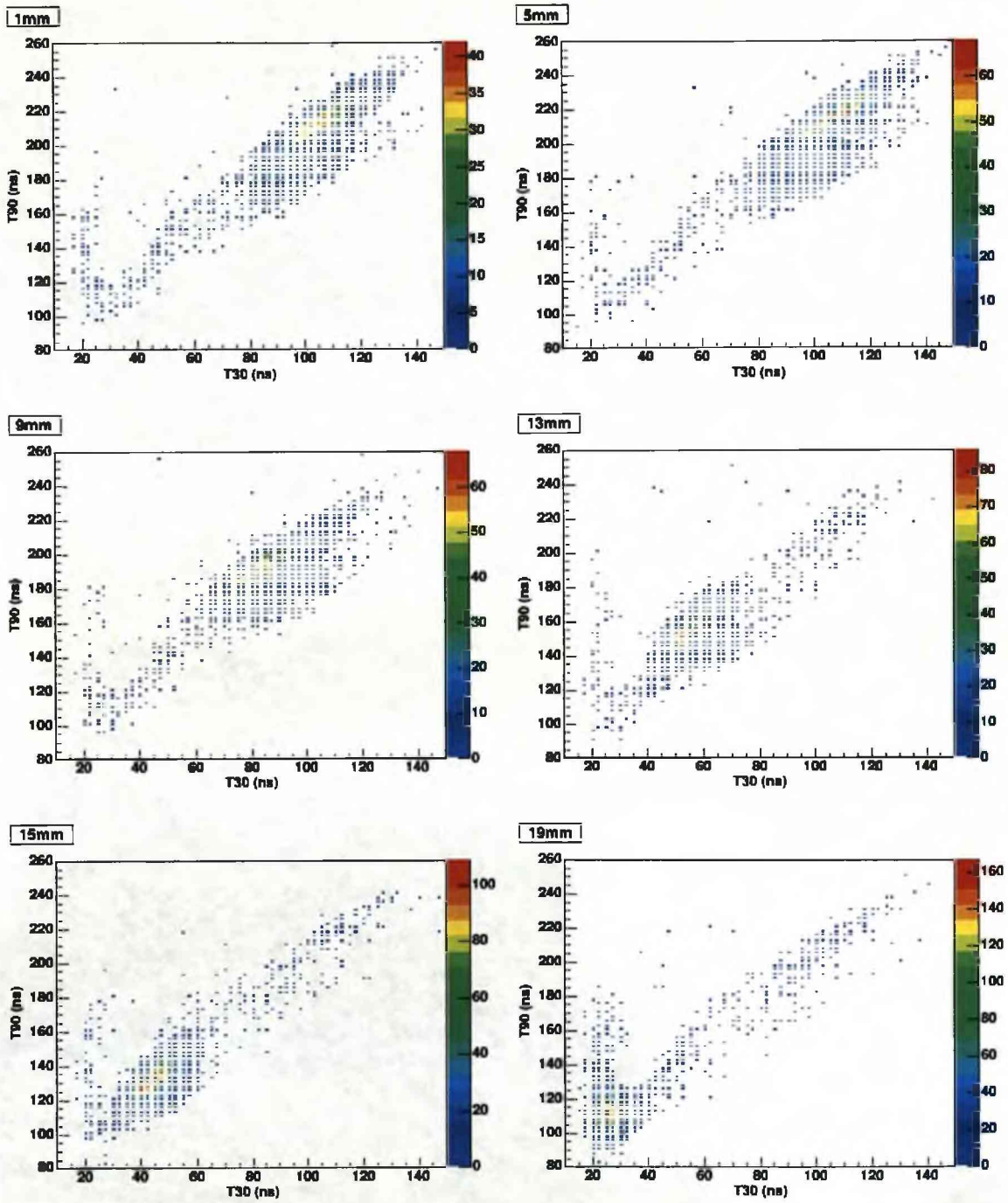

Figure 4.17: T30 versus T90 plots of the AC06 response for a selection of depths through SmartPET from 1mm to 19mm inclusive, where the colour scale represents the intensity of counts. T30 values plotted along the x axis and T90 values plotted along the y axis. All events are energy and fold 1 gated.

in the trend of the distribution as the scan moved through the depth. In both cases 1mm corresponds to the first millimeter scan position by the DC contact and 20mm to the scan position by the AC contact. Figure 4.16 shows the response from DC06 and Figure 4.17 shows the response from AC06. For both contacts it can be seen that for each scan position an area of intensity occurred and moved throughout the distribution as the collimator was moved from one face of the detector to the other. It can also be seen that for any scan position there are small numbers of events present throughout the entire range of possible T30 versus T90 values. These events that fall outside the region of high intensity could be attributed to:

- The detected event being Compton scattered prior to detection in those contacts and so producing a T30vsT90 response not characteristic of that position. Scattering could feasibly occur in the collimator, detector casing or the high voltage coupling for the detector. The position of the H.V. coupling can be deduced from the areas of low intensity present in an intensity plot of the side of the crystal from a side scan using ^{57}Co [Coo07],[Bos09]. This plot can be seen in Figure 4.18 where the areas of low intensity correspond to where the lower energy (122 keV) ^{57}Co γ rays are attenuated by the high voltage coupling to the detector.

- Compton scattering within the detection volume of the contacts, which is the $5 \times 5 \times 20\,\mathrm{mm}^3$ effective voxel created from one strip on each face by the orthogonal orientation of the strips with respect to each other (Figure 4.12). This could produce multiple interactions at different distances from the contacts yielding uncharacteristic risetimes, whilst still satisfying the energy gate and fold one event acceptance criteria.

The ambiguity in pulseshape response which is manifested from these suggestions could feasibly be removed by performing a coincidence scan rather than a singles scan.

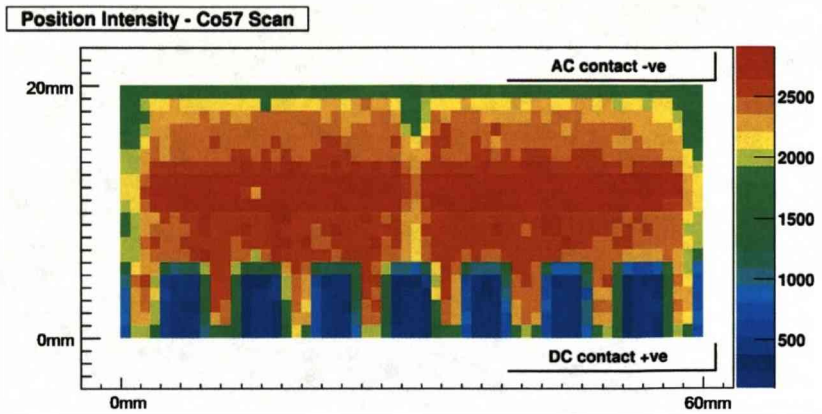

Figure 4.18: Plot showing the photopeak intensity as a function of position from the ^{57}Co side scan. The regions of low intensity by the DC face are the result of the high voltage coupling capacitors attenuating the 122 keV photons prior to interaction in the crystal.

The coincidence measurement requires the collimated γ-rays to undergo a 90^0 Compton scatter in the detector and be subsequently detected in separate detector array (typically NaI scintillators) in a predetermined time window ensuring coincidence between the events. The separate detector array is collimated at an angle of 90^0 with respect to the source collimator ensuring that only photons that scatter through 90^0 trigger the system. More details of this technique can be found in [Des02]. The data produced from this technique is of very high quality, however very few events satisfy the interaction criteria making the acquisition process extremely lengthy. Due to the experimental time constraints, an attempt to characterise the response over the whole detector side was not possible, resulting in a singles scan being conducted.

A method is required to define finite areas of the T30T90 distribution that correspond to a particular depth. It is assumed that the pulseshapes (and therefore T30T90 values) are more likely to be characteristic of that scan depth in the small areas of high intensity, than in the large areas of low intensity, as observed in the T30T90 distributions from each scan depth (Figures 4.16 and 4.17). To assign the events more likely of a specific depth to a finite area, a frequency threshold is introduced to each

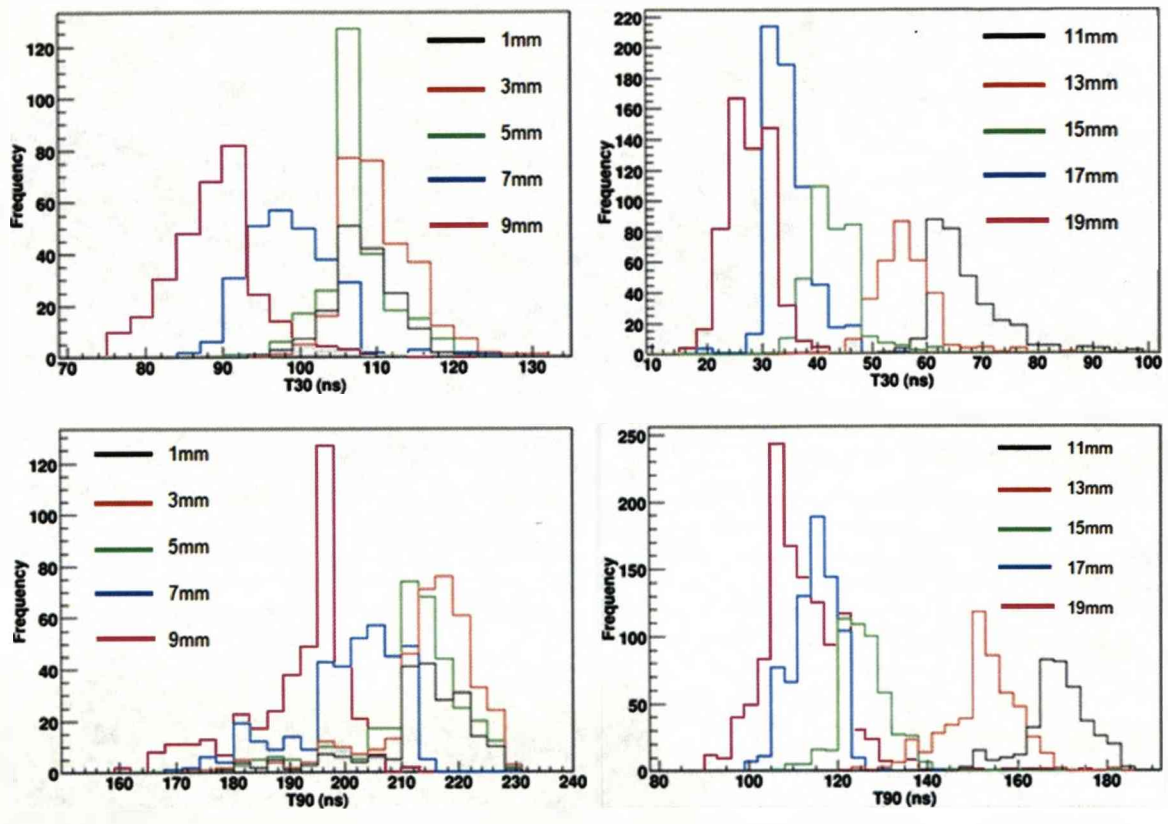

Figure 4.19: Histograms showing the distribution of pulseshape risetimes as a function of the T30 and T90 parameters for the AC06 contact.

bin in each distribution. Examples of the distributions grouped together can be seen in Figures 4.19 and 4.20. These plots show the distribution of each parameter (T30 or T90), for each face, for every other millimeter through the depth.

It can be seen that the distributions are not the same shape for each millimeter and also that there is a significant amount of overlap between the distributions, which reduces as a function of increasing intensity. There are differing numbers of events in each scan position, so a method was chosen to use an intensity cut that was a function of the number of counts in the distribution. It can also be seen that the distributions from the DC contact are narrower than those belonging to the AC contact, indicating

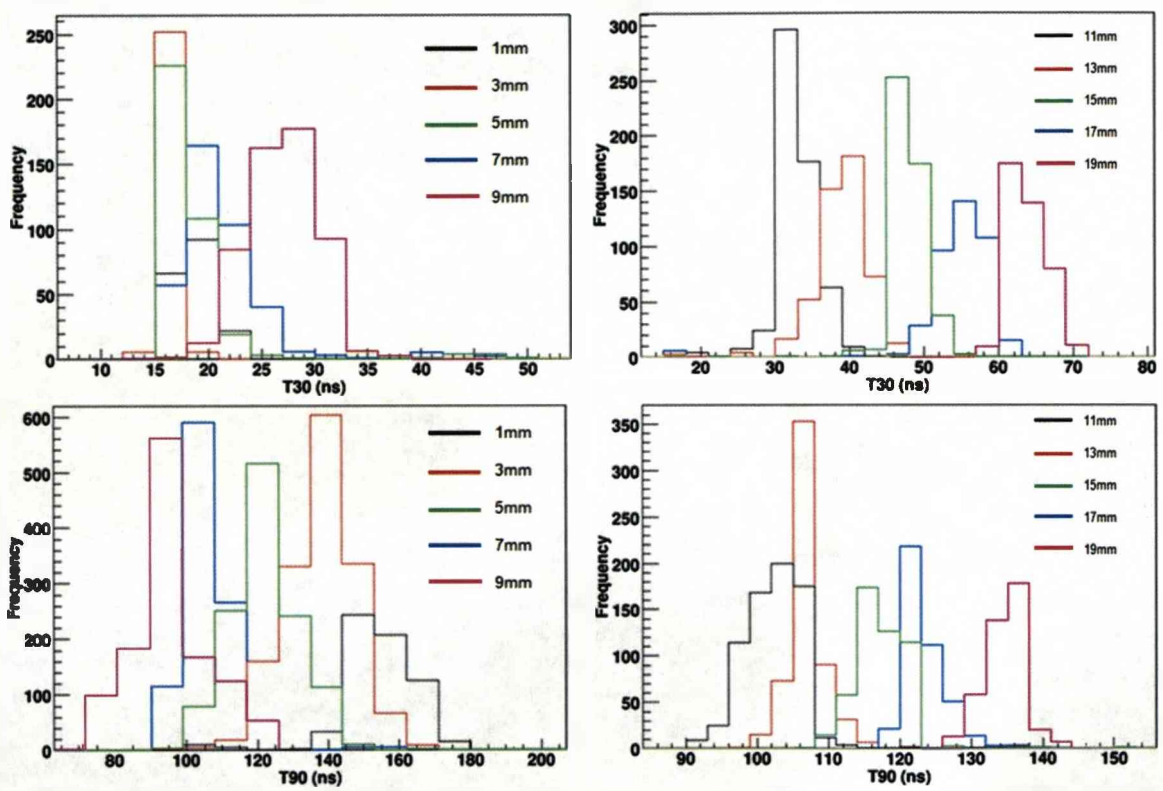

Figure 4.20: Histograms showing the distribution of pulseshape risetimes as a function of the T30 and T90 parameters for the DC06 contact.

that the events from the DC contact are more localised than the AC contact. Why this was the case is not obvious. In order to try and speculate as to the reason behind this observation, consideration was given to the different mobility attributed to each charge carrier species. It is known that electrons (collected by the DC contact) have a greater mobility than holes (collected by the AC contact) as presented in Table 3.1. Although this factor alone does not result in a great difference in carrier drift velocity at saturation voltage, a larger difference in drift velocity between the two charge species occurs as the voltage decreases below the saturation voltage. These effects can be seen in Figure 4.21 which highlights the relative differences between the respective drift velocities at a given voltage below saturation (highlighted by the dashed line) and the saturation velocities. These differences are represented by electron V_d (difference between electron drift velocity and electron saturation velocity) and hole V_d (difference between hole drift velocity and hole saturation velocity). Should the SmartPET detector bias of -1800V not be sufficient to allow the charge carriers to reach saturation velocity, it is conceivable that the larger value of hole V_d compared to the electron V_d could be responsible for degrading the transport of the holes to a greater degree than that of the electrons. This could result in greater discrepancies between pulse shapes generated in the same region of the detector and hence yield a greater spread of risetime values and ultimately reduced position sensitivity for events observed by the AC contact.

Figure 4.22 shows the distributions from the AC06 and DC06 contacts with differing levels of intensity cut applied. It can be seen that as the intensity cut level was increased (more counts needed in each individual bin), the distributions from each depth become more localised to a particular area. If no intensity cut is applied (Figure 4.22, top), it can be seen that the markers associated with each depth spread through the whole T30T90 distribution range, which would result in a poor interaction sensitivity. When an intensity cut was applied to the data from each depth it can be seen (Figure 4.22, middle) that no one depth had a spread of T30T90 values through the whole

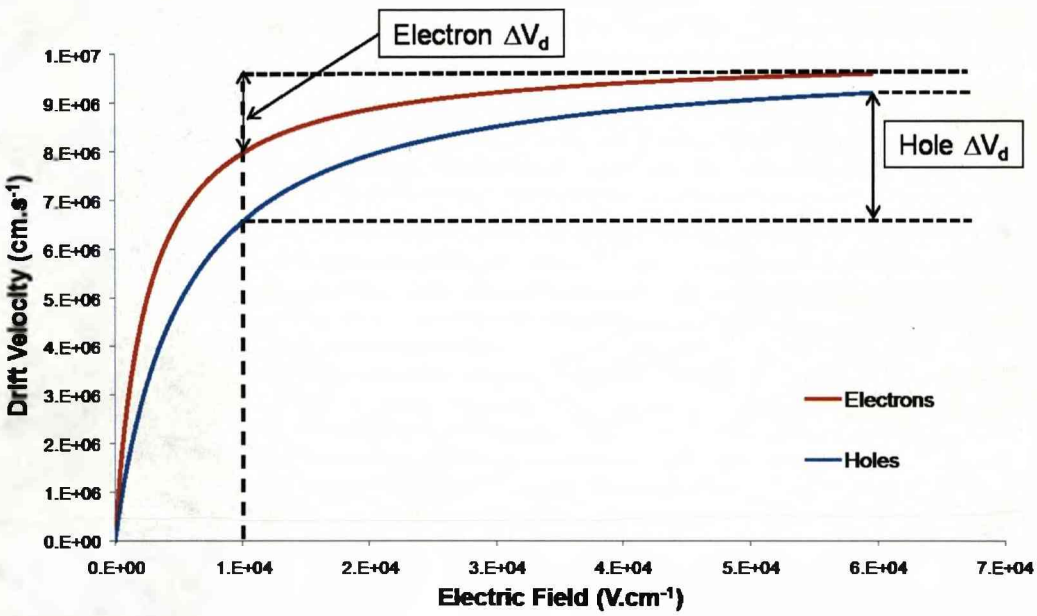

Figure 4.21: Graph describing the saturation of charge carrier drift velocities with increasing electric field strength in germanium. On the graph is highlighted the respective drift velocity differences between the carrier drift velocities and their saturation velocities at a finite value of electric field below that required to saturate the carrier drift velocity. It can be seen that this difference is greater for the hole species than for the electron species.

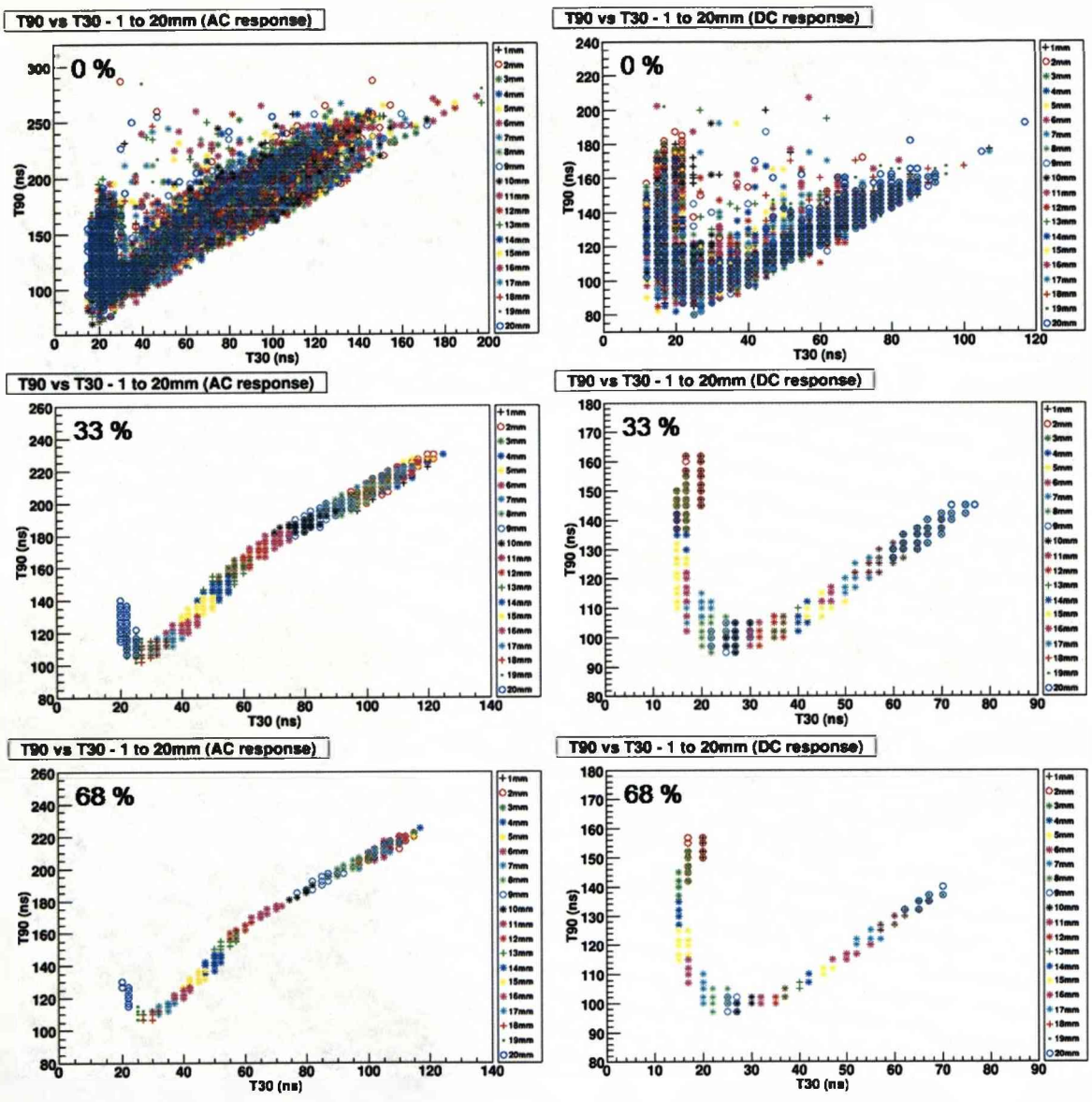

Figure 4.22: T30 versus T90 distributions with differing levels of frequency cut for each millimeter from the DC face to the AC face. The plots to the left are from the AC06 contact, and the plots to the right belong to the DC06 contact. Top: distributions with no frequency cut applied. Centre: intensity cut equivalent to 33 percent of the counts contained in the modal bin in each distribution applied. Bottom: intensity cut equivalent to 68 percent of the counts contained in the modal bin in each distribution applied.

range, but instead was more localised to a finite area. There was still a significant overlap between the distributions from each depth, and so the intensity cut was increased further. It must be noted that although increasing the intensity cut allows greater localisation of the events, this increased frequency requirement also reduces the number of total events available, ultimately reducing the efficiency of the Compton camera. By a process of trial and improvement it was decided that an intensity cut of 68 percent (seen in Figure 4.22, bottom) of the number of counts contained in the modal bin reduced the gate overlap whilst not significantly decreasing the amount of events available. Although the reduction in the number of events is undesirable, it is a necessary consequence if the position sensitivity is to be refined beyond the 4mm value obtainable at present toward the target of 1mm position sensitivity.

4.2.2 T30T90 gate creation

To allocate depths to any interaction in the detector, ranges of T30 and T90 values need to be defined for each individual depth. This is done by creating a polygonal gate around the frequency cut distribution and subsequently using the gate coordinates to assign a depth(s) to an interaction. Polygonal gates were created for each depth for responses from both the AC06 and DC06 contact using the ROOT analysis package [ROO07]. To gauge an initial idea of the sensitivity of this method, the sidescan data was selected using the polygonal gates for one scan line through the depth. For each scan depth the number of events that satisfied each gate were recorded.

Figure 4.23 shows the maximum number of gates triggered for any one event at each depth for a strip from each face (AC06 and DC06). Again, 1 mm corresponds to the scan position by the DC face and 20 mm to the scan position by the AC face. From the plot it can be seen that as the interactions moved through the depth of the detector, the sensitivity became comparable (after about 10 mm from the DC face), however for most depths the DC gates still showed superior sensitivity. A limitation of Figure 4.23 is that it does not show how frequent each gate, or set of gates, were triggered for

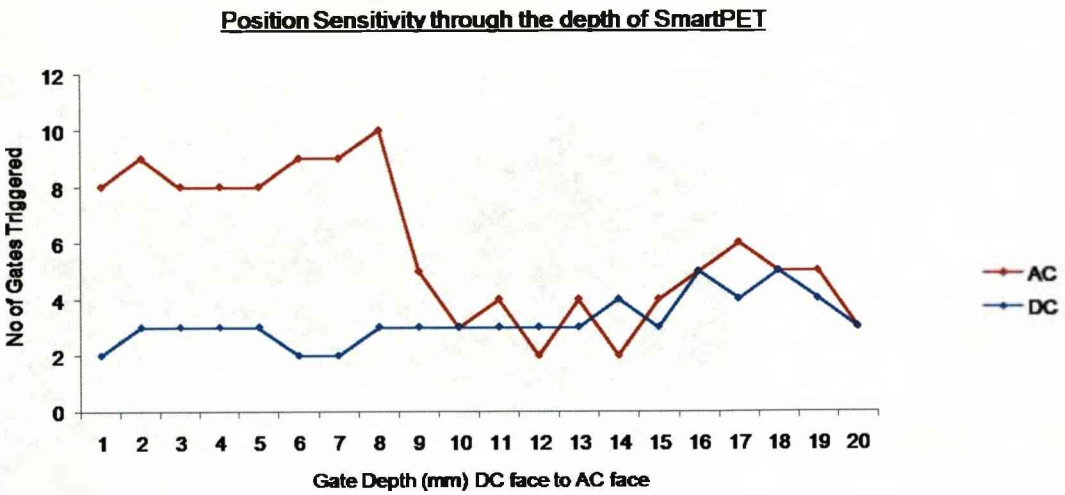

Figure 4.23: Graph showing basic sensitivity associated with the triggering of any one T30T90 polygonal depth gate from each face. This shows the maximum number of gates that were triggered by any one event from each scan depth.

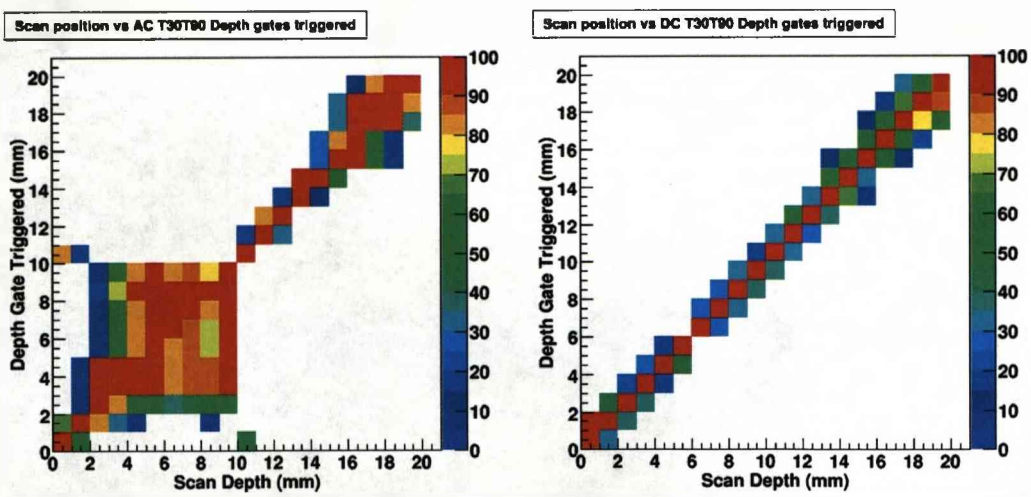

Figure 4.24: Percentage of events occurring in each of the T30T90 gates from each face triggered as the collimated 662 keV photons move from the DC face (0 mm) to the AC face(20 mm). This plot illustrates the distribution of the events used to create figure 4.23 throughout the gates for each scan depth.

a given number of events. To show the relative triggering of one gate with respect to its neighbours Figure 4.24 was created. This plot shows the normalised distribution of events through the range of depth gates triggered at each depth. For the AC response it can be seen that there was a significant spread of events through several neighbouring gates between depths 1 and 10 mm, confirming the information seen in Figure 4.23 that for the AC response, this region of the detector is insensitive. For the depths from 10 mm to 14 mm there was a good sensitivity (only one or two neighbouring gates triggered along with the depth gate belonging to that depth). However this sensitivity degraded as the scan depth progresses toward the AC contact. The DC response exhibited a good sensitivity throughout the detector depth. For scan depths 1 to 13 mm, only the gates belonging to the depths either side of the scan depth were triggered (3 mm depth of interaction sensitivity), and with a much reduced intensity compared to the gate for that depth, indicating that there was a large fraction of events only triggering the gate for that scan depth (1 mm depth of interaction sensitivity). Between depths 14 and 20 there was never more than two gates triggered either side of the gate for that depth. Depths 15 and 18 exhibit the poorest sensitivity, with 5 gates each triggering (5 mm sensitivity). The remaining depths between 14 mm and 20 mm achieved between 3 and 4 mm depth of interaction sensitivity.

These plots indicate that the contacts most sensitive to the pulseshape change with respect to depth belonged to the DC coupled face, hence the gates derived from the DC response were used to assign a depth to an event.

4.2.3 Detector Risetime Uniformity

The analysis presented so far corresponds to pulseshapes collected from the centre of the detector, i.e. those occurring in the effective voxel created by strips AC06 and DC06 (Figure 4.12). The response at the edges of the detector differs to that of the main body of the detector, possibly due to distortions in the electric field toward the edges of the detector. To determine which combinations of contacts need separate

gates, T30 and T90 plots were created of the average pulses from each position through the depth. Figure 4.25 shows the average risetime responses from the corner pixels and for the DC gated pixels along the AC06 contact.

Figure 4.25 a), shows the T90 response from each DC strip from fold 1 full energy events in the region of the detector gated by the particular DC strip and strip AC06, effectively describing the general DC response from the centre of each DC strip. It can be seen that the strips toward the edges of the detector (DC01, DC02, DC10, DC12) had a slightly slower risetime response than those through the main bulk of the detector (DC03 - DC09). This was speculated to be due to the differences in the electric field toward the edges of the detector. Figure 4.25 d), shows the DC T30 response from each DC strip from fold 1 full energy events, in the region of the detector gated by the particular DC strip and strip AC06 (as in Figure 4.25 a). Whereas in a) there was a differing response throughout the depth for the areas near the edge, the T30 response in d) only differs in the last 5 mm (16 to 20 mm).

Figure 4.25 b) shows the DC T90 response at the corner pixels. It can be seen that the response was different for each corner at most depths. Figure 4.25 c) shows the DC T30 response at the corner pixels. As with the response from the centre of the strips, the T30 differences for the corner pixels only become apparent toward the AC contact (i.e. 16 to 20mm). Why the T30 response for the strips by the edges of the detector only differs from the bulk response for the 5 mm by the AC face is not known; however speculation can be aimed toward amounts of induced charge forming the initial rise of the pulse. The differing electric field present in the edge strips will affect the induced nature of the pulse and it is in this induced portion of the pulse that the edge effects will be manifested. The T30 value is calculated by subtracting the time at 10 % of the final pulse magnitude from the time at 30 % final pulse magnitude. In order for a difference between the response observed from the edge strips and that seen from the bulk strips, this induced portion of the pulse must be generated after 10 % of

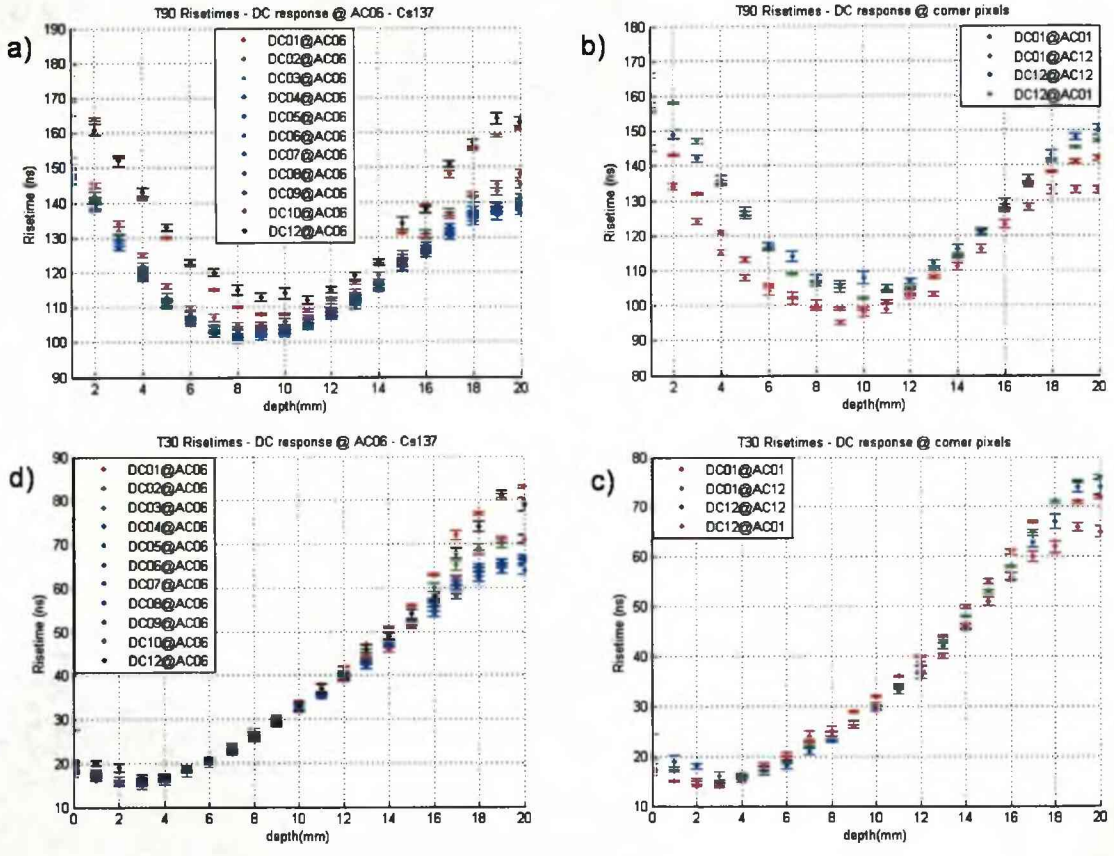

Figure 4.25: Differing risetime responses as a function of position of interaction across the front face of the detector. The risetime response from those strips away from the edges of the detector exhibit a similar behaviour to each other and as a result are coloured the same (blue). The responses of those strips by the edges differ to those strips situated away from the edges and are coloured separately to highlight this observation.

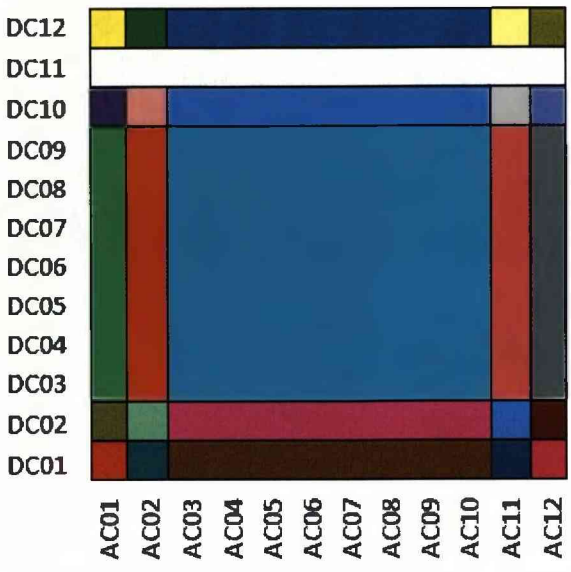

Figure 4.26: Diagram to highlight regions of the detector with differing pulseshape response. Regions belonging to that of a different colour require separate risetime gates.

the magnitude has been reached. If the induced charge is created before 10 %, then the region of the pulse between 10 % and 30 % will simply correspond to the charge species collection, which yields a linear charge collection containing no characteristics with which one could distinguish a given pulse from another. As the induced charge is a function of distance from the collecting electrode, it is speculated that unless the charge species is created at a sufficient distance from the collecting DC contact whereby the induced charge contributes more than 10 % of the pulse magnitude, then all of the induced charge will have occurred prior to the T10 value, and as such the T30 values will be similar to that observed in the bulk region. When considering this statement in conjunction with figure above (d), it can be assumed that the distance from the DC contact at which the charge species must be formed is approximately 16mm.

Figure 4.26 is a diagram representing the front face of the SmartPET detector. The strips from each face have been labeled. Each colour seen on the diagram corresponds

to an area of differing risetime response and so required a unique set of polygonal gates. The pixels in the main bulk of the detector (turquoise) all displayed a similar response, and so could share the same gates, however, edge and next-to-edge strips each needed individual sets of gates, along with separate gates again for the pixels at the corners and next to the corners. It can be seen that DC11 was been omitted from this stage of the analysis. It was observed in previous research [Tur06], [Coo07], that there is a problem with DC11 in the form of significant charge sharing, double peaking of the photopeak, long risetimes and significantly less statistics than observed in neighbouring strips. It was assumed that this is a problem with the electrical contact. For this reason it was decided to use the previous risetime gates (4mm sensitivity) used in [Coo07], for events occurring in this strip in the subsequent Compton camera measurement. The gates for the separate regions were created in ROOT [ROO07] and the coordinates of these gates were output to be used in subsequent analysis.

4.2.4 T30T90 Gate Test

Before the T30T90 gates were used on experimental Compton camera data, the gates needed to be assessed to validate that they performed as expected. To achieve this, the frequency of the gates triggered were plotted for photons incident through each face of the detector (AC and DC face), against a theoretical attenuation curve for photons of the same energy incident on the same face. It would be advantageous for the chosen energy of the photons to be significantly attenuated through the depth of SmartPET, as this would display a strong variation in intensity through the depth of the detector, allowing a more rigorous test to validate the proposed gates.

It can be seen from Figure 4.27 which was calculated using attenuation coefficients, that almost all 122 keV photons emitted from a ^{57}Co source are attenuated through a 20 mm thickness of germanium, and so it was decided to use photons from ^{57}Co for this purpose. The data used were from front face characterisation scans (on both AC and DC) faces, which were originally collected for characterisation purposes [Tur06]

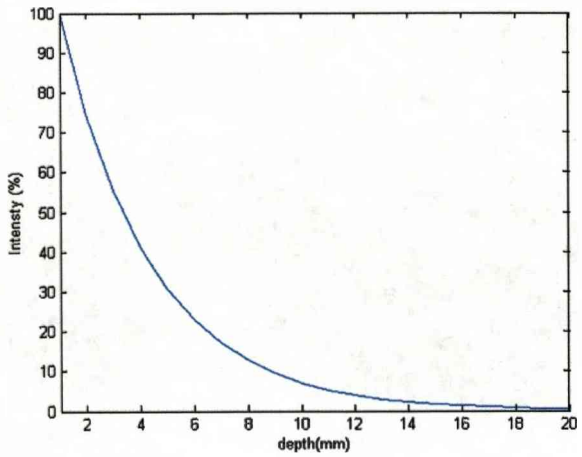

Figure 4.27: Calculated attenuation of 122 keV photons through 20 mm of germanium.

[Bos09], allowing the check to be done for higher statistics near both faces.

Figure 4.28 shows the relative intensity of events with which the gates for each depth were triggered with respect to the theoretical attenuation of ^{57}Co. In general they exhibited a good agreement with the attenuation curve, however this agreement diminished for interactions near either face. This was expected as the number of gates triggered increased toward each face (Figures 4.23 and 4.24).

4.2.5 T30T90 Risetime Gate Performance

The polygonal risetime gates created to select the events were very selective. It can be seen from Figure 4.22 that a large number of events present in the data will not trigger any of the gates created around the intensity cut data. The original T30T90 gates (4 mm depth sensitivity) used in [Coo07] encompassed the majority of the events. Table 4.1 quantifies what percentage of events triggered which gating category, to allow a comparison of the efficiency of each T30T90 gating method for photons incident on either face. 100000 photopeak events through each face were used. The trigger categories from table 4.1 refer to the different combinations of gates that the events can fall into.

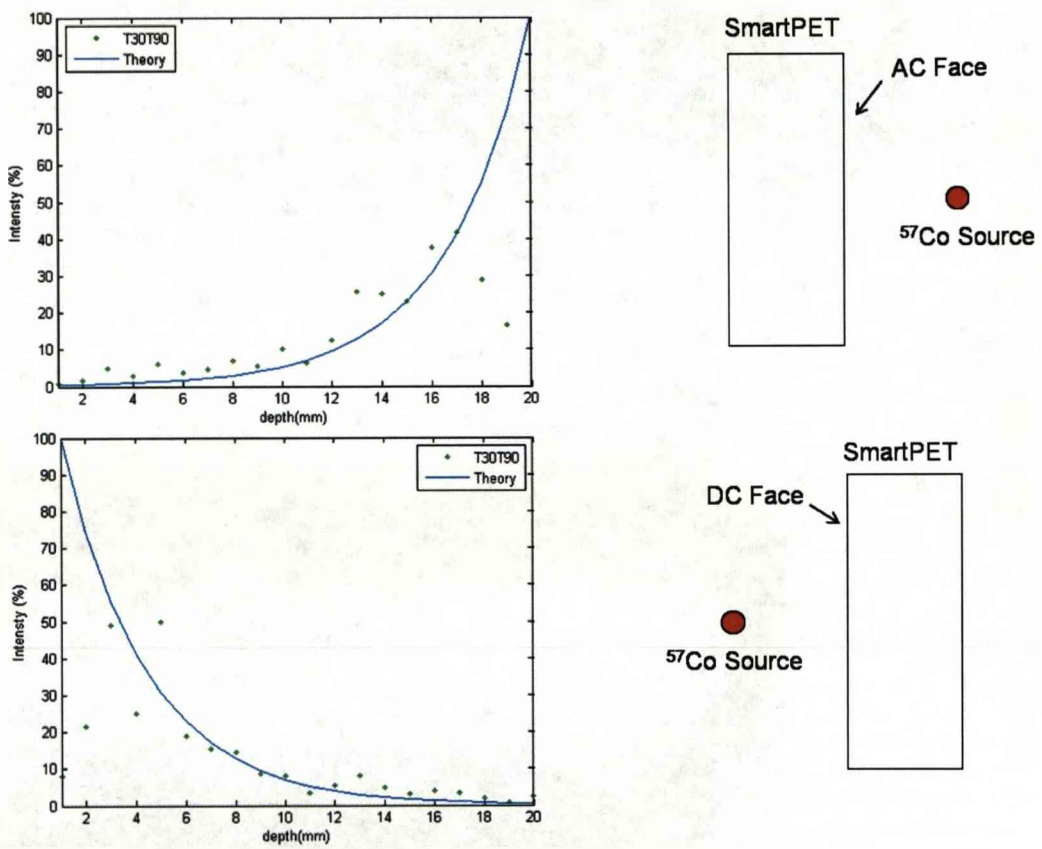

Figure 4.28: T30T90 gates triggered through the depth of SmartPET by 122 keV photons incident on the AC face (AC face = 20 mm, DC face = 1 mm). Top: Photons incident from the AC face. Bottom: Photons incident from the DC face. The blue curve represents the theoretical attenuation of ^{57}Co photons that would be expected when incident through each face.

Trigger Category	Incident on AC Face	Incident on DC Face
Original T30T90 Gates (AC and DC)	65639 (65.6 %)	74349 (74.5 %)
Original T30T90 DC Gates only	10224 (10.2 %)	17552 (17.6 %)
Original T30T90 AC Gates only	20542 (20.5 %)	6752 (6.8 %)
Not Triggering Any Gates	3595 (3.6 %)	1347 (1.5 %)
New T30T90 Gates	11286 (11.3 %)	31761 (31.8 %)

Table 4.1: Table comparing gates triggered (original T30T90 gates and new T30T90 gates). Photons are incident through either face. The percentage values are a percentage of 100,000 full energy, fold 1 events.

The category *Original T30T90 Gates (AC and DC)* shows the number of events that satisfy a gate from each contact in a fold 1 photopeak event for photons incident on each face, (as not all events will satisfy both a gate from an AC strip and a gate from a DC strip).

Original T30T90 DC Gates only again refers to the original gates, but for those events that only trigger the gates belonging to a DC strip.

Original T30T90 AC Gates only category is for events only triggering the original gates belonging to an AC strip.

Not Triggering Any Gates is for the events which do not trigger any gates, neither the original T30T90 nor new T30T90 gates.

New T30T90 Gates, is for the number of events that trigger one of the new T30T90 gates.

To determine what overall position sensitivity was achieved with this new T30T90 gating method, the number of gates triggered by each event was quantified. These numbers are represented in Table 4.2. From photons incident on the AC face, out of

the 11,286 accepted events, 3,789 of these triggered only 1 gate (1mm sensitivity), 5420 triggered two gates (2mm sensitivity), 1813 triggered 3 gates (3mm sensitivity) and 264 triggered 4 gates (4mm sensitivity). From photons incident on the DC face, out of the 31,761 accepted events, 18244 of these triggered only 1 gate (1mm sensitivity), 13057 triggered two gates (2mm sensitivity), 401 triggered 3 gates (3mm sensitivity) and 59 triggered 4 gates (4mm sensitivity).

No of T30T90 Gates Triggered	Photons incident on AC Face	Photons incident on DC Face
1	3789	18244
2	5420	13057
3	1813	401
4	264	59

Table 4.2: Table displaying the frequency of how many T30T90 gates were triggered per accepted event. The percentage value refers to the percentage of total triggers recorded from the new T30T90 gates.

The T30T90 method provided a working method to assign a depth to an interaction in SmartPET, with varying degrees of accuracy for different events in different regions of the detector. For the more sensitive DC response, the majority of interactions that triggered a gate triggered only one gate (see Figure 4.24), implying that for the majority of events that triggered this set of gates a depth sensitivity of 1mm is achievable. Table 4.2 shows the number of events that triggered the new T30T90 gates for 1, 2, 3 and 4 mm sensitivity. The target of 1 mm sensitivity was achieved by 3,789 events through the AC face and 18,244 events through the DC face. For the AC face this equates to 3.8 % of the total number of incident events and 33.6 % of the total number of events triggering any of the New T30T90 gates. Similarly, for the DC face, 18.2 % of the total 100,000 events and 54.4 % of the events satisfying any of the New T30T90 gates, incident through the DC face achieved a position sensitivity of 1 mm.

4.2.6 T50 Time Difference Method

Another method of employing risetimes for depth of interaction determination is the Time Difference Method. This method uses the difference between the arrival time of holes to the negative AC contacts and electrons to the positive DC contacts to assign a depth to an interaction. If the arrival of the electrons occurs prior to that of the holes, the interaction event must have taken place closer to the electron-collecting DC contacts. Similarly, if the holes are detected before the electrons, the event must have occurred closer to the hole-collecting AC contacts. The parameter used to apply this method is the T50 parameter, i.e. the time taken for the pulse to rise from 10 percent of its final magnitude to 50 percent of its final magnitude. The value of 50 percent is chosen as this is generally accepted to be the point of steepest slope on the pulse indicating the moment that the charge carriers arrive at the detector electrodes, providing the best timing properties [Mih04]. This method is illustrated in Figure 4.29 for events recorded by each face and in the centre.

Figure 4.30 shows the normalised frequency of the time difference values calculated at each scan depth. It can be seen that for any one depth across the x axis there are time difference values across almost the full range of possible values along the y axis. In order to constrain the range of T50 time difference values that correspond to a particular depth, and hence reduce overlap with neighbouring scan depth values, an intensity cut needed to be introduced as implemented in the T30T90 analysis. The fewer scan depths that a given T50 time difference value satisfies, the greater the position sensitivity assigned to that event.

As was seen previously in the T30T90 analysis, the intensity of counts recorded at a given depth varied from one depth to the next, therefore each depth required an individual value for the intensity cut. This value was set at a fraction of the highest intensity of counts observed from the range of time difference values for each depth. Figure 4.31 shows the T50 time difference distribution as the intensity cut was

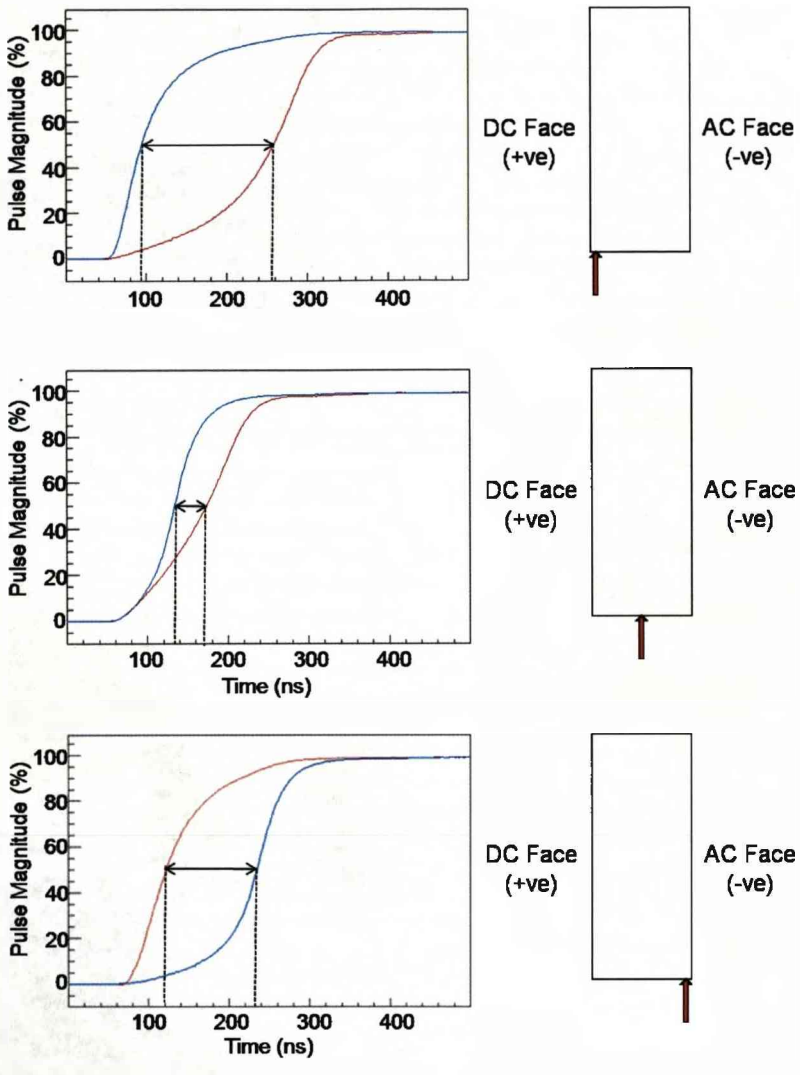

Figure 4.29: Plots showing an average pulseshape from a strip on each face (AC06 and DC06), at the scan position of 1mm (top), 10mm (center) and 20mm (bottom) from the DC face. The blue pulses are average pulses created at the DC face, and the red pulses are the average pulses created at the AC face. The arrows between the pulses are at 50 percent of the total pulse magnitude. The diagrams to the right of each plot are to illustrate the direction of the collimated beam (red arrows) of photons with respect to the detector faces. It is the time difference calculated between the T50 values of pulses generated at strips on opposite faces which will be used to calibrate the depth of interaction.

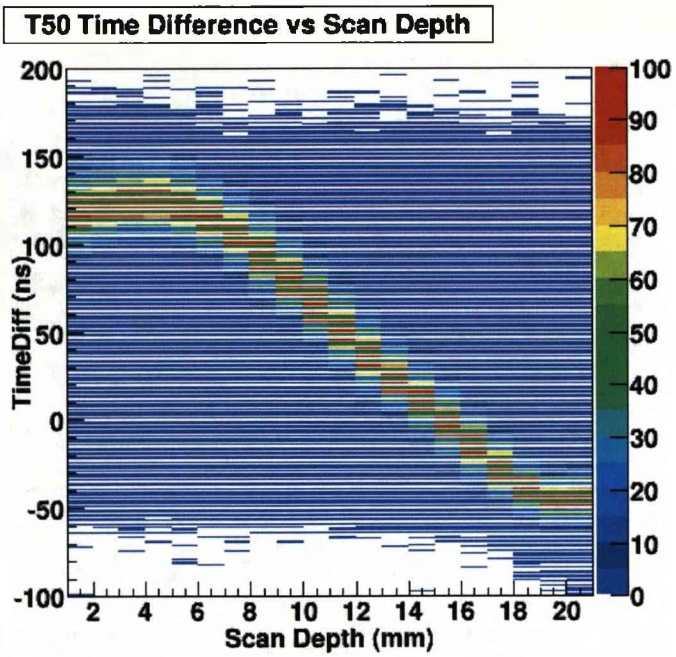

Figure 4.30: Distribution of the T50 time difference values as a function of depth.

increased from 20 percent of the number of counts in the modal bin (top left), to 40 percent (top right), to 60 percent (bottom right) and to eighty percent (bottom left). Ideally there would be no overlap between any of the range of depths, and this would be perceived as 1 mm position sensitivity. From the 20 percent cut, there was a reasonably localised range of time difference values for each depth when compared to no cut (Figure 4.30) however a significant overlap with ranges from other several other depths can be observed for any one depth. This overlap was slightly reduced for the 40 percent cut but it was still common for a given range to overlap those from at least two depths in either direction. For the 60 percent cut it can be seen that the majority of ranges only overlapped their nearest neighbours. A further cut of 80 percent was applied to the data. This cut showed no overlap between ranges of values for most of the depths and was expected provide the desired 1 mm sensitivity for the majority of interactions that fall within the gates. However, the issue of how many events would actually have values within any of the gates was a concern, as the range

of values acceptable has been severely diminished. As with the determination of the new T30T90 gates earlier in the chapter, the trade off between efficiency (number of events accepted) and accuracy of their position determination is an important factor in deciding on the level of intensity cut to be applied. The 60 percent cut was decided as the best level of cut to address this issue as it was deemed to offer a high level of position sensitivity (less overlap with neighbouring ranges when compare with lower level frequency cuts) and displayed only a slightly reduced range of possible values for each depth, when compared to other levels of intensity cut.

It can be seen from Figures 4.32 and 4.33 that the T50 gates have a poor sensitivity up to 7 mm from the DC face, in agreement with the significant overlap of time difference ranges observed in Figures 4.30 and 4.31. However they have a good sensitivity between 8 mm and 17 mm (i.e. majority of events localised to 1 mm and no gates beyond the adjacent gates ever triggered), and between 18 mm and 20 mm the sensitivity is usually 2 mm (i.e. most events fall in gate 19 or 20).

As was shown earlier in the chapter, the pulse shape response is not uniform for all areas of the detector, therefore T50 gates have been determined for each region where the pulseshape response has been shown to differ (see Figure 4.26).

4.2.7 T50 Gate Test

Prior to applying the T50 gates to Compton camera data a validation was needed to confirm that the gates performed as expected. As with the T30T90 gate test, this was done by comparing the frequency of the gates triggered to the theoretical attenuation of ^{57}Co photons incident on a front face of the detector (AC or DC face). The events used from the data were photopeak gated, fold 1 events.

Figure 4.34 plots the T50 gates triggered against the ^{57}Co attenuation curve. It can be seen that there was a reasonable agreement up to the last 3 mm by the AC contact

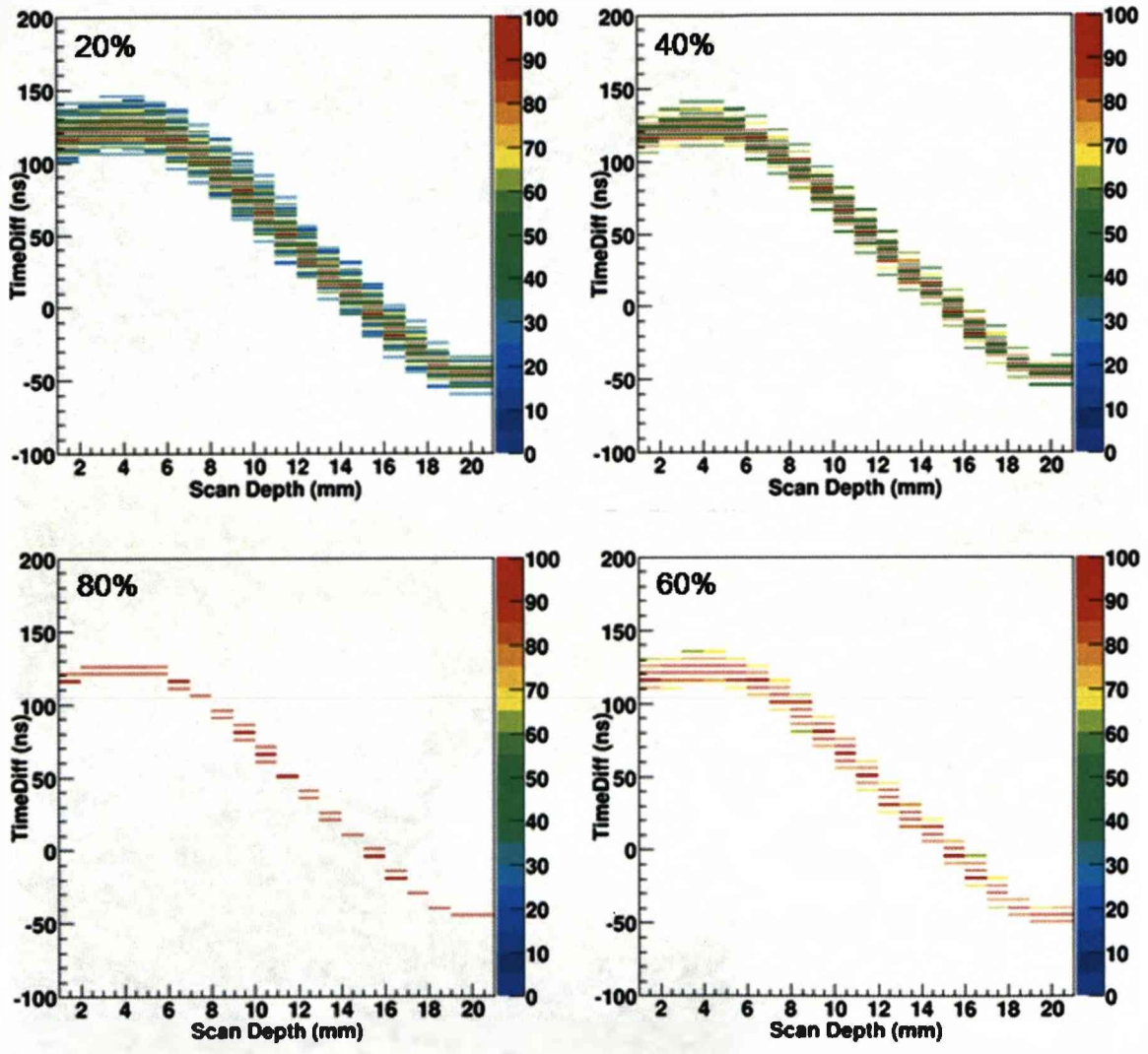

Figure 4.31: Distribution of the T50 time difference values with differing frequency cuts applied. Each cut is defined as a percentage of the maximum counts in any one bin for that particular depth.

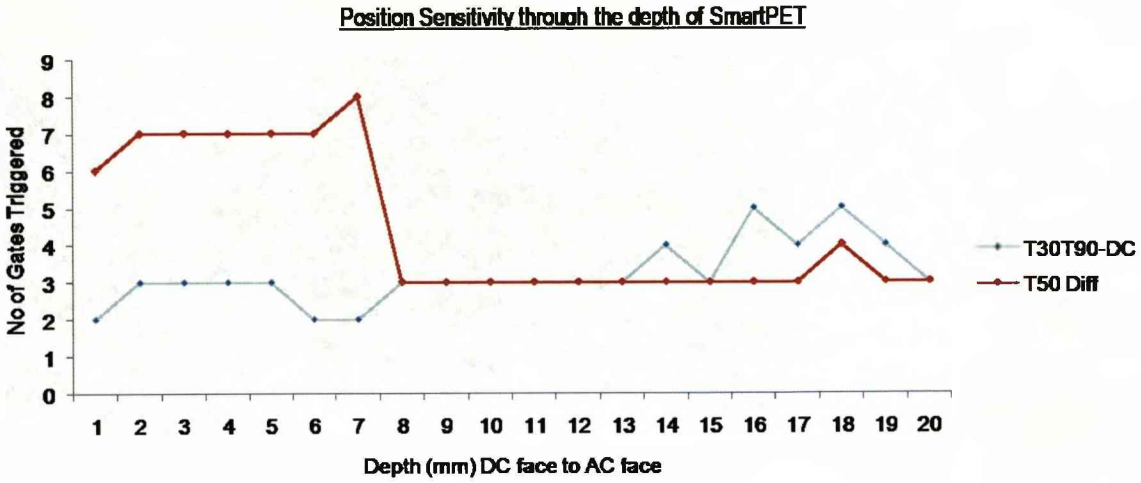

Figure 4.32: Comparison of the number of gates triggered as a function of scan depth for the 60 percent frequency filtered T50 time difference and T30T90 (DC response) methods.

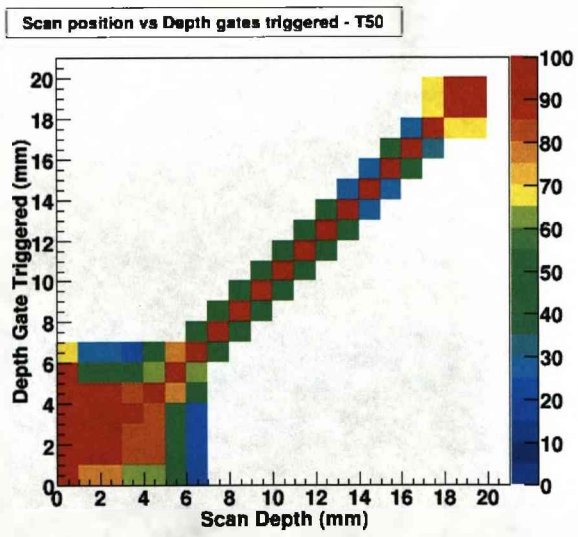

Figure 4.33: Percentage of events occurring in each of the T50 gates as the scan moves from the DC face (1 mm) to the AC face (20 mm). This graph illustrates the distribution of the events used to plot the T50 gates triggered in Figure 4.32 for each scan depth.

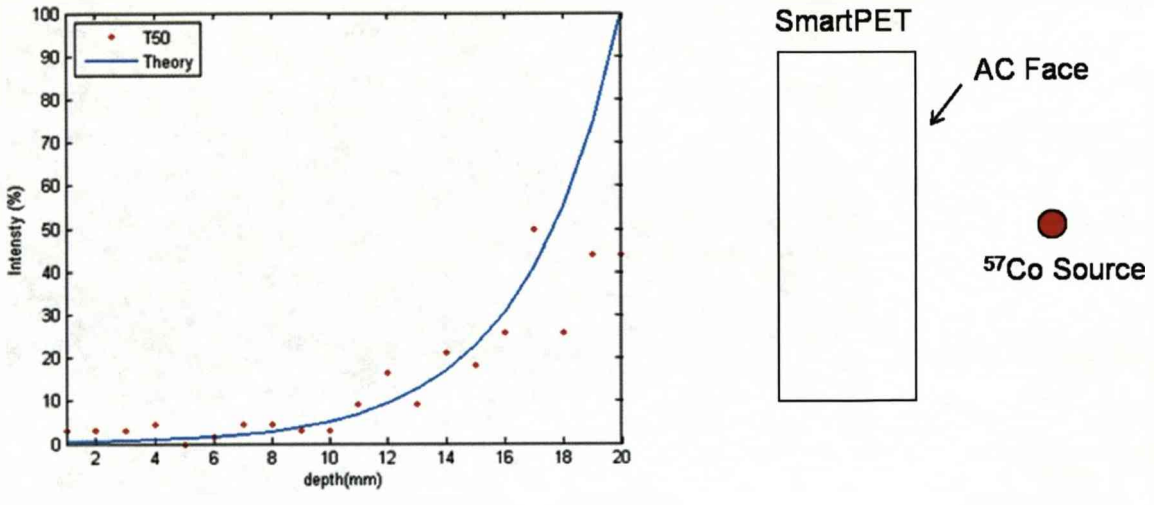

Figure 4.34: T50 time difference gates triggered from ^{57}Co photons incident on the AC face. (DC face = 1 mm, AC face = 20 mm). The blue curve represents the theoretical attenuation of ^{57}Co photons that would be expected when incident through the AC face.

(depths 18,19 and 20 mm). Figure 4.35 shows the T50 gates gates triggered when the ^{57}Co photons were incident on the DC face. In order to show the regions of agreement more clearly the plot has been shown in two parts; a) The full plot range; it can be seen that there was poor agreement from 1 mm to 7 mm from the DC face. b) From 8 mm to 20 mm; the triggered gates followed the desired trend.

As with the T30T90 gates, a basic efficiency for this method compared to the original T30T90 gates (4 mm sensitivity), can be quantified. The numbers of events from a data set of 100000 photopeak events are summarised in table 4.1.

As with the T30T90 method, the number of events satisfying each value of position sensitivity through depth have been determined. Again, this was done by quantifying how many of the depth gates were triggered by each event. These numbers are presented in Table 4.4.

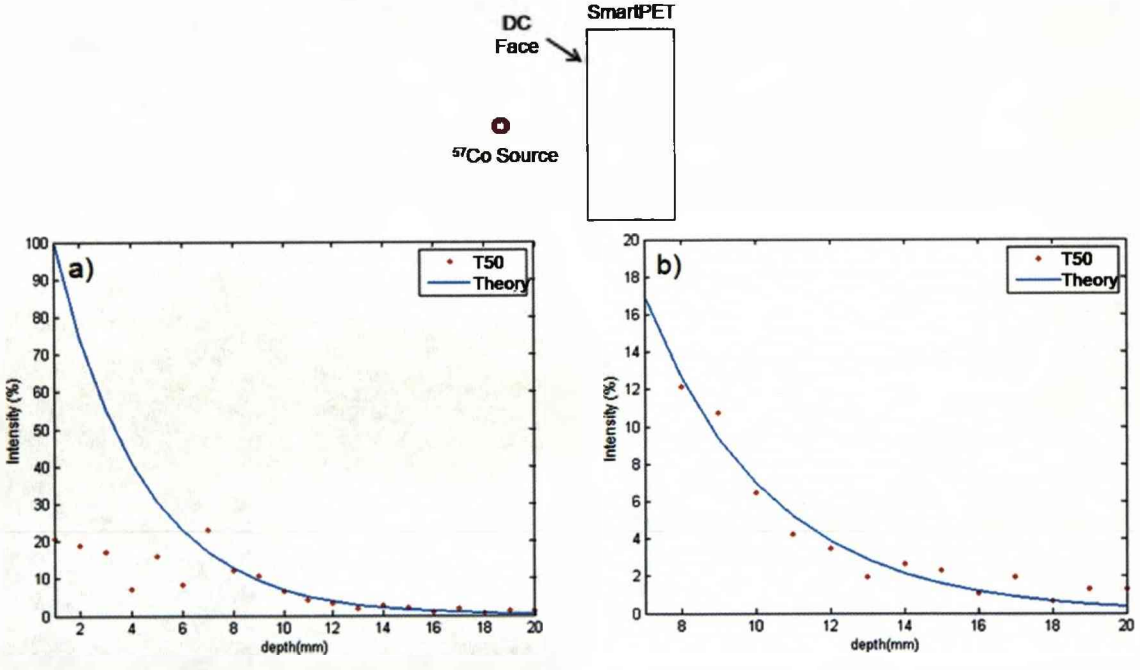

Figure 4.35: Percentage of events occurring in each of the T50 gates from ^{57}Co photons incident on the DC face. DC face (1 mm), AC face (20 mm). The blue curve represents the theoretical attenuation of ^{57}Co photons that would be expected when incident through the DC face.

Trigger Category	Incident on AC Face	Incident on DC Face
Original T30T90 Gates (AC and DC gates)	65639 (65.6 %)	74349 (74.5 %)
Original T30T90 DC Gates only	10224 (10.2 %)	17552 (17.6 %)
Original T30T90 AC Gates only	20542 (20.5 %)	6752 (6.8 %)
Not Triggering Any Original T30T90 Gates	3595 (3.6 %)	1347 (1.5 %)
T50 Gates	34177 (34.2 %)	58834 (58.8 %)

Table 4.3: Table comparing gates triggered (original T30T90 gates and T50 time difference gates). Photons are incident through either face. The percentage values represent the fraction of the total 100,000 full energy, fold 1 events used.

No of T50 Gates Triggered	Photons incident on AC Face	Photons incident on DC Face
1	15407(45.1 %)	17177(29.2 %)
2	13392(39.2 %)	20455(34.8 %)
3	4604(13.5 %)	5081(8.6 %)
4	192(0.56 %)	4363(7.4 %)
5	215(0.63 %)	4696(8.0 %)
6	243(0.71 %)	4677(8.0 %)
7	125(0.37 %)	2385(4.1 %)

Table 4.4: Table displaying the frequency of how many T50 gates were triggered per accepted event.

Figure 4.36 shows the percentage of events through either face that satisfy any of the three sets of gates (original T30T90, new T30T90 and T50 time difference method). It can be seen that for each of the gating methods, photons incident through the AC face initiate more triggers than when incident through the DC face.

Figure 4.37 shows the depth sensitivity achieved by each of the methods developed in this chapter; the new T30T90 gates and the T50 time difference method. For the T30T90 gates, 18.2 percent of the events through the DC face and 3.8 percent of the

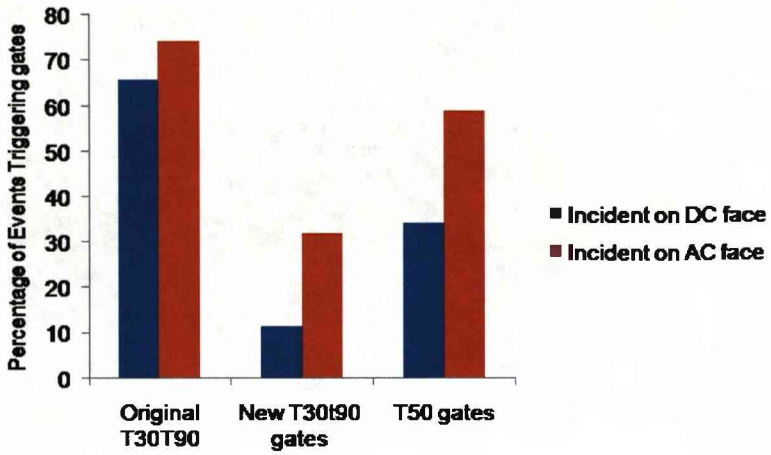

Figure 4.36: Histogram to show the percentage of events incident through either face which trigger the gates from the three different sets of gates (original T30T90, new T30T90 and T50 time difference method).

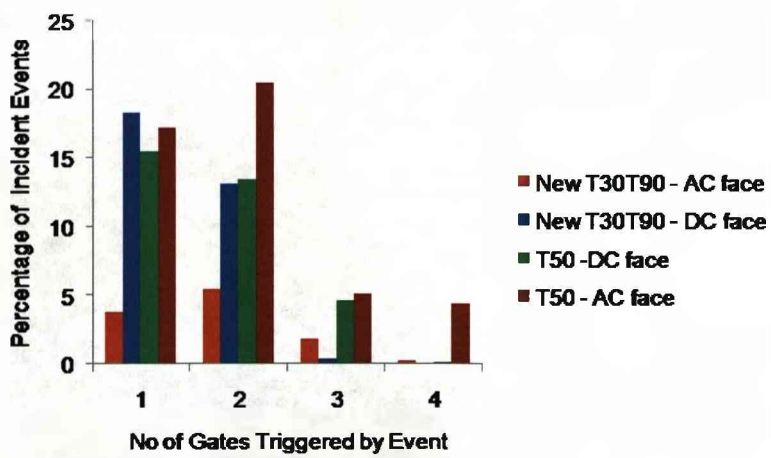

Figure 4.37: Histogram to show the position sensitivity of the gating methods investigated in this chapter. Each gate represents millimeter in depth, and so the number of gates triggered for any one event indicates the position sensitivity with which the interaction position can be determined.

events through the AC face achieved 1 mm position sensitivity. For the time difference method, 17.2 percent of events through the DC face and 15.4 percent of events through the AC face achieved 1 mm position sensitivity. A greater percentage of events incident on the DC face of the detector achieved a depth sensitivity of 1 mm compared to those through the AC face. This was expected from earlier observations (Figures 4.23, 4.24, 4.24 and 4.33) which show a reduced sensitivity for interactions in close proximity to the AC contacts for both methods. It is not clear why this is the case. Suggested reasons include the variation of impurity concentration by up to 5 percent through the depth of SmartPET and poor AC contact performance, both of which could degrade the charge carrier transport properties.

Two methods, constant fraction (T30T90) and time difference (T50), have been investigated using data acquired from collimated side and face scans. For both methods it has been demonstrated that for most of the events that trigger any one of the gates, only one gate is triggered (Figure 4.37), implying that the depth of interaction sensitivity is 1 mm for the majority of the events triggering these new gates.

It was not clear at this stage which method should be ultimately be employed for Compton camera data analysis. Both methods provided comparable efficiency with a similar depth sensitivity, however for the depth region between 1 to 7mm from the DC face the T30T90 method for the DC response was the more accurate of the two. In this region of the detector (1 - 7 mm from the DC face) any method using an AC pulseshape response, i.e. T30T90 AC gates and T50 time difference method, provided a low level of position sensitivity (typically 7 mm sensitivity, shown by Figures 4.32 and 4.33). It is not clear why this was the case. The response from both faces for both methods generally exhibited the optimum sensitivity toward the centre of the detector, and for both responses sensitivity became poorer toward the AC face. The degradation toward the AC face was also observed in [Tur06], where it was suggested that the possible 5 percent difference in impurity concentration through the depth of

the detector could be responsible.

In the following chapter the gates derived from these methods will be applied to experimental Compton camera data, allowing a more thorough evaluation by quantifying their effect on image quality.

Chapter 5

Germanium Compton Camera

This chapter describes the germanium Compton camera setup, using two SmartPET detectors, and the measurements taken in order to evaluate the effect of pulse shape analysis on the position resolution of the image. The data was presorted and then reconstructed using an analytical back projection algorithm.

5.1 Data Acquisition System

The two SmartPET detectors were mounted in a rotating gantry which was specifically designed to hold and rotate the detectors for PET measurements [Coo07]. In Compton camera mode, the detectors remain static and the source was positioned to one side of the detector pair, with SmartPET 1 positioned closest to the source. The two detectors were operated in coincidence with a time window of 100 ns. Both detectors were triggered using conventional NIM electronics as described in earlier chapters. The data acquisition setup of the SmartPET Compton camera system is shown in Figure 5.1. GRT4 cards were again used to acquire the data digitally, however the sample size for each event was reduced to 128 samples, as opposed to 256 samples per event for SmartPET data collected in Chapter Four which increased the rate of data acquisition by a factor of two.

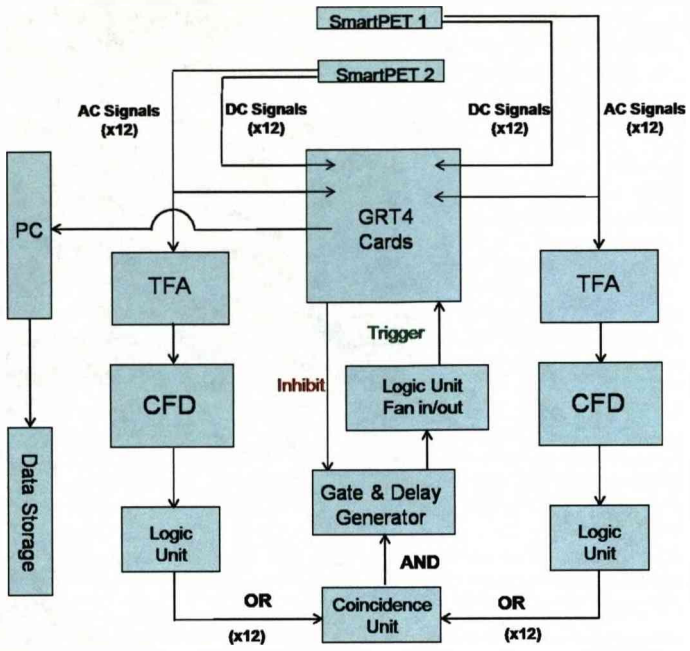

Figure 5.1: Diagram of the acquisition setup of the SmartPET Compton camera.

5.2 Analysis methods

Prior to reconstruction, the raw data needed to be presorted to a text file using the MT Sort programming language, to select and output the information required by the reconstruction algorithm. The interaction criteria for events to qualify for reconstruction are:-

- A fold 1 event (a single strip firing on each face) in each detector.
- The energy deposited in both detectors sums to the gamma ray energy, i.e. the event consists of a Compton scatter in the scatter detector (SmartPET 1) and the scattered photon is stopped in the absorber detector.

For each event, the following information was output on a row of the text file, totaling 21 columns:

1. Event number

2. AC channel number (SPET1)
3. Lateral position of interaction within that strip
4. Risetime number
5. Energy deposited - Digital GRT4 energy
6. DC channel (SPET1)
7. Lateral position of interaction
8. Risetime number
9. Energy deposited
10. AC channel (SPET2)
11. Lateral position of interaction within that strip
12. Risetime number
13. Energy deposited
14. DC channel (SPET2)
15. Lateral position of interaction within that strip
16. Risetime number
17. Energy deposited
18. New risetime gate (SPET1)
19. No of new risetime gates triggered by the current event (SPET1)
20. New risetime gate (SPET2)
21. No of new risetime gates triggered by the current event (SPET2)

where the *Lateral position of interaction within that strip* is calculated using the asymmetry parameter, *Risetime number* is a number between 1 and 5 assigned using the original gates referred to in [Coo07]. Each number corresponds to a 4mm region of depth, where 1 equals 1mm to 4mm depth, 2 equals 5mm to 8mm depth, 3 equals 9mm to 12mm depth, 4 equals 13mm to 16mm depth and 5 equals 17mm to 20mm depth. This is calculated for each face in each detector. The *New risetime gate* is the depth gate assigned using the methods described in Chapter Four. These can be either the T30T90 gates, or the T50 time difference gates (separate sorts are run to apply the two methods). *No of new risetime gates triggered by the current event* is the number of gates triggered by the event and is used to adjust the interaction position to the centre of the group of gates triggered.

5.3 Compton camera imaging

A reconstruction algorithm must be used to create images from the sorted data. The back projection algorithm was originally developed in MATLAB by Scraggs [Scr07] to reconstruct both simulated data, which was used for validation, and experimental data acquired with the SmartPET system. The term *back projection* is typically applied to a Compton reconstruction code which does not employ any method of enhancing the image by either applying a filter, or using an iterative approach. These methods have the potential to reduce blurring due to false intersections close to the position of the actual source and improve the spatial sensitivity of the resultant image. The simple nature of the code is expected to provide a more robust method to test the effect of the position of interaction sensitivity. This is because no filter or iterative method is used which could reduce the effect of incorrect location of the source. As discussed in Chapter Two, an image is created via the construction of a cone projected into space for many events, with the point at which the cones intersect being the location of the source.

5.3.1 Cone creation

The selected data described in the above section 5.2 was input to the MATLAB reconstruction code and interpreted to position each of the interactions in 3D space using a cartesian co-ordinate system. The 3D space set up in MATLAB was a 500 × 500 × 200 matrix, corresponding to an x, y, and z axis, defining the volume into which the cone will be projected. The angle of the cone apex is double the angle of scatter, which is calculated from the energy deposited in both detectors, using the Compton scatter formula 5.1.

$$\cos\theta = 1 - m_0c^2\left(\frac{1}{E_2} - \frac{1}{E_1 + E_2}\right). \tag{5.1}$$

This angle will then be used to construct the cone into the defined volume. The equation describing a cone is

$$\frac{(x - x_0)^2 + (y - y_0)^2}{[\tan(\frac{\theta}{2})]^2} = (z - z_0)^2 \tag{5.2}$$

where x, y and z are the co-ordinates of a single point on the cone and x_0, y_0 and z_0 are the co-ordinates of the interaction position in the scatter detector where the cone apex is to be situated, shown in Figure 5.2. The equation is then simplified resulting in a single variable. As stated earlier, the volume into which the cone will be reconstructed is a $500(x) \times 500(y) \times 200(z)$ matrix. The equation is solved in the algorithm by calculating all points of the cone present in each of the two hundred 500 x 500 matrices. This is illustrated in Figure 5.2, where the black rings correspond to the surface of the reconstructed cone at a particular z plane.

When the cone is initially created its apex is situated on the point of interaction in the scatter detector. The cone is orientated in such a way that a line between the cone apex and the centre of the cone base is parallel with the z axis. This line is known as the cone axis, and in order for the reconstruction to be correct it must be parallel

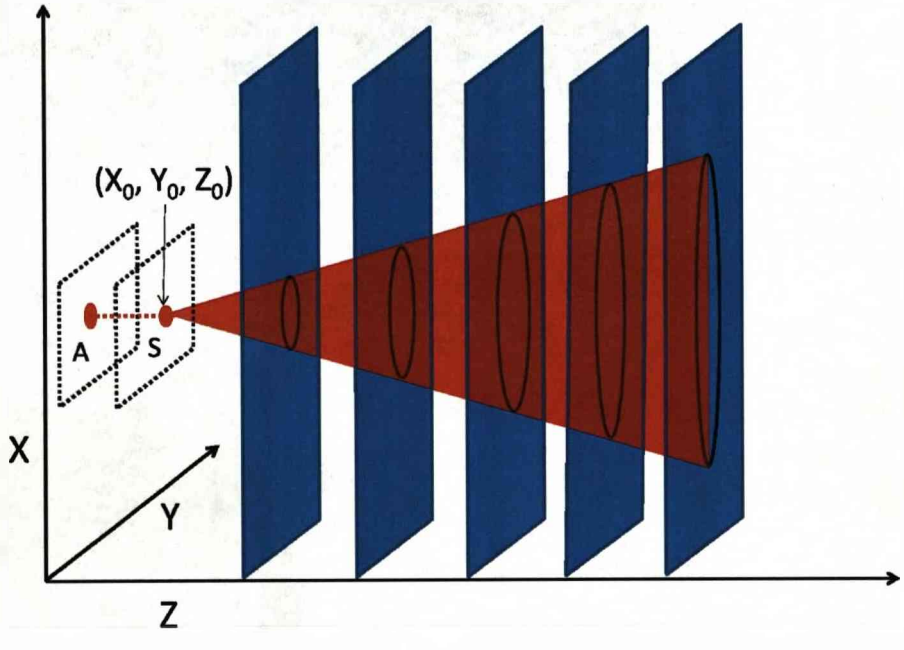

Figure 5.2: Diagram to visualise the process of cone beam reconstruction. A scatter and an absorption are represented by the red ovals in the detectors (marked 'S' for scatter detector and 'A' for absorber detector). The dashed red line between the two interactions reveals the path of the scattered photon. The large red triangle represents the cone that would be reconstructed as a result of these interactions. The blue squares represent hypothetical planes normal to the z axis. The points on these planes that are intersected by the cone are shown as the black rings. Any one reconstruction in the xy plane will in effect be an overlap of many of the black rings, each one originating from an individual event.

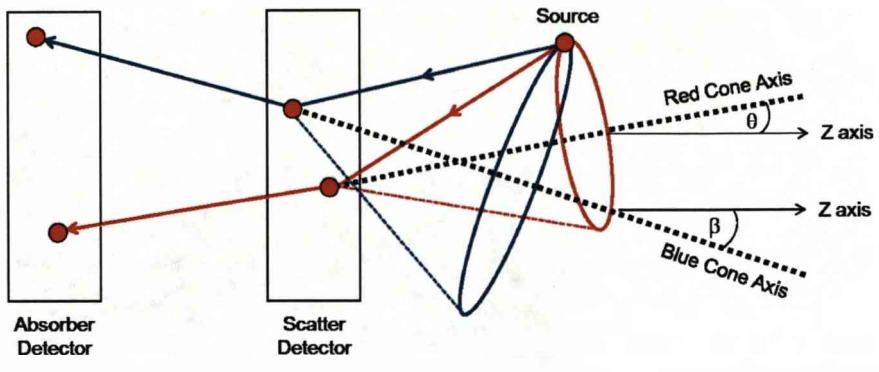

Figure 5.3: Diagram to show how cones may be created at angles to the Z axis. The cone axis must be angled parallel to the vector created between the two interactions, which will likely not be parallel to the Z axis.

to the vector between the two interaction points. The angles of both elevation and azimuth that this vector makes with the z axis are calculated, and the direction of the cone altered accordingly. Figure 5.3 shows two cones created from photons emitted from the same source to demonstrate different directions of the reconstructed cone with respect to the horizontal z axis.

5.4 Experimental Reconstructions

For each data set, several reconstructions were conducted, with each reconstruction employing differing levels of PSA. This was intended to allow image comparisons not only between images produced by applying the depth sensitivity methods developed in Chapter Four, but also to provide a general evaluation of the application of PSA to the image produced from the particular data set. Reconstructions were therefore produced with the different grades of PSA shown in Table 5.1.

Data sets from two measurements were examined with the criteria listed in Table 5.1; a ^{137}Cs point source, and a distributed ^{22}Na line source. The spatial resolution of each reconstruction was determined in both the xy plane and the z plane, quantifying

Gate Criteria	Lateral PSA	No PSA	T30T90	T50	Orig T30T90
1	Yes	-	-	-	-
2	-	Yes	-	-	-
3	Yes	-	Yes	-	-
4	Yes	-	-	Yes	-
5	Yes	-	-	-	Yes
6	Yes	-	Yes	Yes	-
7	-	-	Yes	-	-
8	-	-	-	Yes	-
9	-	-	-	-	Yes
10	-	-	Yes	Yes	-

Table 5.1: Table documenting the ten gating criteria that were applied to the data to determine the optimum combination of PSA gates which provide the highest resolution image.

the location of the source in three dimensions.

5.4.1 ^{137}Cs Point Source Measurement

Data were collected using the SmartPET Compton camera system and a 0.273 MBq ^{137}Cs point source. The source was mounted at a distance of 72 mm from the AC coupled face of the SmartPET 1 crystal, and was centrally located with respect to the crystal face. The detectors were separated by a distance of 30 mm, which was the closest separation possible due to the detector casing. The average trigger rate throughout the measurement was approximately 170 counts/second. The data acquired totalled 55 GB and was collected over a 12 hour period. A photograph of the source mounted in front of the two SmartPET detectors in a Compton camera configuration is shown in Figure 5.4.

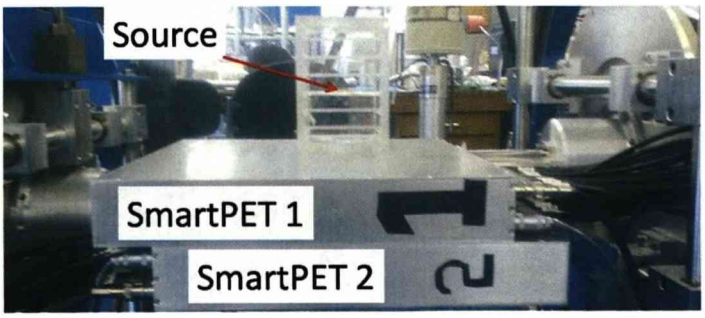

Figure 5.4: Photograph of the Compton camera apparatus with a point source mounted in the plastic stand above SmartPET 1.

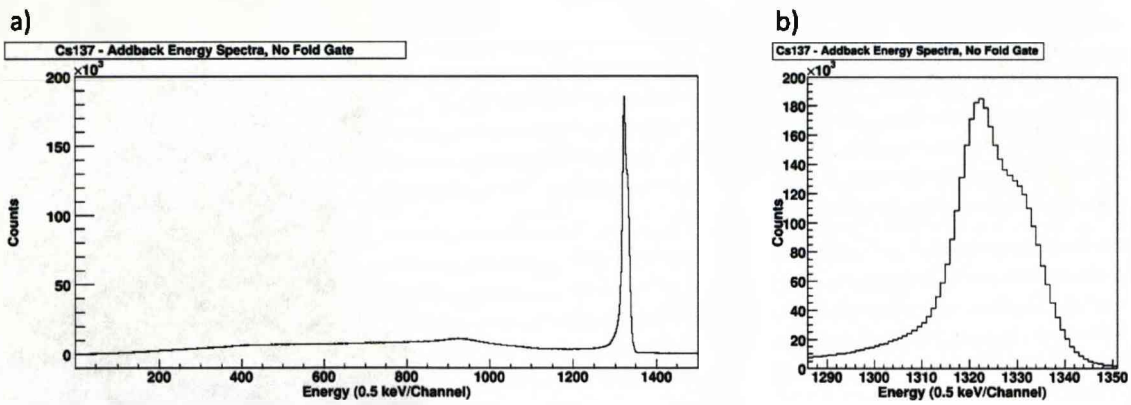

Figure 5.5: Addback spectrum from the two SmartPET detectors of the ^{137}Cs point source. Part a) shows the addback spectrum obtained by summing the energies recorded from each detector. Part b) shows a magnified view of the photopeak. A high energy shoulder is present on the photopeak which is possibly the result of cross talk between strips for multiple interactions. The FWHM of the photopeak is 8.5 keV.

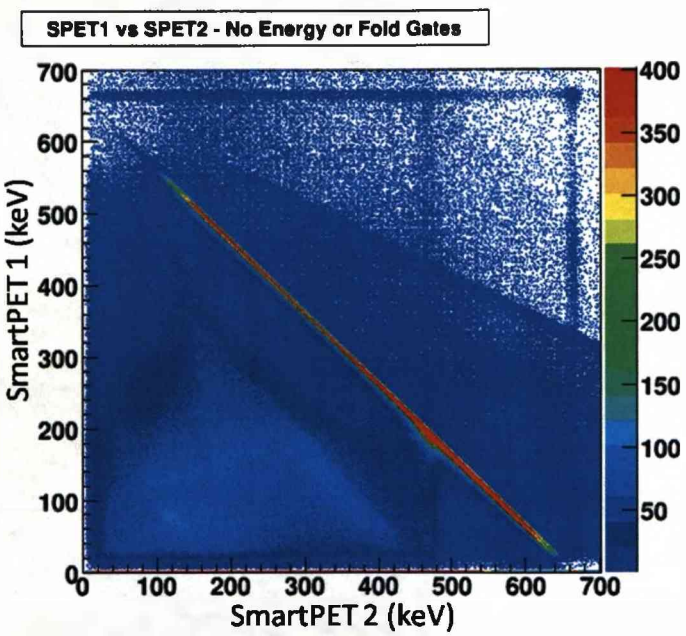

Figure 5.6: Plot of the energies from SmartPET 1 plotted against the energies in SmartPET 2, where events sharing their full energy between the two detectors fall along the diagonal line between 662 keV.

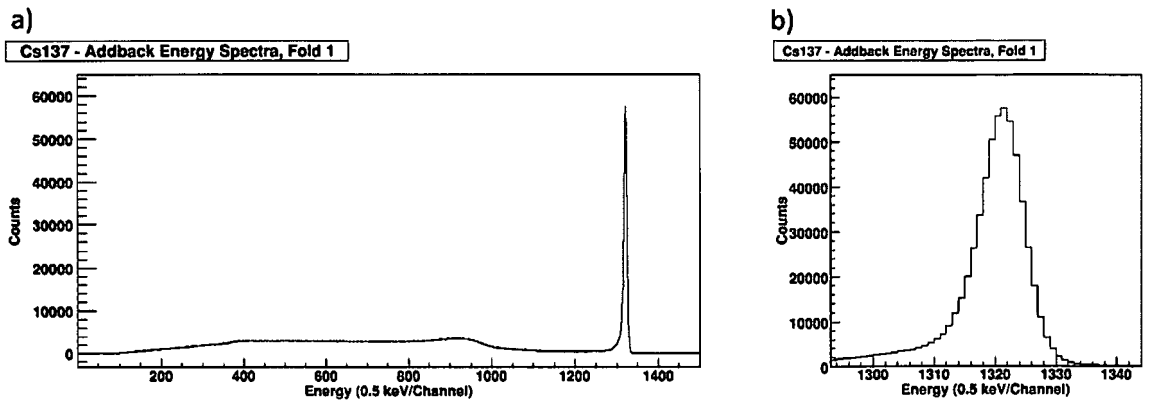

Figure 5.7: Addback spectrum from the two SmartPET detectors of the ^{137}Cs point source with a fold 1 criteria applied. Part a) shows the addback spectrum after a fold 1 condition is applied to both detectors. Part b) zooms in on the photopeak showing which is exhibiting a much more typical Gaussian distribution expected from a photopeak than observed in Figure 5.5 part b). The FWHM of the photopeak is 4.5 keV.

There were approximately 12 million events in the addback spectra with no fold gate, of which 3 million were in the photopeak. Figure 5.5 part a) shows the addback spectrum obtained by summing the energies recorded from each detector. Figure 5.5 part b) shows a magnified view of the photopeak. A high energy shoulder was present on the photopeak which was possibly the result of multiple interactions resulting in cross talk effects between strips. The cross talk results from undesired coupling between the detector electrodes. When the energies from an event triggering more than one strip on a detector face are summed together, the resulting energy can be increased by up to 6 keV which could form the high energy shoulder to the photopeak. Observations from cross talk effects are documented in [Tur06]. Figure 5.6 shows the energies from SmartPET 1 plotted against the energies in SmartPET 2, where events sharing their full energy between the two detectors fall along the diagonal line between 662 keV.

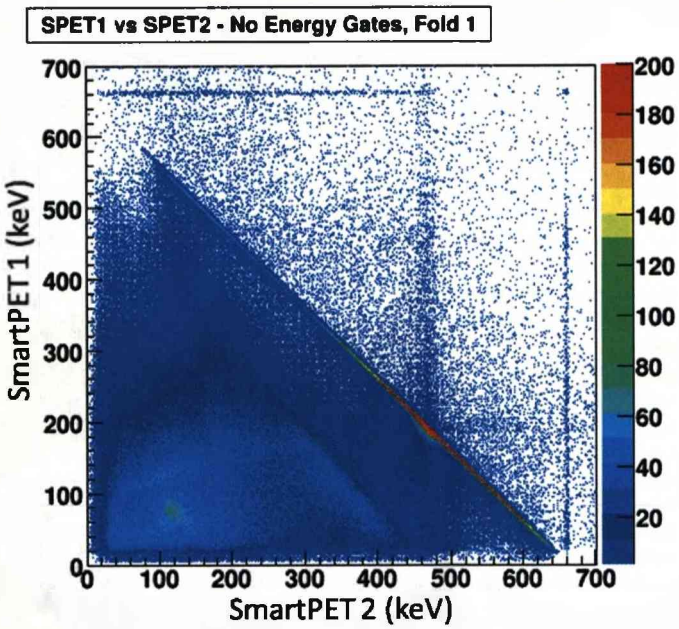

Figure 5.8: Plot of the energies from SmartPET 1 plotted against the energies in SmartPET 2, where events sharing their full energy between the two detectors fall along the diagonal line between 662 keV.

The reconstruction code requires that the events to be reconstructed satisfy a fold 1 condition in both detectors and that the sum of these two interactions must be equivalent to the incident photon energy (662 keV). To ensure only these events are used in the reconstruction, the sum energy of the two interactions uses energy gates set at 655 keV and 670 keV. These requirements are placed on the data to select the events likely to consist of a single scatter and an absorption. When a fold 1 requirement is imposed on the data, the total number of events was roughly 3 million, with over 0.5 million of those events occurring in the photopeak. Figure 5.7, part a) shows the addback spectrum after a fold 1 condition is applied to both detectors. Figure 5.7 b) zooms in on the photopeak which exhibited a much more typical gaussian distribution expected from a photopeak. This suggested that the high energy shoulder observed in Figure 5.5 b) is likely to be due to multiple depositions occurring from events higher than fold 1, which can produce a higher summed energy due to cross talk effects between electrodes. Figure 5.8 shows the energies from SmartPET 1 plotted against the energies in SmartPET 2, where the potentially usable events (full energy shared between the detectors via a fold 1 interaction in each detector), fall along the diagonal line between 662 keV. In contrast to Figure 5.6, not many events occur above 300 keV in SmartPET 1. A deposition of 300 keV approximately corresponds to a scatter of 69^0, suggesting that scatters above this energy are less likely to be incident on the absorber detector (SmartPET 2) which is situated directly behind SmartPET 1.

For each reconstruction, the first 30,000 events were used. The same exact events were used in each reconstruction. Although approximately 100,000 events were collected, the reconstructions were limited to 30,000 of events to ensure that each reconstruction was completed in under 24 hours, due to the computationally intensive nature of the reconstruction code.

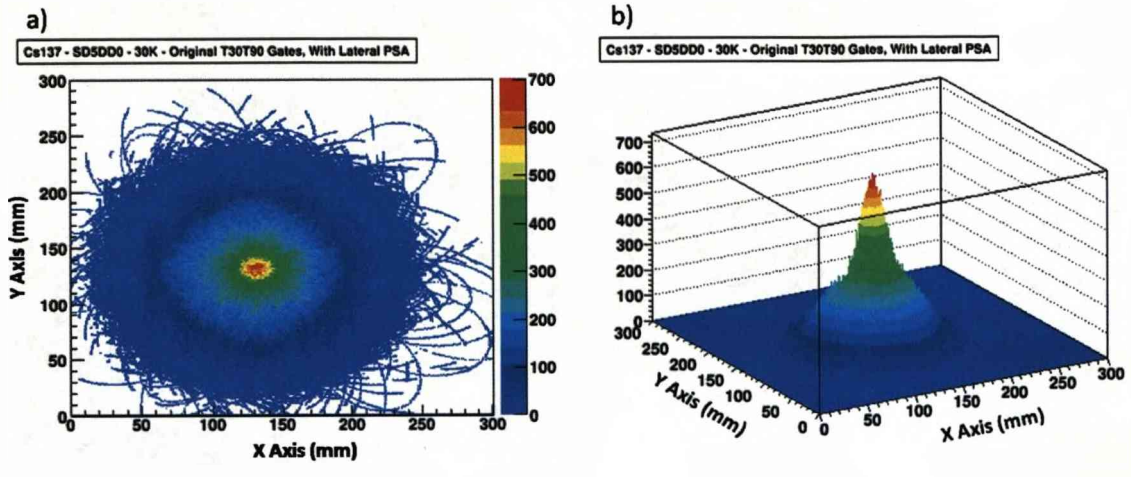

Figure 5.9: Reconstruction of the ^{137}Cs point source using the original T30T90 gates. Source is at a distance of 72mm from the AC face of SmartPET 1. a) 2D profile of the xy plane corresponding to the source position. b) 3D profile of the xy source plane.

5.4.2 ^{137}Cs Point Source Reconstruction

Figure 5.9 shows the reconstruction of the source in the xy plane using the original T30T90 gates (4 mm depth sensitivity) and with lateral PSA applied. a) shows the reconstruction as 2D colour intensity map. b) shows the reconstruction as a 3D surface plot. For the xy plane, the resolution is quoted in terms of FWHM (Full Width at Half Maximum) and FWTM (Full Width at Tenth Maximum) in units of millimeters. They were calculated along both the x and y axis through the centre of the reconstruction, shown in Figure 5.10. The resolutions in the xy plane for all the reconstructions created using the different PSA gates are presented in Figure 5.11. The plot at the top of Figure 5.11 shows the FWHM values and to the bottom, the FWTM values.

It can be seen from the resolution results in Figure 5.11 that the optimum PSA to apply are the T30T90 gates with no lateral PSA. These achieved a FWHM of 18 and 19 mm and a FWTM of 131 and 130 mm in the x and y planes respectively. Figure 5.12 shows the resolution values in both x and y planes averaged to give a single figure

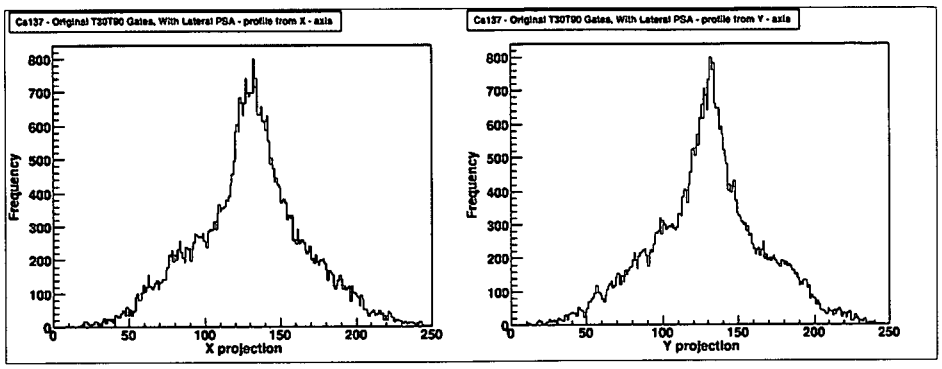

Figure 5.10: Plots show the distribution of intensity in the xy source plane. The spatial resolution is calculated in terms of FWHM (Full Width at Half Maximum) and FWTM (Full Width at Tenth Maximum) in units of millimeters using these distributions.

for the position resolution obtained with each application of PSA. These values are quoted with a 1.4 mm error margin. This value for error is calculated by estimating a 1 mm error to each side of the distribution and summing these errors in quadrature. When the values are averaged, the T30T90 gates with no lateral PSA resolution was 18.5 mm at FWHM and 130.5 mm at FWTM.

Table 7.3 lists the position resolutions obtained from the reconstructions. It can be seen from both Table 7.3 and Figures 5.11 and 5.12 that when lateral PSA is applied to the data, the position resolution degrades. This is an unexpected result which suggests that the asymmetry distribution used to determine where the interaction occurs across the strip needs to be recalibrated, as improving the lateral position sensitivity should improve the position resolution of the image, as discussed early in Chapter Four.

The z position of the source location was calculated by determining a distribution along the z axis by calculating the ratio of the highest number of counts in one element of a plane to the sum of the total counts in that same plane, for each of the two hundred planes. An example of the distribution which localises the source in the z plane is shown in Figure 5.13. These distributions result from using the

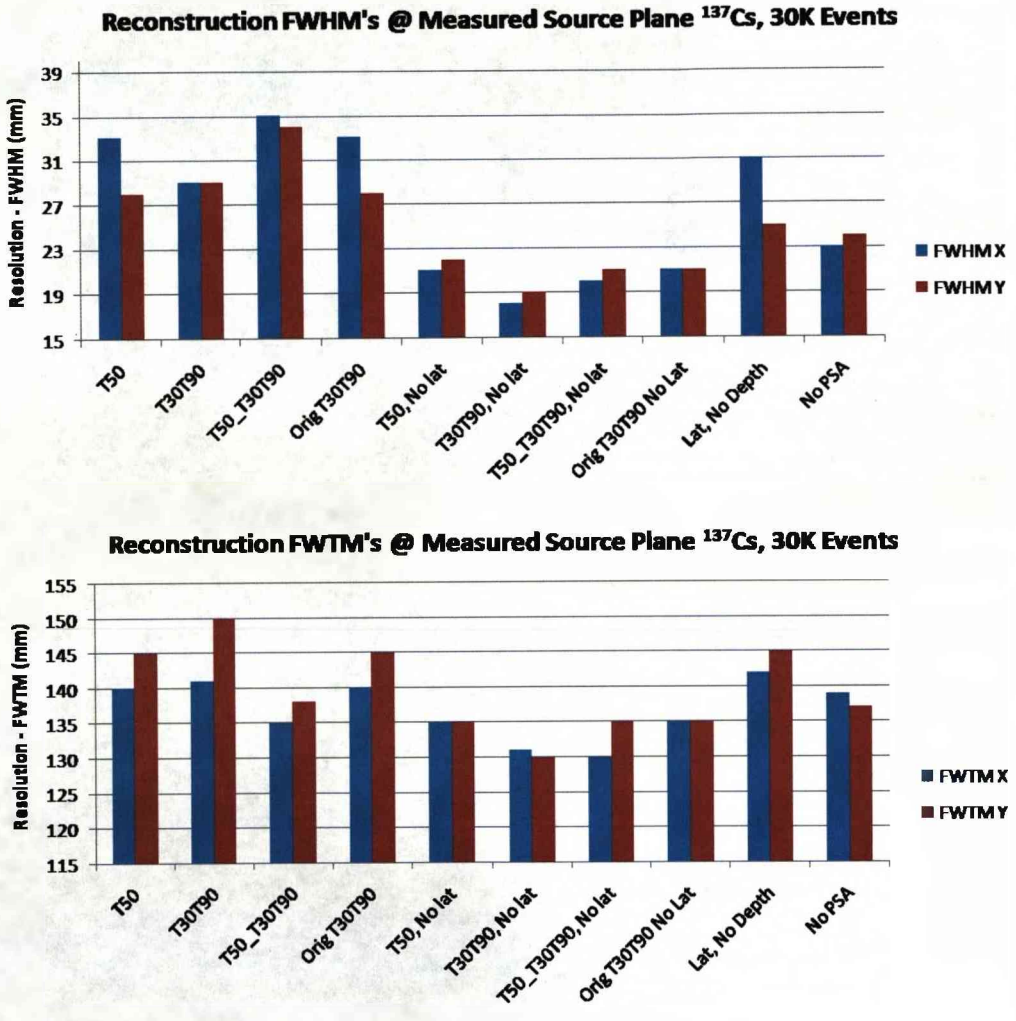

Figure 5.11: Position resolutions of reconstructions in the xy plane.

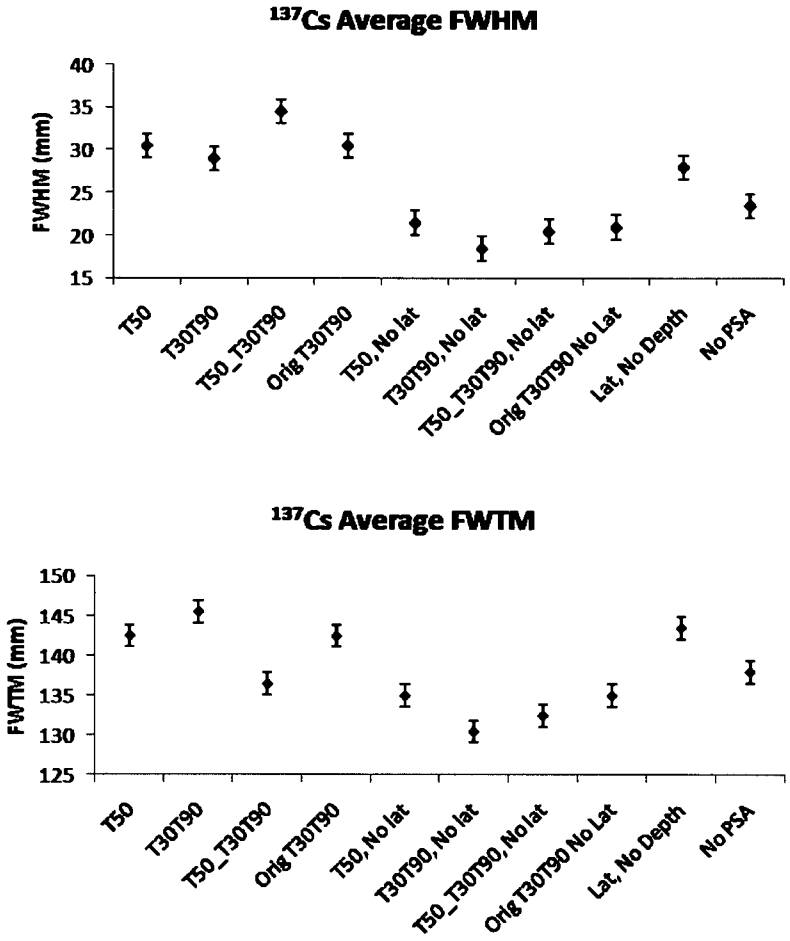

Figure 5.12: Position resolutions from the x plane averaged with those from the y plane. A 1.4 mm error for each value has been assumed by summing a proposed millimeter error from each side of the distribution in quadrature, and is plotted for each point.

PSA Gates	FWHM X	FWHM Y	FWTM X	FWTM Y	Average FWHM	Average FWTM
T30T90 No Lat	18	19	131	130	18.5	130.5
T30T90T50 No Lat	20	21	130	135	20.5	132.5
Orig T30T90 No Lat	21	21	135	135	21	135
T50 No Lat	21	22	135	135	21.5	135
No PSA	23	24	139	137	23.5	138
Lateral No Depth	31	25	142	145	28	143.5
T30T90 With Lat	29	29	141	150	29	145.5
Orig T30T90 With Lat	33	28	140	145	30.5	142.5
T50 With Lat	33	28	140	145	30.5	142.5
T30T90T50 With Lat	35	34	135	138	34.5	136.5

Table 5.2: Table of resolutions measured from the reconstruction of a ^{137}Cs point source positioned at 72 mm from the scatter detector with a detector separation of 30 mm. The gates used have been listed in order of best average FWHM from top to bottom. Units are millimeters.

original T30T90 gates (4 mm depth sensitivity), both with lateral PSA (part a) and without lateral PSA (part b). The distributions derived from the reconstructions using no lateral PSA were all similar in shape to b), and those with lateral PSA were all

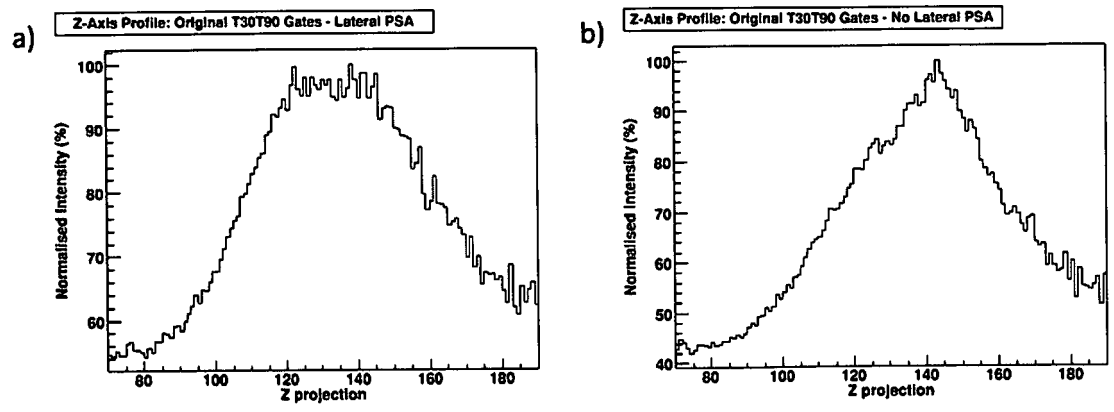

Figure 5.13: Distribution which localises the source in the z plane. Part a) shows the distribution obtained when lateral PSA is included, and part b) when lateral PSA is omitted. These were created by calculating the greatest intensity in the smallest area to determine the position of the source in the z plane.

similar to a). As the distributions with lateral PSA (Figure 5.13 a) were broader at the top and without a well defined peak, it was decided to also quote the width at a higher fraction of the maximum to provide more information about how well the source was actually localised. The resolutions are therefore calculated as the conventional FWTM, FWHM as well as FWTQM (Full Width at Three Quarters Maximum). The source was positioned at a distance of 72 mm from the front face of the scatter detector, however the reconstruction algorithm calculates the distance from the back of the absorber detector. As each detector was 20 mm thick, and separated by 30 mm, the z calculated position had an extra 70 mm included, so the source was expected to be located a distance of approximately 142 mm, with respect to the back of SmartPET 2.

Figure 5.14 presents the position resolutions from the z intensity distributions as in Figure 5.13, for each application of PSA. As with the xy localisation, if lateral PSA is applied the resolution achieved was worse than those gates used with no lateral PSA. It can be seen from Figure 5.14 that the optimum PSA to be used is the original

PSA Gates	FWTQM	FWHM	FWTM
Orig, No Lat	17	37	77
T50, No Lat	18	42	83
T30T90T50, No Lat	25	47	92
NoPSA	25	47	93
T30T90, No Lat	26	46	94
Lat, No Depth	22	55	86
T30T90, With Lat	31	50	109
Orig, With Lat	32	55	108
T50, With Lat	32	55	108
T30T90T50, With Lat	35	51	122

Table 5.3: Table of z location resolutions measured from the reconstruction of a ^{137}Cs point source positioned at 72 mm from the scatter detector with a detector separation of 30 mm. The gates used have been listed in order of best average resolution from top to bottom. Units are in millimeters.

T30T90 gates (4 mm depth sensitivity). The position resolutions are also listed in Table 5.3.

From the reconstructions of the ^{137}Cs point source, which was positioned at 72 mm from the scatter detector with a detector separation of 30 mm, the analysis conducted has shown that the source can be localised in three dimensions. The resolution of the reconstruction has been quantified in each dimension to determine which PSA gates provide the most localised image. The best PSA gates differ depending upon which dimension was being localised. In the xy plane it was found the that optimum gates were the T30T90 gates determined in Chapter Four, with no lateral PSA. In the Z dimension it was found that the original T30T90 gates (4 mm depth sensitivity), again with no lateral PSA, provide the best localisation.

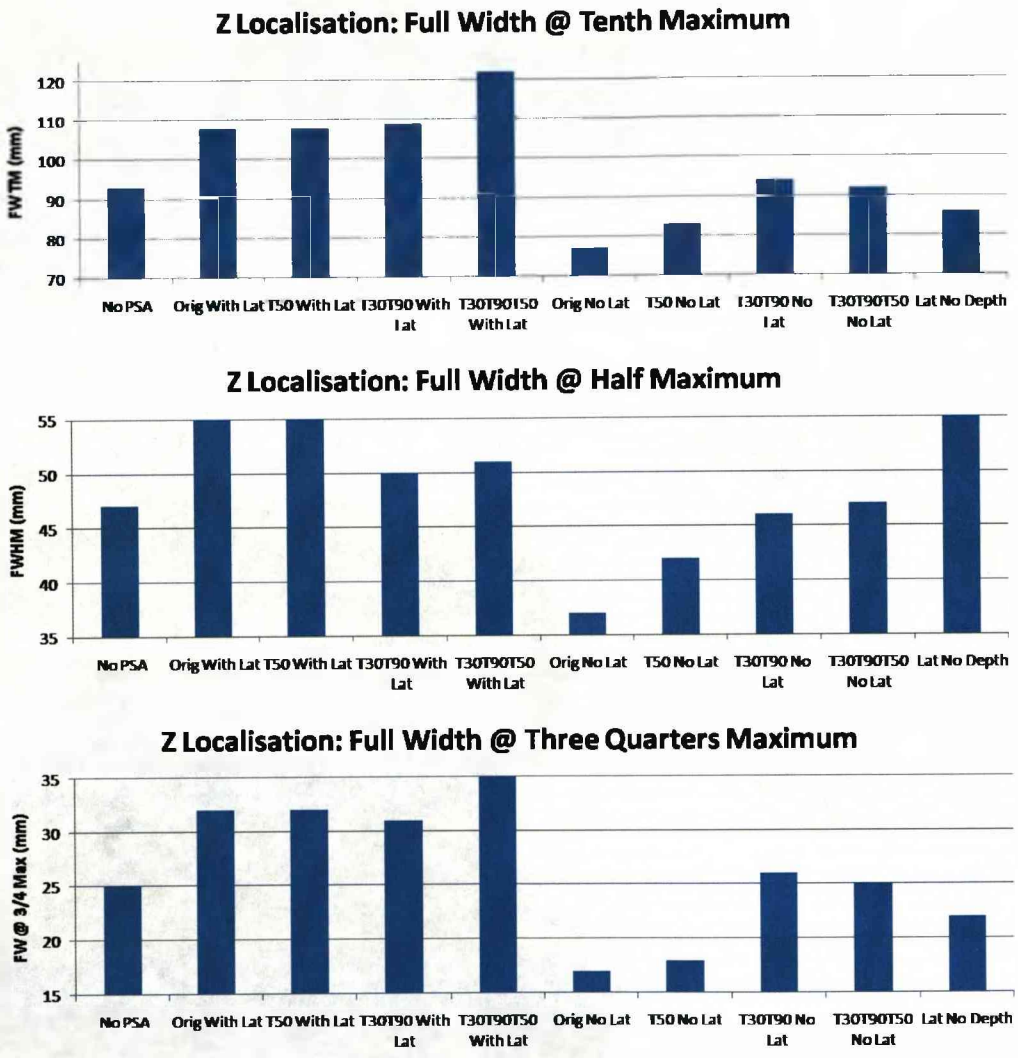

Figure 5.14: Resolutions from the z intensity distributions. The resolutions are calculated as FWTM, FWHM and FWTQM (Full Width at Three Quarters Maximum).

5.4.3 ^{22}Na Line Source Measurement

The second measurement used a distributed 0.9 MBq ^{22}Na line source. The source was 50 mm in length with an internal diameter of 2.5 mm, and was located at a distance of 71 mm from the front (AC) face of SmartPET1. Figure 5.15 is a photograph of the source. The detectors were again separated by a distance of 30 mm. The average trigger rate throughout the measurement was approximately 210 counts/second and the total data acquired was 24 GB, collected over a 8 hour period. Following from the ^{137}Cs point source reconstructions, the ^{22}Na line source was reconstructed using the T30T90 gates (1 mm depth sensitivity) with no lateral PSA and the original T30T90 gates (4 mm sensitivity). A reconstruction using no PSA was also produced. All reconstructions used the same 50,000 events. This increase in the number of events used with respect to the point source was intended to help account for the distributed nature of the source. It would be desirable to compare reconstructions created using the two different energies emitted from ^{22}Na (511 keV and 1274 keV), however this was not feasible due to time constraints and so only reconstructions using the 511 keV line are presented in this work.

Figure 5.16 part a) shows the addback spectrum obtained by summing the energies recorded from each detector. Figure 5.16 part b) shows a magnified view of the photopeak. Of the total 5 million events in the spectrum, 0.45 million events fall within the photopeak boundaries, which were at 500 keV and 520 keV. Figure 5.17 shows the energies from SmartPET 1 plotted against the energies in SmartPET 2, where events sharing their full energy between the two detectors fall along the diagonal line between 511 keV.

Figure 5.19, part a) shows the addback spectrum after a fold 1 condition is applied to both detectors. Figure 5.19 b) zooms in on the photopeak showing which is exhibiting a low energy tail. It is possible that this was the result of scatters from the higher energy 1274 keV γ rays, which could also be responsible for the poor FWHM of 14 keV

Figure 5.15: Photograph of the ^{22}Na line source.

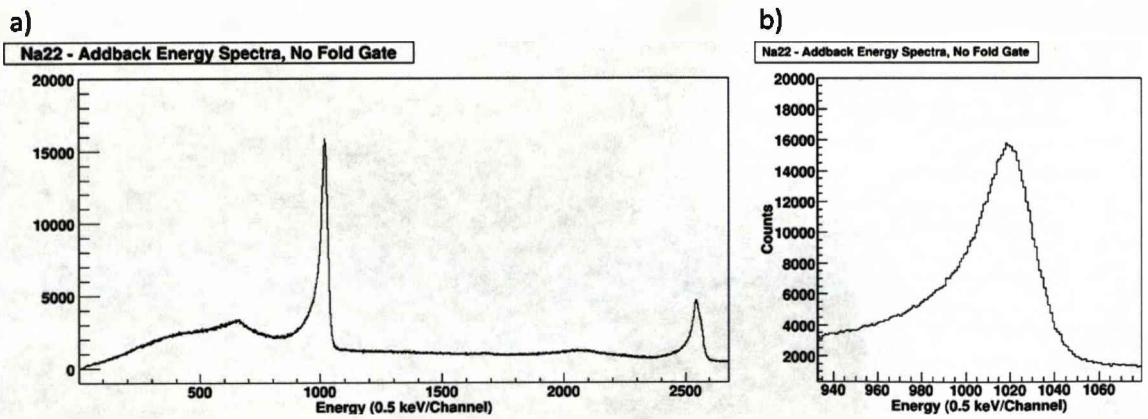

Figure 5.16: Addback spectrum from the ^{22}Na line source Compton measurement. Part a) shows the addback spectrum obtained by summing the energies recorded from each detector. Part b) shows a magnified view of the 511 keV photopeak which has a FWHM of 14.5 keV.

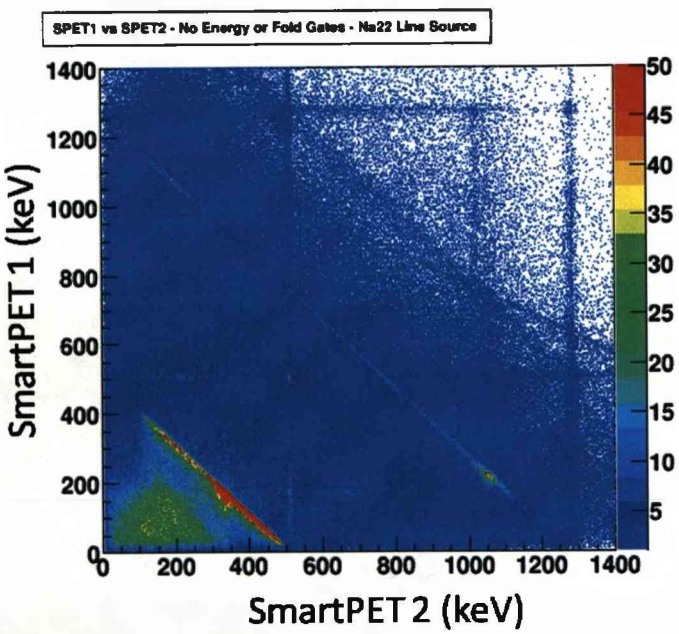

Figure 5.17: Energies from SmartPET 1 plotted against the energies in SmartPET 2, where events sharing their full energy between the two detectors fall along the diagonal line between 511 keV.

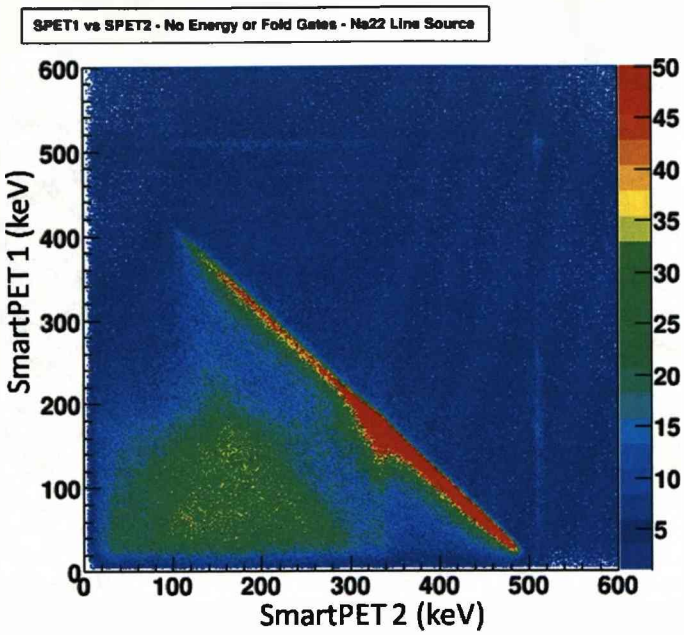

Figure 5.18: Plot of the energies from SmartPET 1 plotted against the energies in SmartPET 2. The plot is a magnified view of Figure 5.17 to show the energy deposition due to the 511 keV photons in more detail.

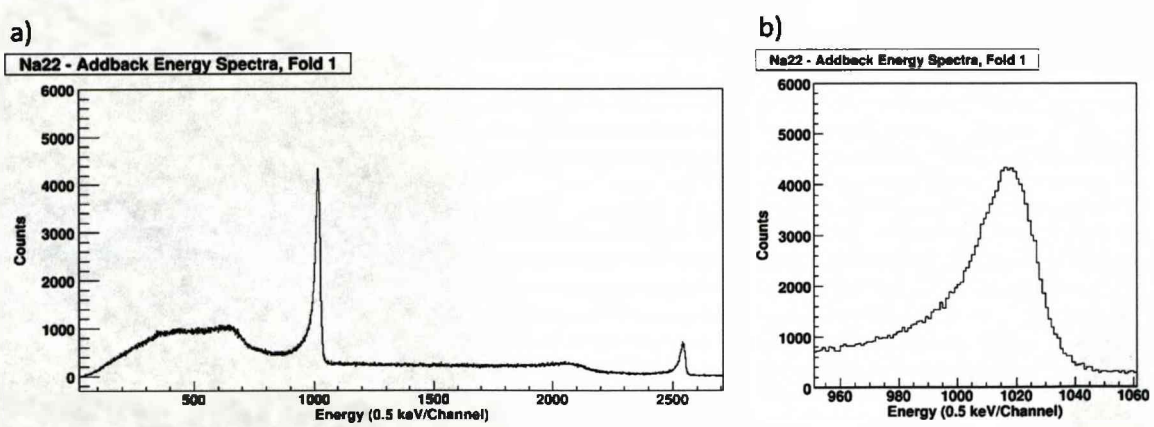

Figure 5.19: Addback spectrum from the ^{22}Na line source Compton measurement with a fold 1 condition applied. Part a) shows the addback spectrum after a fold 1 condition is applied to both detectors. Part b) zooms in on the photopeak with a FWHM of 14 keV.

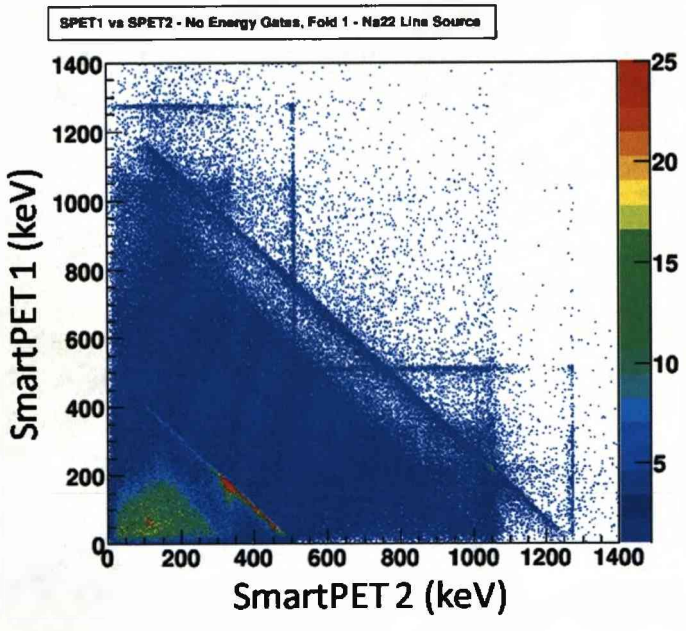

Figure 5.20: Energies from SmartPET 1 plotted against the energies in SmartPET 2, where the potentially usable events (full energy shared between the detectors via a fold 1 interaction in each detector) fall along the diagonal line between 511 keV.

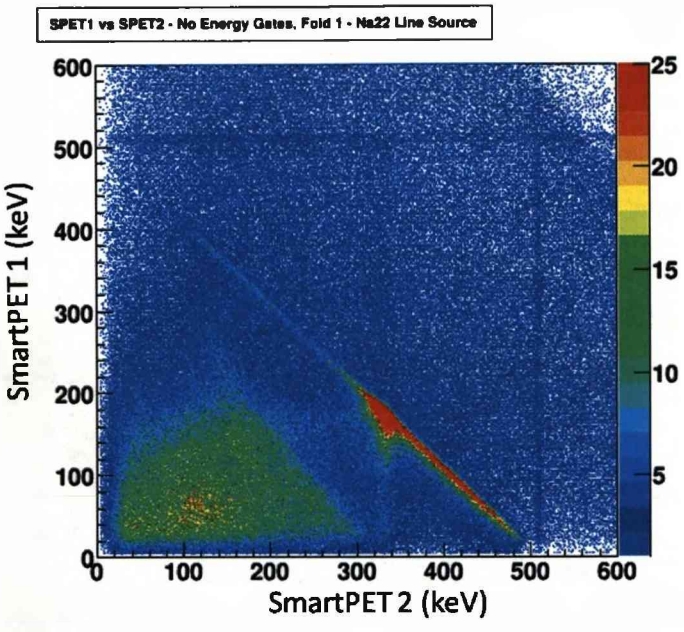

Figure 5.21: Plot of the energies from SmartPET 1 plotted against the energies in SmartPET 2. The plot is a magnified view of the distribution shown in Figure 5.20 to show the energy deposition due to the 511 keV photons in more detail.

recorded. Figure 5.20 shows the energies from SmartPET 1 plotted against the energies in SmartPET 2, where the potentially usable events (full energy shared between the detectors via a fold 1 interaction in each detector), fall along the diagonal line between 511 keV. A magnified view of this distribution for the 511 keV energy depositions is shown in Figure 5.21. An energy cut off point was again observed, this time at approximately 200 keV which corresponds to a 69^0 scatter, mirroring the effect from the ^{137}Cs measurement.

5.4.4 ^{22}Na Line Source Reconstructions

Figure 5.22 shows the 2D (part a) and 3D (part b) reconstructions in the xy plane of the line source. From the 2D image it can be seen that the area of intensity is greater along the x axis with respect to that in the y axis, clearly showing the distributed nature of the line source. Figure 5.23 shows the distribution of intensity through the centre of the reconstruction along both the x and y planes. As with the ^{137}Cs point source reconstructions, the resolutions in the xy plane are presented in terms of FWHM and FWTM along both axis.

Figure 5.24 shows the resolutions obtained from the reconstructions using the three different grades of PSA. Again, the averages of the resolutions have also been calculated and are presented in Figure 5.25 and Table 5.5.

These results show that neither of the optimum PSA grades determined from the previous reconstruction improve upon using no PSA. This is unexpected as the reconstructions from the ^{137}Cs point source implied that the risetime gates used with no lateral PSA provided better localisation than without. Although a greater number of events are used in the reconstruction of the line source (50K compared to 30K for the point source) it may be that many more events are needed to effectively reconstruct a distributed source. The distributions illustrating the localisation in the z plane can be seen in Figure 5.26, however the source does not seem to have been as effectively

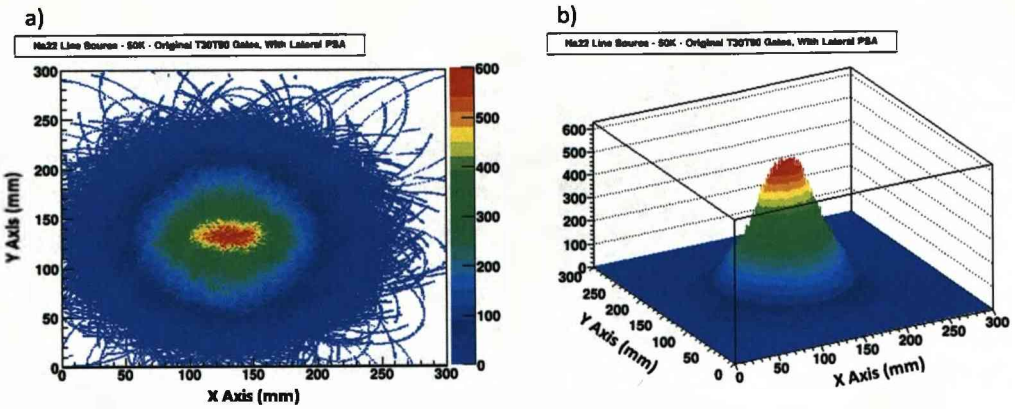

Figure 5.22: Reconstruction of the ^{22}Na line source using the original T30T90 gates with lateral PSA applied. The source is at a distance of 72mm from the AC face of SmartPET 1. a) 2D profile of the xy plane corresponding to the source position. b) 3D profile of the xy source plane.

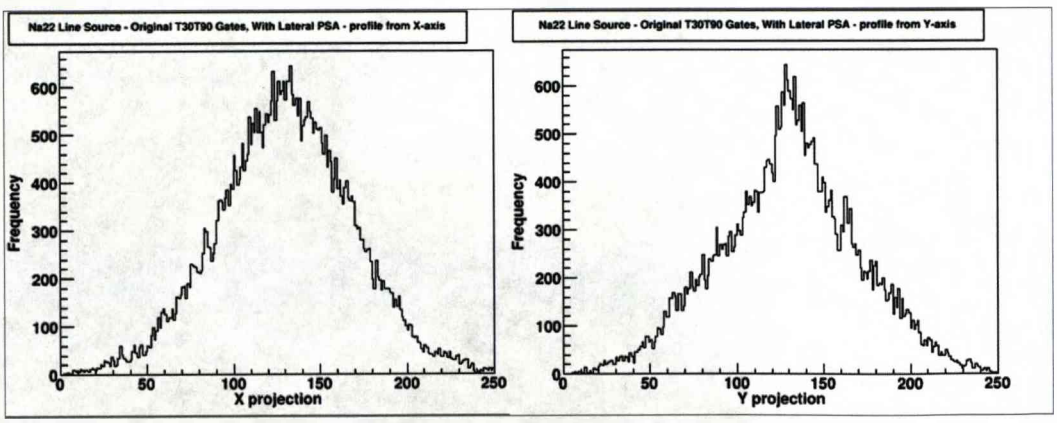

Figure 5.23: Plots show the distribution of intensity in the xy source plane. The spatial resolution is calculated in terms of FWHM (Full Width at Half Maximum) and FWTM (Full Width at Tenth Maximum) in units of millimeters using these distributions.

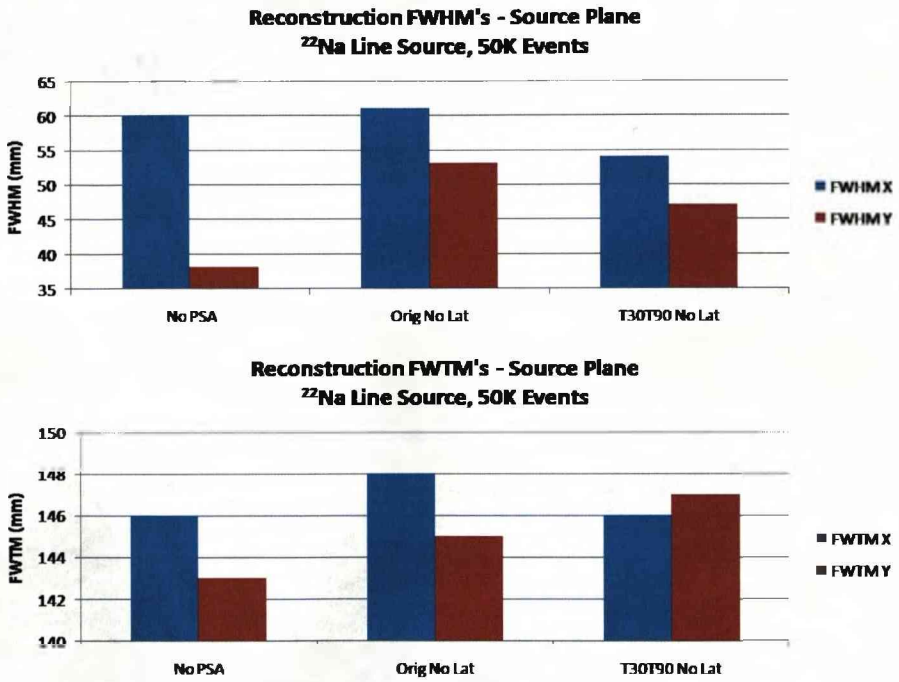

Figure 5.24: Position resolutions calculated from the reconstructions using the three different grades of PSA.

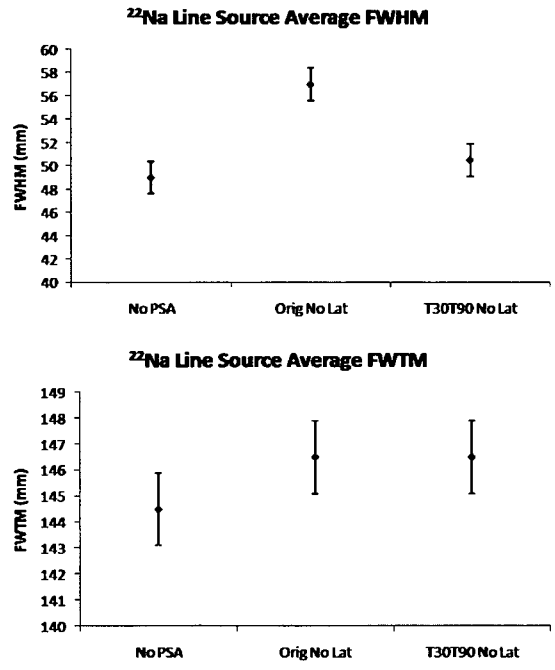

Figure 5.25: Position resolutions from the x plane averaged with those from the y plane. A 1.4 mm error for each value has been estimated and is plotted for each point.

PSA Gates	FWHM X	FWHM Y	FWTM X	FWTM Y	Average FWHM	Average FWTM
NoPSA	60	38	146	143	49	144.5
T30T90, No Lat	65	47	146	147	50.5	146.5
Orig, No Lat	61	53	148	145	57	146.5

Table 5.4: Table resolutions in the xy plane from the reconstruction of a ^{22}Na line source positioned at 72 mm from the scatter detector with a detector separation of 30 mm. The gates used have been listed in order of best average resolution from top to bottom. Units are millimeters.

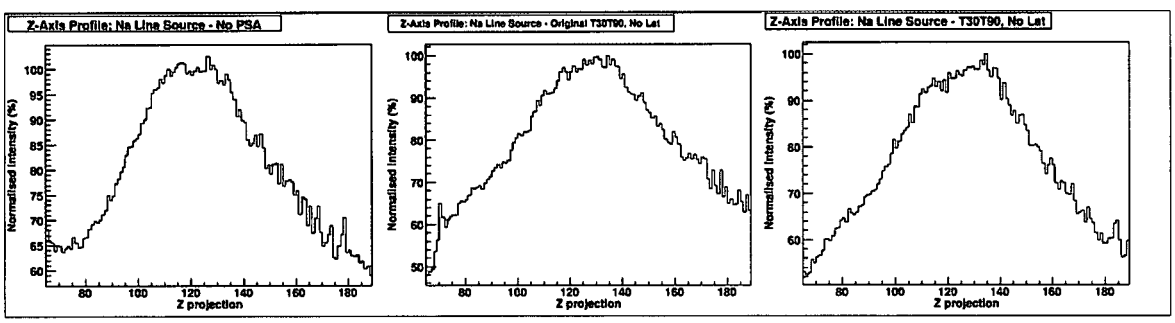

Figure 5.26: Distributions illustrating the localisation in the z plane. These were created by calculating the greatest intensity in the smallest area to determine the position of the source in the z plane.

localised as with the point source. Figure 5.27 shows the resolutions obtained from the z distributions. Again, a third parameter of Full Width at Three Quarters Maximum (FWTQM) has been used to provide more information regarding the localisation of the source through the z plane.

It can be concluded that the application of PSA does not improve the image obtained from the reconstruction in any of the 3 dimensions. It is not clear why this is the case, as the application of PSA to the ^{137}Cs point source data improved the localisation of the source. It may be that a higher number of statistics is required, and

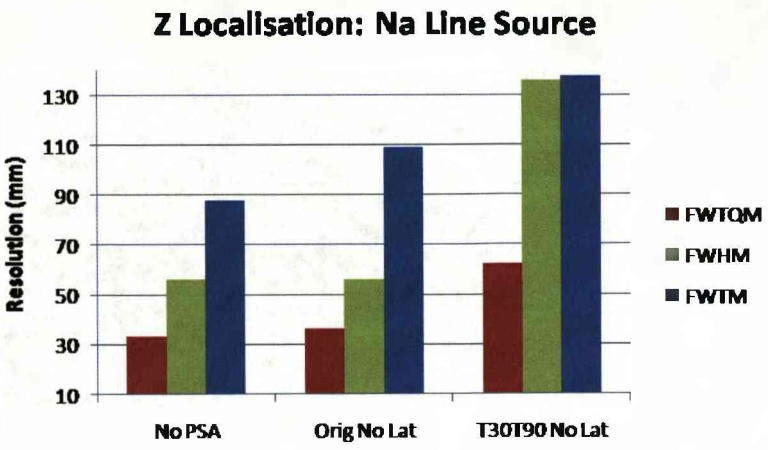

Figure 5.27: Position resolutions obtained from the z distributions shown in Figure 5.26.

PSA Gates	FWTQM	FWHM	FWTM
NoPSA	33	56	88
Orig, No Lat	36	56	109
T30T90, No Lat	62	136	138

Table 5.5: Table of z location resolutions measured from the reconstruction of a ^{22}Na line source positioned at 72 mm from the scatter detector with a detector separation of 30 mm. Units are millimeters.

it would also be of interest to observe the images produced by utilising the 1274 keV γ line. It must also be mentioned that complications in the reconstruction can occur due to the distributed nature of the source. This is manifested in the form of an increased possibility of false intersections, as cones from different regions of the source will form an overlap with each other more often than if they were emitted from a single point. Secondly, the presence of a higher energy line also has the potential to complicate the reconstruction, as scatters from these photons could feasibly be present in the 511 keV addback peak and be incorrectly identified as a 511 keV photon. This will lead to false cones being created during the reconstruction which will result in image degradation.

Chapter 6

Double Sided Silicon Strip Detector (DSSSD)

One of the goals of the Compton camera project is to demonstrate imaging at a similar gamma photon energy to that currently utilized in medicine, namely metastable Technetium 99 (^{99m}Tc), which emits photons with an energy of 141 keV. As mentioned in the introduction, it has already been observed from experimental measurements [Gil06], [Bos06], that the lowest energy the SmartPET Compton camera system can image is of the order of 300 keV. This is due to the 20 mm thickness of the scattering detector (SmartPET 1) significantly attenuating energies below this value. This prohibits scatters through to the absorber detector which is the necessary sequence of interactions required to take place if a reconstruction cone is to be created and an image subsequently obtained.

This chapter presents the steps taken to try and overcome this problem by the introduction of a double sided silicon strip detector (DSSSD) as a substitute scatter detector. The use of a silicon detector has potential advantages over germanium including an increased Compton scatter cross section for lower energies and lower uncertainty in the determination of the scatter angle, due to a reduced contribution from Doppler broadening [Zog03], which is the dominant factor in angular resolution

for energies around a few hundred keV.

Prior to using a detector in a measurement such as a Compton camera experiment, details must be known about the detector characteristics, primarily its uniformity of pulseshape response to γ ray photons. In order to achieve this the detector response as a function of position has been measured. This allowed an investigation into the possible application of PSA to refine the position of interaction beyond that of the detector segmentation, as applied in SmartPET. The apparatus and methods for the characterisation are outlined in this chapter including the detector details, scanning setup, digital acquisition system, measurements taken and subsequent signal analysis.

6.1 Experimental Details

6.1.1 Silicon Detector Description

The detector used was a double sided silicon strip detector (Figure 6.1), manufactured by Micron Semiconductor UK [Mic09] and on loan from the University of Edinburgh [Dav07]. The detector had a silicon n-type crystal of $53.78 \times 53.78 \times 0.5$ mm^3 with an active volume of $50 \times 50 \times 0.5\,mm^3$. The crystal was electrically segmented into 2 sets of 16 orthogonal strips. The strips on each side have a pitch of 3.1 mm and an inter strip gap of 100 μmm on both faces of the detector. The detector was DC coupled and the depletion voltage of the crystal was -30 V, with the operational voltage at -80 V. The contacts on the AC-side are labeled AC01 - AC16 and on the DC-side DC17 - DC32. Every contact is connected to a Rutherford Appleton Laboratory (RAL) [Tho90] charge sensitive preamplifier with a gain of 20 mV/MeV, which were also on loan from the University of Edinburgh.

Figure 6.1: Photograph of the Double Sided Silicon Strip Detector manufactured by Micron Semiconductor UK [Mic09].

6.1.2 Data Acquisition System

The requirement to analyse the shape of the pulses produced by the charge sensitive preamplifiers requires the use of a digital electronic system. The DAQ system is based on 8 VME GRT4 modules manufactured by Daresbury Laboratory [Laz01] and was discussed in Chapter Four.

6.1.3 Trigger

The GRT4 cards are triggered externally using conventional analogue timing electronics. The least noisy signals observed from the DC channels proved a more reliable trigger source than those from the AC channels. The preamplifier signals observed were very noisy (80 mV peak to peak) and the observation of a preamplifier pulse in this noise was extremely difficult. Quad TFAs (Ortec 863 units) were used to amplify the signal and try to reduce some of the noise. The TFAs were set with the differentiation function to 0.1 μs (reducing low frequency noise), and the integration function to 50 ns (to reduce the high frequency noise). This resulted in pulses of about 100 mV from 60 keV photons with a peak to peak noise on the baseline of 50 mV.

The trigger was achieved by using a T junction to split each of the sixteen signals passed though from the DC side. One of the split signals from each of the T pieces was then passed through another set of timing filter amplifiers (Ortec units 474 and quad 863 set with 50 ns differentiation and 200ns integration) for the timing/trigger signal, and the other signal from each channel to the GRT4 cards for processing. The trigger signals were subsequently passed through constant fraction discriminators (Ortec models 473 and 934) with a time delay of 10 ns, into a logical OR unit and then to a gate and delay generator. A circuit diagram of the system set up is illustrated in Figure 6.2. The trigger signal was then input to the eight GRT4 cards to signal the cards to read the data from the thirty-two detector channels. Whilst the GRT cards are processing data an inhibit signal is sent to the gate and delay unit to prevent any further trigger signals being sent until all signals being processed by the cards have been passed on to storage. The trigger level (CFD threshold), was set between the noise level which was approximately 40 keV and 60 keV, using the 60 keV γ-rays from a ^{241}Am source.

6.1.4 Scanning Setup

The position sensitivity obtained from the detector segmentation and thickness is $3.1 \times 3.1 \times 0.5\,\text{mm}^3$. By performing a finely collimated scan, the uniformity of the detector pulseshape response across its face could be deduced, together with an investigation into whether transient charges can be observed on adjacent strips. If transient charges could be observed on neighbouring strips they could be used to refine the position of interaction in the lateral plane beyond that of the strip width. This procedure was successfully applied to the SmartPET detector [Tur06] to localise the position of interaction from the strip width (5 mm) down to 1 mm, as discussed in Chapter Three. It was unlikely that transient pulses would be seen due to the high level of noise present in this detector.

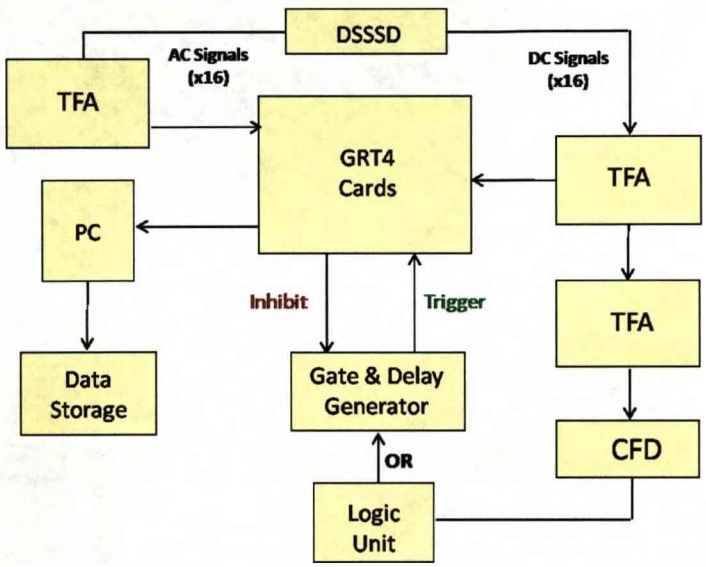

Figure 6.2: A diagram of the data acquisition system used for the silicon scan. The first bank of TFAs for both the AC and DC signals have the differentiation set to 0.1 μs (out) and integration set to 50 ns in order to reduce the baseline noise and amplify the preamplifier pulse. The DC signals are used for the trigger and are subject to a further bank of TFA processing (differentiation of 50 ns, integration of 200 ns) prior to the CFD (delay = 10 ns) units. A logic unit is then used to apply a logical OR condition to the signals from each of the DC channels. Finally a gate and delay generator is used to pass the logic trigger signal to the GRT4 cards when no inhibit signal is received from the cards.

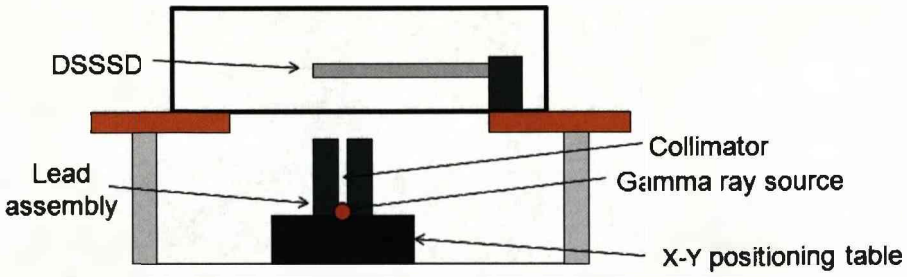

Figure 6.3: The scanning setup with the detector positioned for the ^{241}Am face scan inside a light tight, EM (Electromagnetic) and RF (Radio Frequency) shielded box.

A diagram representing the scanning apparatus used to perform the scan is shown in Figure 6.3 and photographs of the setup can be seen in Figure 6.4. The radioactive source was placed below the 1 mm diameter, 80 mm long collimator in the middle of a lead assembly. The lead, source and collimator were sat on top of an x-y positioning table which was driven by two stepper motors which position the table with a precision of 30 μm. The detector face was 5.9 cm from the top of the collimator, which gave rise to a beam divergence at the surface of the detector of approximately 1.6 mm FWHM. It was not possible to reduce separation between the collimator and the detector due to the proximity of the surrounding supports. The response of the detector was investigated using 60 keV γ-rays from a 1.6 GBq ^{241}Am source. The collimator was moved over the entire face of the detector in 1 mm steps. The scan was done over an area 55 $\times$ 55 mm^2 with the collimator at each position for 120 seconds collecting a total data set of 622 GB.

6.2 Results and Analysis

6.2.1 Intensity of Counts

Figure 6.5 shows a plot of the interaction (full energy, fold 1) intensity as a function of scan position. The dip in intensity through the centre of the detector corresponds

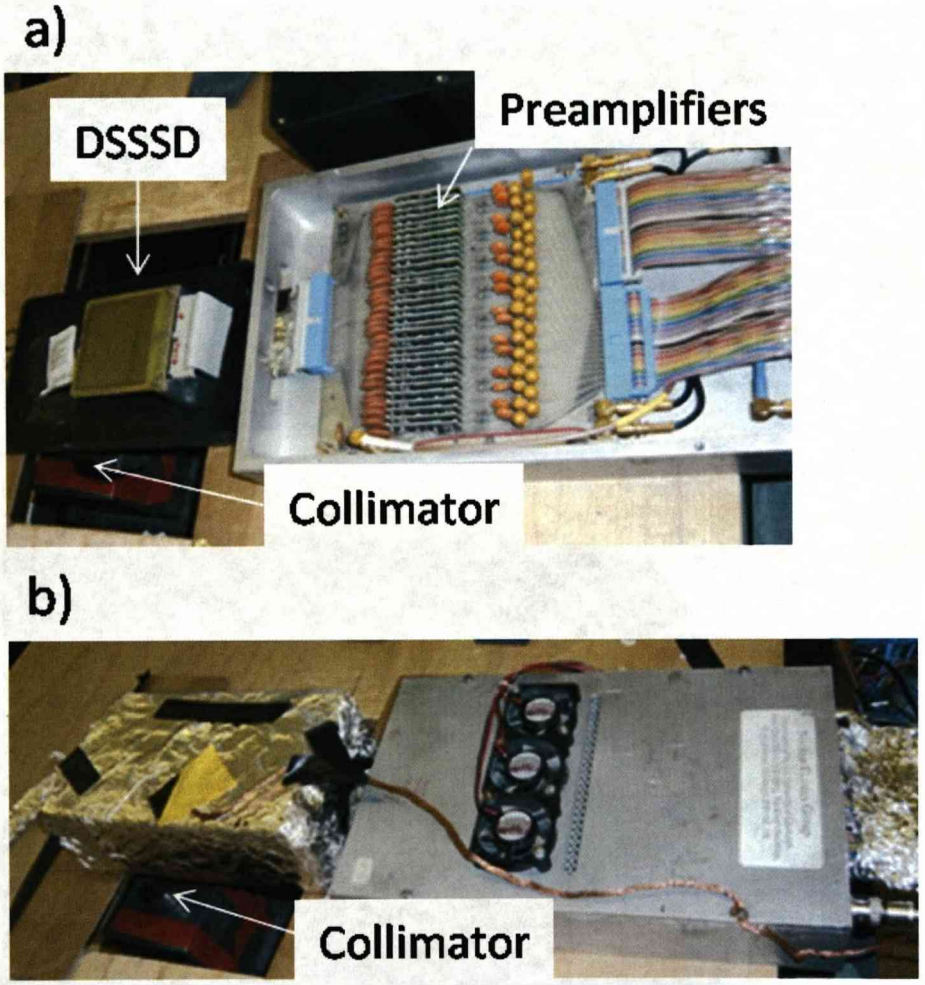

Figure 6.4: Photographs of the silicon scan apparatus. a) DSSSD mounted above the collimator prior to being enclosed in the light tight box together with the exposed preamplifiers. b) System enclosed ready for acquisition. The light tight box housing the DSSSD is surrounded by aluminum foil to increase shielding.

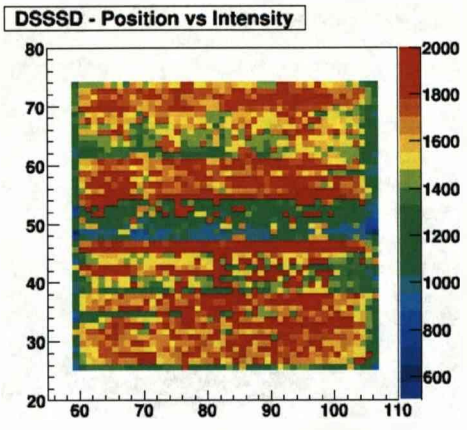

Figure 6.5: Position vs Intensity map for energy gated (60 keV) fold one events.

to strip 25, which was not instrumented due to excessive noise present in that strip (no photopeak could be observed). It can also be seen that there are many areas of differing intensity, generally ranging from 1200 counts to 2000 counts. It is not clear why there is this difference in detected photopeak events, although it must be noted that the system was very susceptible to noise which could have affected the number of accepted triggers (i.e. the areas of high counts correspond to a period where noise was sporadically triggering the system).

6.2.2 Energy and Resolution

Using the data recorded from the scan, Figure 6.6 was created to show the energy resolution (FWHM at 60 keV) and number of counts observed on each strip. It can be seen that the energy resolution for the DC channels is superior to that of the AC channels, with the exception of channel 24 and channel 25. As previously mentioned, channel 25 was not instrumented due to excessive noise, however the cause of noise observed on channel 25 could also be the reason for channel 24 showing poor performance (e.g. a faulty preamplifier or a strip contact fault).

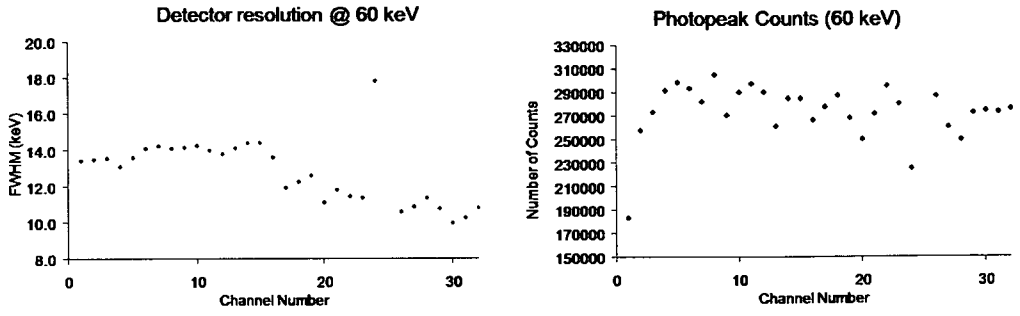

Figure 6.6: Left: Energy resolution (FWHM) for each strip at 60 keV. Right: Number of photopeak events recorded on each strip. AC strips: 1 - 16, DC strips: 17 - 32

6.2.3 Noise Considerations

During the initial detector tests it was noticed that the noise present in the system is not constant, and appeared to fluctuate randomly. It was confirmed that there was sufficient grounding of the system. A separate similar DSSSD was also tested, both with RAL preamplifiers [Tho90] and Amptek A250 preamplifiers [Amp08], and also with and without moderate cooling (down to -10^0 C), however significant noise was observed in all scenarios, contributing between 30 to 40 keV to an energy spectrum. It is likely that the system shielding was not adequate. Steps were taken to improve this by surrounding the detector mount, preamps and signal cables with aluminium foil, which reduced the noise slightly, although it is recommended that a Faraday cage would be required for similar measurements in the future.

6.2.4 Pulse Shape Analysis

As has been mentioned, a significant amount of noise was present in the detector system. The method by which the interaction position is refined beyond that of the segmentation requires the measurement and comparison of transient charges recorded in the strips adjacent to the interaction strip. Figure 6.7 shows the signals recorded from three DC strips during a full energy, fold 1 interaction. The centre strip contains the real charge, and the strips either side should be expected to contain the image

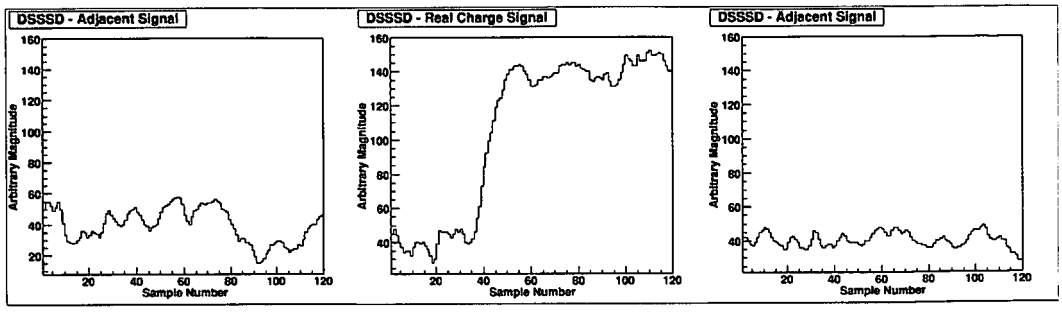

Figure 6.7: Pulses recorded from three neighbouring strips after an interaction in the DSSSD. The real charge is recorded from the hit strip (centre strip) in which the charge from the interaction was collected and is represented by the centre plot. The image charges are induced charges, originating from the movement of charge from the interaction site to the collecting electrode, and are expected in the strips adjacent to the hit strip. The magnitude of noise along the baseline has prohibited the observation of any transient charges that may be present.

charge.

As can be seen, no image charges can be observed above the noise present on the baseline in either of the neighbouring strips. This scenario was observed in all events recorded, resulting in the conclusion that no pulseshape analysis could be performed to improve the lateral position of interaction. The 0.5 mm detector depth also makes the need for any depth analysis as performed for the SmartPET detector in Chapter Four redundant. Risetimes were still employed however, as a method of investigating uniformity of the pulseshape response across the detector, which is expected to be uniform due to the very small depth. Average pulseshapes from different scan positions were used to comment on the uniformity of the detector response across each strip, and strip to strip. When creating the average pulseshape from a particular position, it is desirable to remove pulses uncharacteristic of the majority of pulseshapes from that position. As the detector was susceptible to random noise fluctuations, and without the physical means to further reduce the noise in the system, it was deemed necessary

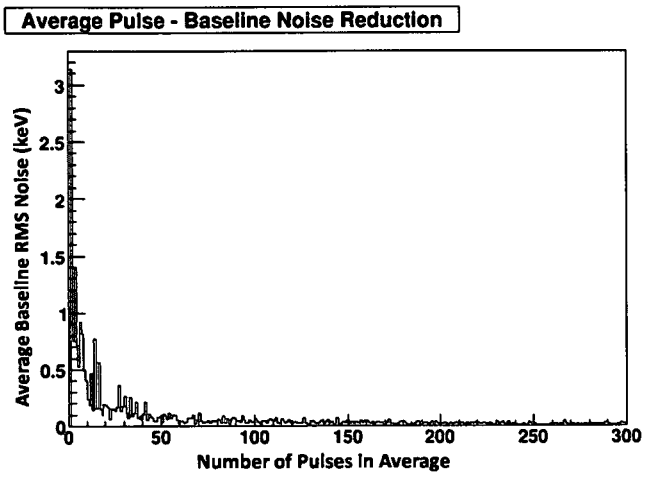

Figure 6.8: Plot showing how the average RMS noise present in the baseline decreases as the number of pulses used to create the average increases.

to attempt to remove those signals exhibiting higher noise in order to allow cleaner signals to be used to characterise the pulseshape response of the detector. Similarly, those pulseshapes which displayed a shape dissimilar to the majority of pulseshapes were also removed from the final set of pulses used to create the average pulseshape to represent that area. Figure 6.8 shows how the noise present in an average pulses was reduced as the number of pulses used increases. It can be seen that above 100 pulses the noise does not appreciably diminish, and so 100 pulses were used (post filtering) to construct the average pulse for a position.

6.2.5 Noise Filtering

Figure 6.9 shows a selection of DC pulses from a scan position intersected by the strips DC30 and AC13, which are from opposing faces. The pulses have been time aligned at 20 percent of their total magnitude. Aligning at a value lower than this caused misalignment due to some pulses triggering in the noise.

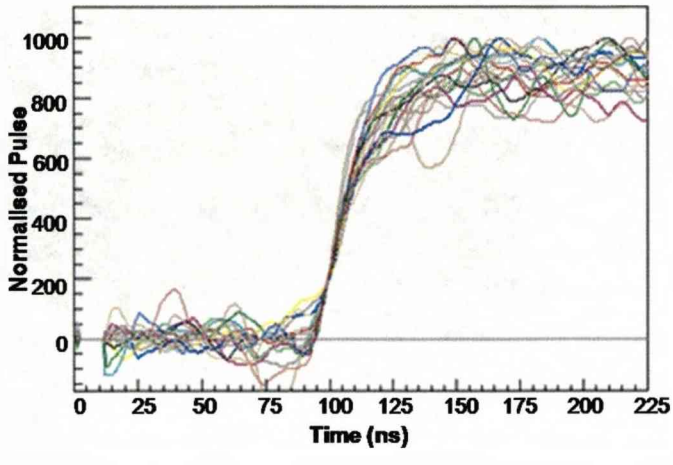

Figure 6.9: Random selection of 20 unfiltered pulses from 60 keV photons. The pulses have been time aligned at 20 percent of their final magnitude and each pulse has been rescaled to 1000.

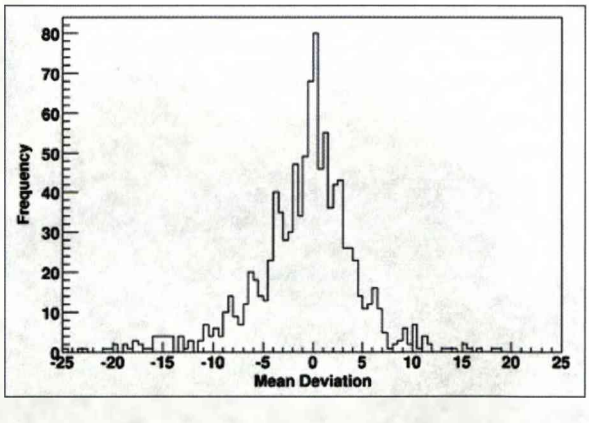

Figure 6.10: Average deviation of the pulses from a set of samples along the baseline. A set of 1000 pulses was used from the same position.

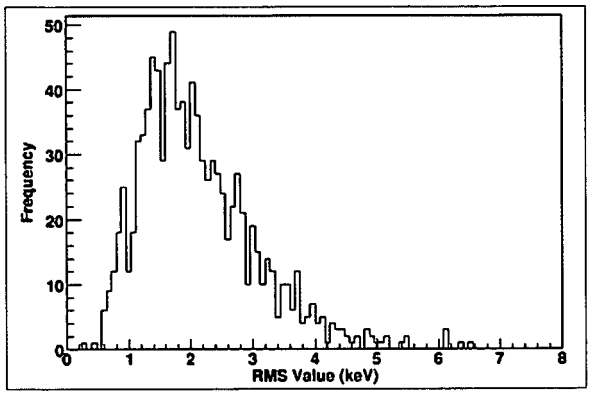

Figure 6.11: Frequency of RMS values calculated from samples along the baseline. 1000 pulses were used from the same scan position.

The nature of the noise was investigated by determining the mean deviation of pulse noise which was oscillating about the baseline. This is shown in Figure 6.10, where it can be seen that the baseline of the majority of the pulses fluctuates above and below the baseline by equal amounts, i.e. most pulses had a mean deviation of zero, meaning that for most pulses, the noise present was oscillating equally above and below a common baseline value. However this does not indicate the amount of noise that was observed on the pulses. In order to quantify the amount of noise present from one pulse to another, the Root Mean Square of the baseline was calculated, prior to the beginning of the pulse. This parameter is commonly calculated to describe the average deviation of a signal from a baseline.

The RMS values calculated from the DC pulses (from a scan position within DC30-AC13) are plotted in Figure 6.11. It can be seen that the majority of pulses had an RMS baseline value of around 2 keV. In general the minimum noise present was about 0.5 keV RMS and the maximum about 5 keV RMS. Each pulse was assigned an RMS value and could therefore be selected based on these values. Figure 6.12 compares 20 pulses from a set of 100 pulses. To the left they are chosen at random, and to the right, they are chosen as the 20 pulses from the same set of 100 pulses with the lowest

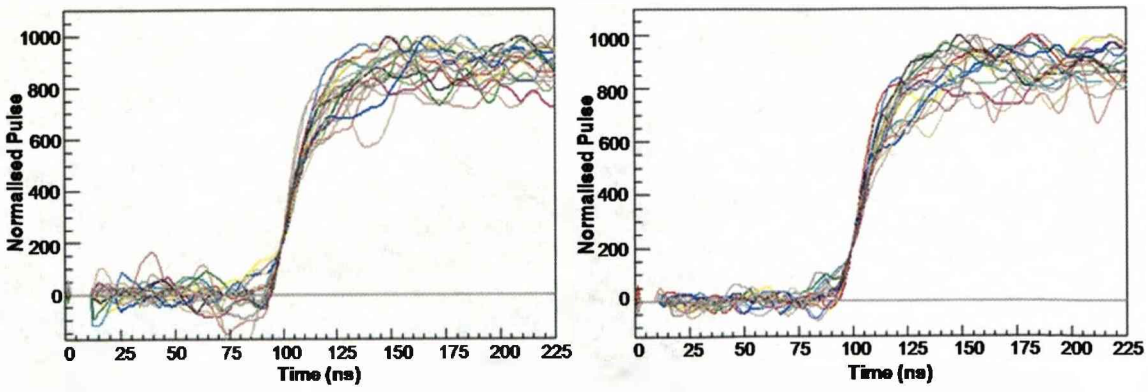

Figure 6.12: Left: Random selection of 20 unfiltered pulses from 60 keV photons (Figure 6.9). Right: Selection of 20 pulses with the lowest RMS baseline values from the first 100 hundred pulses from which the pulses shown left are chosen. Both sets of pulses have been time aligned at 20 percent of their final magnitude and normalised to 1000.

baseline RMS values.

6.2.6 Pulseshape Filtering

It can be seen that RMS filtering provided an effective method to accept the least noisy pulses from a given set of data. It can also be seen from Figure 6.12 that there appeared to be a variance in pulseshape, even amongst those pulses which have been filtered for noise. To eliminate those pulses with the least similar pulseshapes a chi-squared rejection method was implemented. This worked by ranking each pulse according to its deviation from the average pulseshape created from the remaining pulses in the data set, allowing the selection of the most similar shaped pulses. Figure 6.13 shows pulses from a data set of 1000 pulses from the same scan position. Those in blue are a selection of 20 pulses from the bottom the chi squared ranking method, i.e. they are the pulses whose shape are least representative of the majority. It can be seen that they exhibit a variety of shapes from one another. The red pulses are the 20 pulses whose shape is most common amongst the majority of pulses, and their shape is very similar to one another.

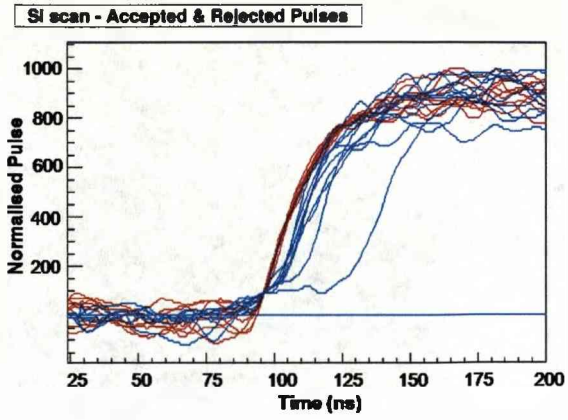

Figure 6.13: Pulseshapes from the same data set of 1000 pulses after being ranked according to their similarity to the majority of other pulses in the data set. Those pulses coloured red are the top 20 pulses after pulseshape filtering, and those coloured blue are the bottom 20.

6.2.7 Pulseshape as a Function of Position

The next step in characterising the detector's pulseshape response was to confirm that the response does not alter in different areas of the same strip. To do this, average pulseshapes were created from several positions from one end of the strip to the other. These average pulseshapes were created from RMS and chi-squared filtered data sets. The strip chosen for this purpose was DC30, which was the strip exhibiting a FWHM energy resolution superior to any other strip (Figure 6.6).

Figure 6.14 shows the average pulseshapes from each of the 150 scan positions across the DC30 strip. The pulse filtering criteria was to accept the 50 percent least noisy pulses, and from those, select the 100 pulseshapes whose shapes are the most similar. These 100 pulseshapes were then considered to be most characteristic of that scan position and were used to create the average pulse. It can be seen that there is very little difference between the pulseshapes from each position. To quantify the similarity of the pulseshapes, the risetimes of each average pulse were plotted in Figure 6.15. It can be seen that the T90 risetimes vary between 22 and 58 ns, and the T30 risetimes

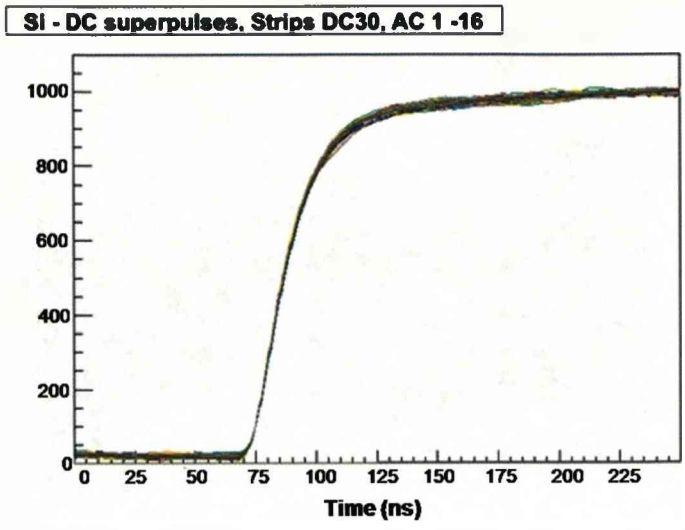

Figure 6.14: Average pulses overlaid for each of the 150 positions across strip DC30 after RMS and CHI filtering.

vary between 5 and 8 ns. The range of risetimes for these average pulses are both quick and similar, as expected from a 0.5 mm thick silicon detector.

In order to investigate whether the remainder of the detector contacts behaved in the same fashion, similar plots were produced for the the other contacts. Ideally one would aim to reproduce the results presented above for each strip, and compare them likewise. This would prove problematic when computational time was factored in, as a single strip (150 positions) requires 12 days sorting time. Based on the knowledge that all the pulses are expected to be of a similar shape due to the small (0.5 mm) separation of each face, it was considered acceptable to determine the risetimes for a scan pixel from a selection of detector strips. This should be adequate to allow confidence that the response does not appreciably differ between detector strips from either the AC or DC face.

Figures 6.16 and 6.17 show the distribution of risetimes for individual events, rather than average pulses, recorded in a single scan position in a selection of strips from

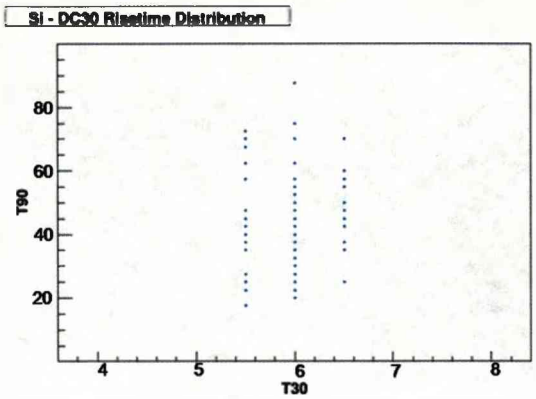

Figure 6.15: distribution of risetimes associated with Figure 6.14.

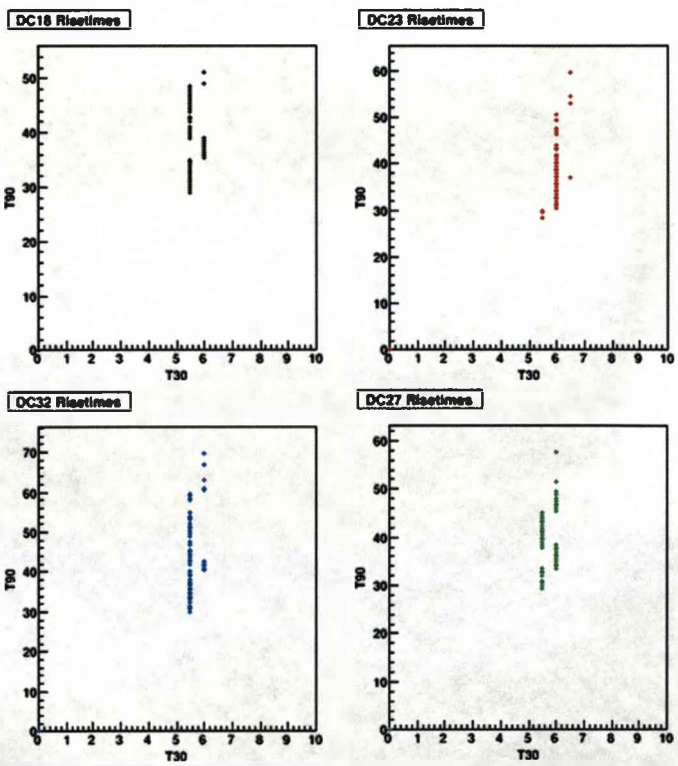

Figure 6.16: Risetime values from a selection of strips across the DC face. From each strip the risetimes are calculated on an event by event basis and are from a single pixel on that strip. The risetimes are calculated after rms and chi filtering.

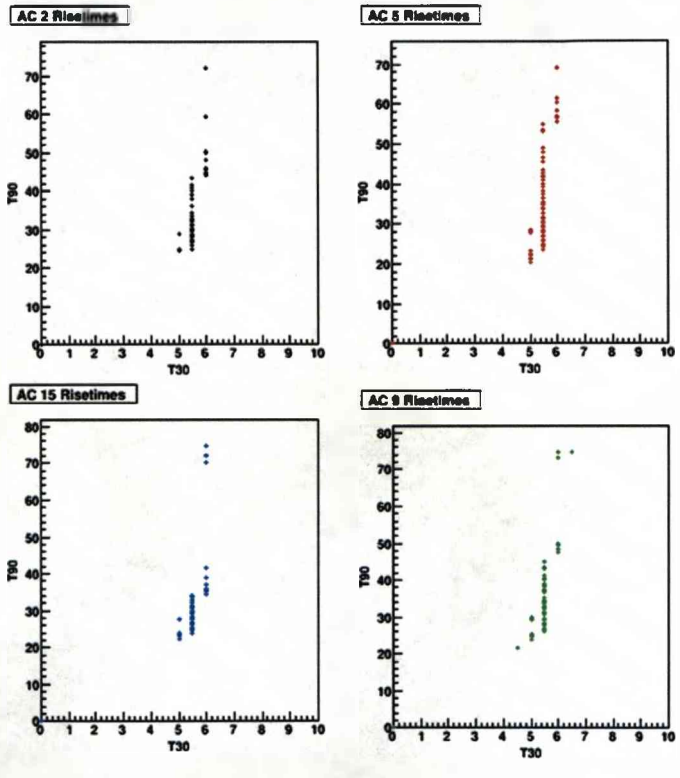

Figure 6.17: Risetime values from a selection of strips across the AC face. From each strip the risetimes are calculated on an event by event basis and are from a single pixel on that strip. The risetimes are calculated after rms and chi filtering.

each face. From the plots it can be seen that the risetimes (and hence the pulseshapes) were suitably similar so as to assume a uniform pulseshape response throughout the detector, as was expected.

6.3 Conclusion

It has been shown through the narrow distribution of risetimes from a selection of positions on each detector face that the pulseshape response appears to be uniform across the detector, as expected due to the small (0.5 mm) separation between each detector face. Unfortunately the high level of noise in the system has prohibited any investigation into the application of pulseshape analysis to refine the position of interaction within a strip, as the presence of any image charges in strips adjacent to the interaction strip were not detectable above the noise. Therefore the position sensitivity achievable by the detector is limited to its segmentation and depth ($3 \times 3 \times 0.5\,\mathrm{mm}^2$).

The noise has serious implications for the viability of ustilising the detector as a scatterer in a low energy Compton camera measurement. This will be discussed further in Chapter Seven.

Chapter 7

Silicon/Germanium Compton Camera

The DSSSD characterised in Chapter Six was subsequently utilised as the scatter detector, replacing the SmartPET germanium detector used in Chapter Four. As discussed previously, the motivation for employing a thin silicon detector as the scatter detector was to enable lower energy γ rays (i.e. energies similar to 141 keV from the current radioisotope used in SPECT imaging ^{99m}Tc), to scatter through to the absorber detector satisfying the Compton imaging requirement. Due to the high level of noise present in the detector (generally between 30 to 40 keV), the CFD threshold was set between the noise level and the 60 keV γ ray from a ^{241}Am source. This resulted in a threshold estimated to be between the noise level previously observed in the system of $\approx$ 40 keV and 60 keV from the ^{241}Am photons. This high threshold prohibits scatters from low energy photons (such as 141 keV) triggering the system. Table 7.1 shows the energy deposited in a Compton scatter interaction for two γ ray energies 141 keV and 662 keV. From the energy deposited by scatters of 141 keV photons, it can be seen that in order to trigger the system (where the CFD threshold is set to be roughly between 40 keV to 60 keV), the photon would need to scatter at an angle of over 120^0. This implies that any photons that do trigger the system would have to scatter at an angle so large they would not be incident on the absorber detector, effectively prohibiting Compton imaging at this energy.

Scatter Angle ^{o}	Energy of Scattered Photon (keV)	Energy in Scattered Detector (keV)	Energy of Scattered Photon (keV)	Energy in Scatter Detector (keV)
0	141	0	662	0
10	139.4	0.6	649.3	12.7
20	137.7	2.3	614.2	47.9
30	135.1	4.9	580.3	81.7
40	131.6	8.4	525.3	136.7
50	127.6	12.4	463.8	198.2
60	123.2	16.8	421.8	240.2
70	118.7	21.3	374.8	287.2
80	114.2	25.8	334.5	327.5
90	110.0	30.0	300.7	361.3
100	106.0	34.0	272.8	389.2
110	102.4	37.6	250.0	412.0
120	99.3	40.7	231.6	430.4
130	96.6	43.4	217.0	445.0
140	94.4	45.6	205.5	456.5
150	92.7	47.3	196.9	465.1
160	91.5	48.5	190.7	471.3
170	90.8	49.2	186.7	475.3
180	90.5	49.5	184.9	477.1

Table 7.1: Table to show the energies of scattered photons and the energies deposited in a detector from those scattered photons for a range of scatter angles.

7.1 Silicon/Germanium Compton camera

The two detectors were setup in Compton camera configuration, with the DSSSD directly in front of the SmartPET detector. A photograph of the setup can be seen in Figure 7.1 and is illustrated in Figure 7.2.

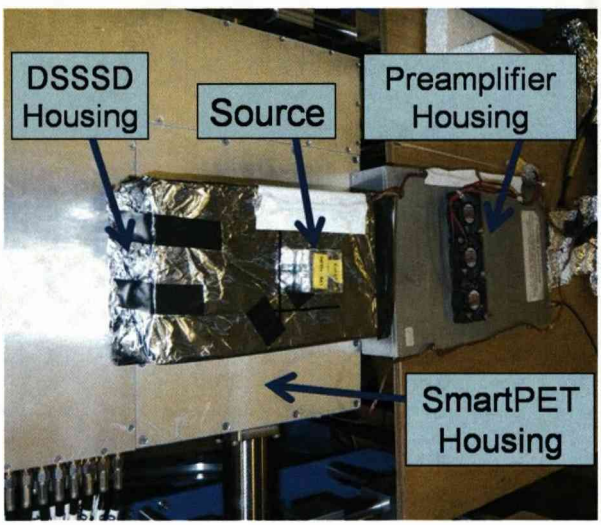

Figure 7.1: Photograph of the DSSSD SmartPET setup illustrated in figure 7.2.

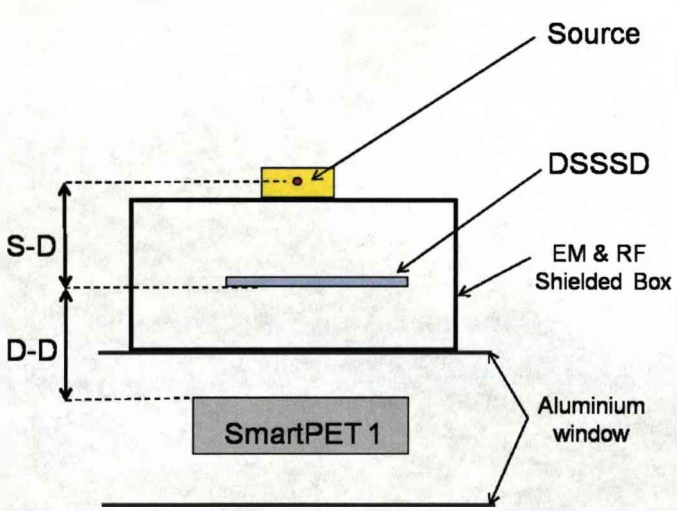

Figure 7.2: Diagram of the Compton camera set up with the DSSSD situated in front of the SmartPET detector, where S-D represents the source to detector distance and D-D the detector separation.

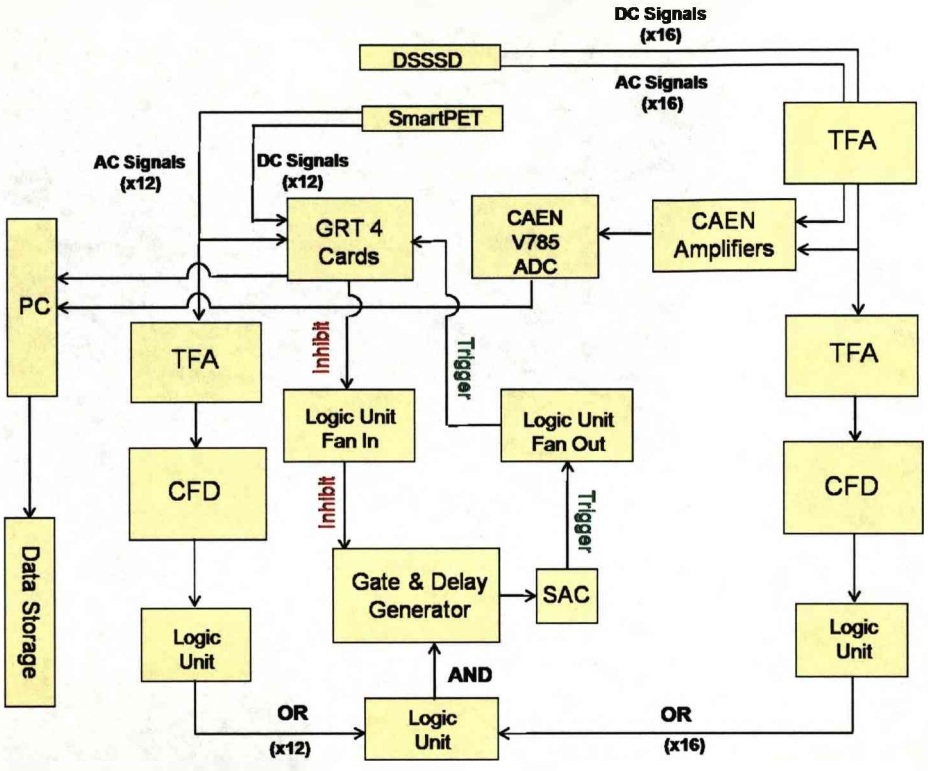

Figure 7.3: Schematic of the DSSSD/SmartPET Compton camera set up.

7.1.1 Data Acquisition System

The two detectors were operated in coincidence with a time window of 100 ns. Both detectors were triggered using conventional NIM electronics as described in earlier chapters. As shown by the DSSSD characterisation in Chapter Six, Pulse Shape Analysis (PSA) could not be applied due to the excessive noise observed in the Silicon system. This fact, coupled with a shortage of GRT4 cards prompted the use of analogue electronics to process the data from the DSSSD. The analogue electronics consisted of; 2×16 channel spectroscopy amplifier (NIM units), V785 32 channel ADC and a V288 controller (VME units), all manufactured by CAEN. These units were integrated into the existing digital system used for the SmartPET detector via an S9418 acquisition control (SAC, VME unit) constructed by STFC Daresbury.

7.2 Experimental Setup

The system was set up with the DSSSD mounted in a light tight EM and RF shielded box, which was wrapped in foil to improve the shielding. This was then situated in front of the SmartPET detector with a point source mounted on the outside of the box level with the center of the DSSSD. A photograph and a diagram of the detector and source arrangement can be seen in Figures 7.1 and 7.2. The Silicon detector was calibrated with a two point linear fit using the 60 keV and 122 keV photopeaks from ^{241}Am and ^{57}Co respectively. These peaks were chosen as the low efficiency for higher energy photons resulted in too lengthy an acquisition time for calibration data. Two data sets were recorded using the DSSSD/SmartPET system, one using a ^{137}Cs source and one using a ^{152}Eu source. The ^{152}Eu source was originally selected to allow an investigation into creating images from low energy photons such as the 121 keV γ rays. Although there is no possibility of creating images at this low energy it was decided to continue to take data with the ^{152}Eu source to determine the operational low energy limit of the system. As was seen by imaging the ^{22}Na source in Chapter Five, difficulty can arise in cone beam reconstruction when imaging multi-line γ sources. For this reason the ^{137}Cs source was also chosen.

7.2.1 Reconstruction Code Modification

As the scatter detector was changed to the the smaller DSSSD, it was necessary to modify the reconstruction code to account for the differences in detector geometry and differing segmentation when creating the reconstruction cones. For ease of set up, the DSSSD was aligned so that one corner of the DSSSD was aligned with the corresponding corner in the SmartPET detector, as illustrated in Figure 7.4.

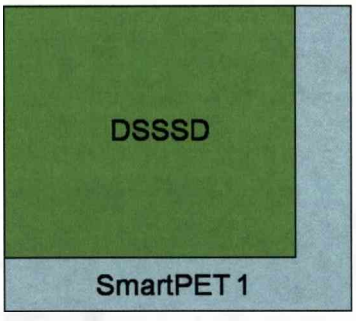

Figure 7.4: Diagram to illustrate the alignment of the DSSSD with respect to the SmartPET 1 detector during the Compton camera measurements.

7.2.2 ^{152}Eu Point Source Measurement

Data were collected using the DSSSD/SmartPET Compton camera system and a 0.1806 MBq ^{152}Eu point source. The source was mounted at a distance of 35 mm from the DSSSD, and was centrally located with respect to the crystal face. The detectors were separated by a distance of 52 mm. Observations from online spectra during the set up for the first measurement showed very few coincidence events between the two detectors and many full energy depositions in the SmartPET detector. This was attributed to the emission of x rays from the ^{152}Eu source with energies of 39.73 keV and 45.26 keV respectively. These x rays are of high enough energy to trigger the system (40 keV CFD threshold) with a full energy deposition in the DSSSD. Consequently, any of the higher energies from ^{152}Eu that pass through the DSSSD within the 100 ns time window will likely interact in the SmartPET detector. This results in an apparent normal ^{152}Eu energy spectrum in the SmartPET detectors with essentially just noise in the DSSSD spectrum (as the x ray energies are only just able to trigger the system and so no peak could be resolved). The solution to this was to attenuate the x rays prior to being incident on the DSSSD whilst still allowing the transmission of the ^{152}Eu γ rays. To achieve this a layer of cadmium (0.97 mm thick) and a layer of aluminum (1.04 mm thick), were inserted between the source and detector casing, which were originally used as graded shielding for low energy spectroscopy experi-

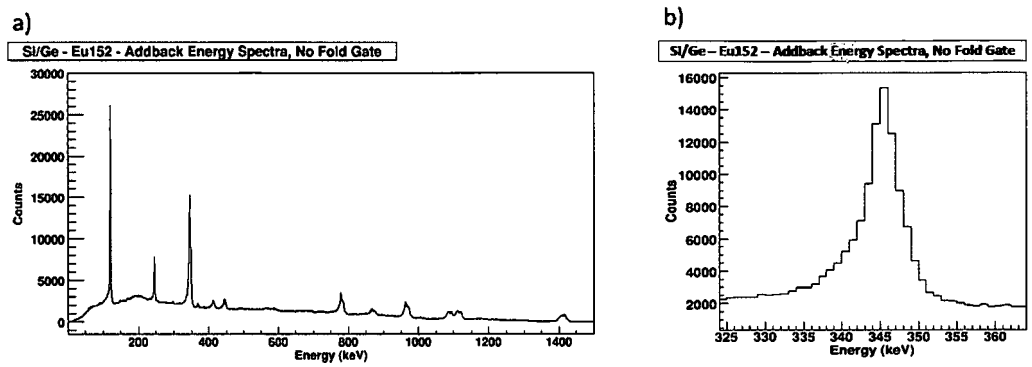

Figure 7.5: Addback spectrum from the DSSSD and SmartPET detector of the ^{152}Eu point source. Part a) shows the addback spectrum obtained by summing the energies recorded from each detector. Part b) shows a magnified view of the 344 keV photopeak that will be used for the reconstructions. The FWHM of this peak is 6 keV.

ments. Their thickness was measured using a digital micrometer. The introduction of this shielding successfully attenuated the x rays whilst allowing the ^{152}Eu γ rays to pass through. Following this action, the system behaved as expected.

The data acquired totaled 17 GB and was collected over a 119 hour period. The acquisition was left to run until there were over 5000 counts in the 344 keV addback peak, with a fold 1 condition in each detector, so as to ensure that there would be a reasonable amount of events for subsequent imaging.

The total number of events in the addback spectrum with no fold gate was 2 million events, of which 134 K are in the photopeak. The photopeak is defined between the energies 330 and 354 keV. Figure 7.5 part a) shows the addback spectrum obtained by summing the energies recorded from each detector. Figure 7.5 part b) shows a magnified view of the 344 photopeak. In contrast to the addback photopeaks observed in the SmartPET1/SmartPET2 addback spectra, there are no high energy shoulders to be seen on the addback photopeak. It can be seen in Figure 7.5 part a) that the 344 keV peak sits upon a large distribution of what are likely to be multiple scatters

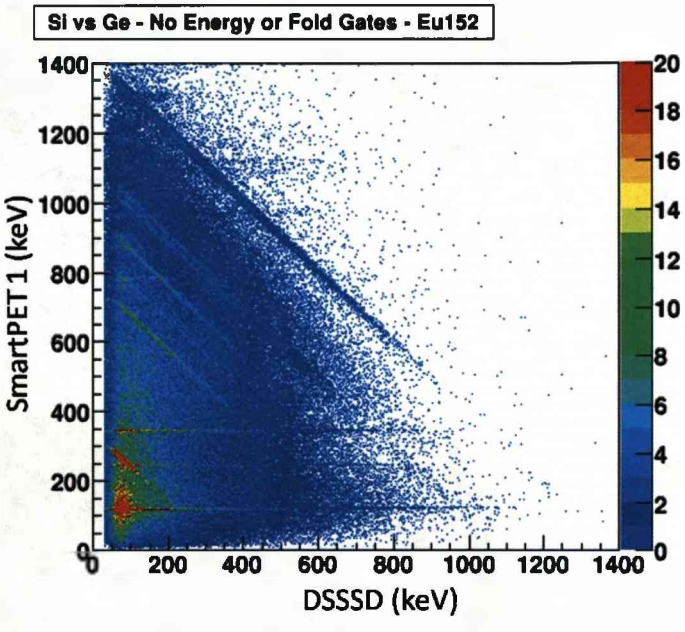

Figure 7.6: Plot of the energies recorded from the DSSSD (x axis) plotted against the energies from SmartPET 1 (y axis), where events sharing their full energy between the two detectors fall along the diagonal lines between the two axis. The lines parallel to the x axis correspond to suspected random coincidences where the system has triggered but a full energy deposition occurs in SmartPET 1. These are not observed at the higher energies, presumably due to the higher energies scattering through SmartPET 1 as opposed to being absorbed.

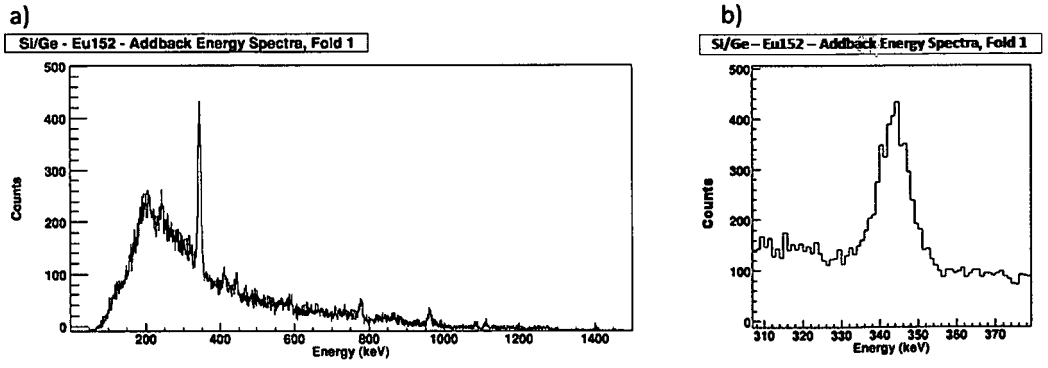

Figure 7.7: Addback spectrum from the two detectors of the ^{152}Eu point source with a fold 1 criteria applied. Part a) shows the addback spectrum after a fold 1 condition is applied to both detectors. Part b) zooms in on the photopeak showing which is similar to the no fold peak with the exception of vastly reduced statistics due to the fold 1 requirement. The FWHM of this peak is 10 keV.

from other energies, making any high energy shoulder from higher fold event less prominent.

Figure 7.6 shows the energies from the DSSSD plotted against the energies in Smart-PET 1, where events sharing their full energy between the two detectors fall along the diagonal lines between the two axis. The lowest energy at which a diagonal line can be seen is at 344 keV. At energies lower than this no definite diagonal line can be seen. The 40 keV threshold set for the DSSSD is also apparent as there were no events present below this value on the DSSSD axis. It can be seen that the maximum energy deposition in the DSSSD from the higher intensity region of the diagonal 344 keV line was approximately 120 keV. This suggests a maximum common scattering angle of around 80^0, which indicates that scatters at larger angles than 80^0 were less likely to be incident on the absorber detector. The minimum energy of the intense region of the 344 keV diagonal line lies at about 50 keV which corresponds to a minimum scattering angle of roughly 45^0. Scatter angles smaller than this would not deposit the required energy to trigger the system.

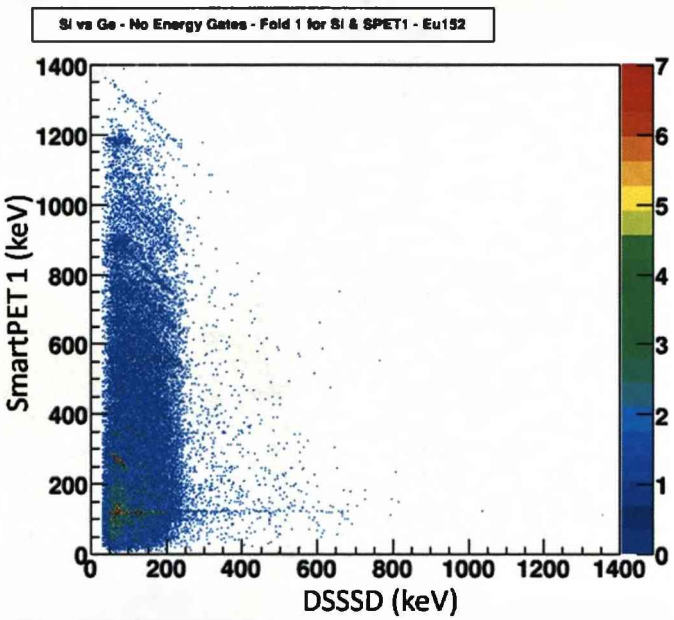

Figure 7.8: Plot showing energies from the DSSSD plotted against the energies in SmartPET 1, where the potentially usable events (full energy shared between the detectors via a fold 1 interaction in each detector), fall along the diagonal line between 344 keV.

As mentioned in Chapter Five, the reconstruction code requires that the events to be reconstructed satisfied a fold 1 condition in both detectors, corresponding to a scatter and an absorption. When a fold 1 requirement was imposed on the data, the total number of events is 75498, with 5962 of those events occurring in the photopeak. Figure 7.7, part a) shows the addback spectrum after a fold 1 condition is applied to both detectors. Figure 7.7 b) shows a magnified view of the 344 keV photopeak. Figure 7.8 shows the energies from the DSSSD plotted against the energies in SmartPET 1, where the potentially usable events (full energy shared between the detectors via a fold 1 interaction in each detector), fall along the diagonal lines between the two axis. As expected, when a fold 1 criteria was applied to the data the statistics were drastically reduced. The region of intensity on the 344 keV diagonal line still appeared to be within the same energy deposition range in the DSSSD, i.e. between 50 and 120 keV, implying that the range of common scatter angles was still between 45^0 and 80^0. Each reconstruction of this data set used the total 5962 events. The same exact events are used in each reconstruction.

7.2.3 ^{152}Eu Point Source Reconstruction

No PSA could be applied to the DSSSD due to the use of analogue electronics, so all events were placed at the centre of the interaction strip. PSA could still be applied to the interactions occurring in SmartPET 1, which continued to use digital electronics. All the PSA risetime combinations used for the ^{137}Cs point source in Chapter Five were be employed on both sets of DSSSD/SmartPET 1 data. It was expected that the source should be located around the z projection slice of 107. Each slice corresponds to a millimeter along the z axis, where 0 mm was situated at the back plane of the SmartPET detector. The SmartPET detector was 20 mm thick, the DSSSD was located 52 mm in front of the SmartPET detector and had a thickness of 0.5 mm. The source was located at a distance of 35mm from the DSSSD, implying the source location should be at 107.5 mm. Based on this information, the following

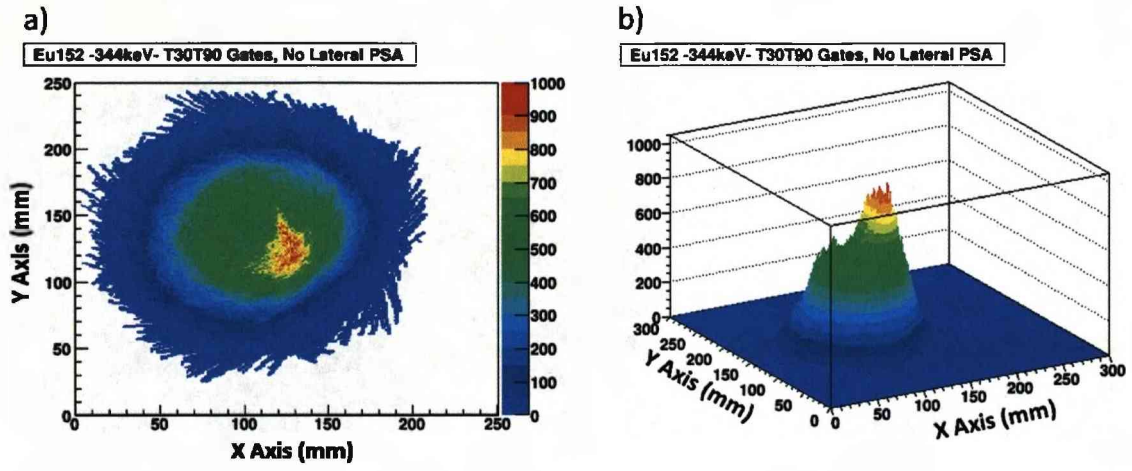

Figure 7.9: Reconstruction of the ^{152}Eu point source using the original T30T90 gates and the 344 keV photon. The source was at a distance of 35mm from the face of the DSSSD. a) 2D profile of the xy plane corresponding to the source position. b) 3D profile of the xy source plane.

reconstructions were created at the z plane of 107.

It can be seen from Figure 7.9 that the reconstruction was not as localised as that obtained using the SmartPET1/SmartPET2 system, but is distributed in an arc shape. It is not fully understood why this has occurred. Possible reasons could be due to a combination of low statistics, incorrect identification of events (as many of the events within the addback energy gates for the 344 keV peak could have resulted from scatters from the higher energy photons emitted from the source), and a restricted range of scatter angles available due to the minimum energy required to trigger the DSSSD. Although these images were of low quality an attempt was still made to compare the localisation achieved with each of the PSA combinations. As in Chapter Five, this was quantified with the FWHM and FWTM parameters. The results are presented in Table 7.2

From Figure 7.10 it can be seen that based on the average resolution of both the x and y planes that the SmartPET risetime gates of T30T90 without lateral PSA

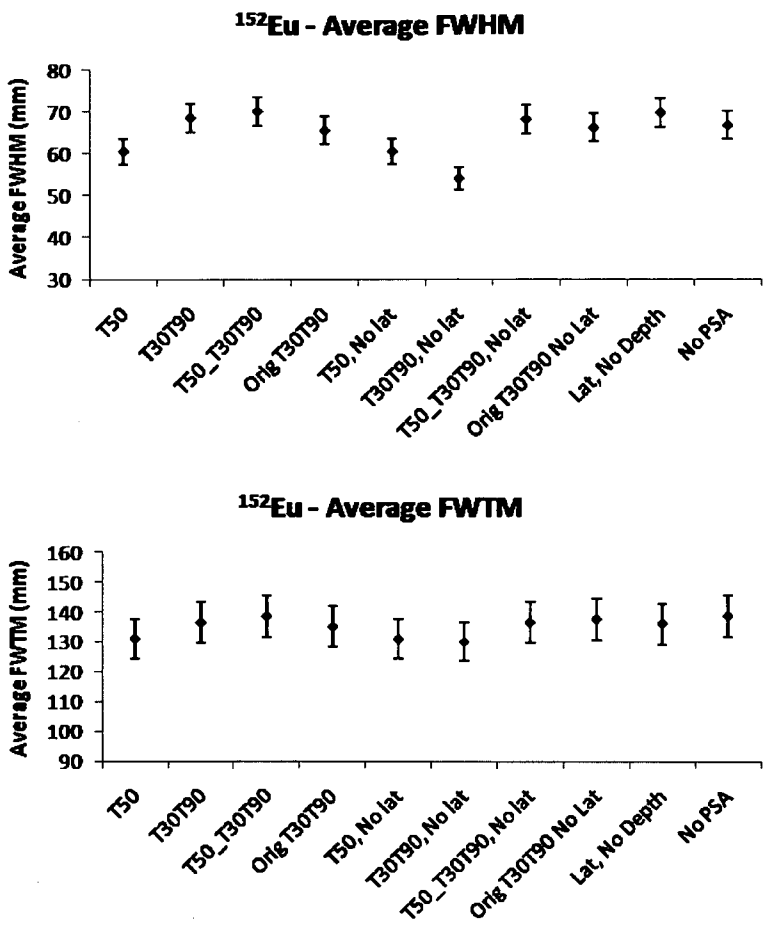

Figure 7.10: Position resolutions from the x plane averaged with those from the y plane. A 5 percent error for each value has been assumed and is plotted for each point.

PSA Gates	FWHM X	FWHM Y	FWTM X	FWTM Y	Average FWHM	Average FWTM
T30T90 No Lat	59	49	134	126	54.0	130.0
T50 No Lat	71	50	134	128	60.5	131.0
T50 With Lat	71	50	134	128	60.5	131.0
Orig T30T90 With Lat	69	62	139	131	65.5	135.0
Orig T30T90 No Lat	75	57	138	137	66.0	137.5
No PSA	70	63	140	137	66.5	138.5
T30T90T50 No Lat	72	64	139	134	68	135.5
T30T90 With Lat	72	65	138	135	68.5	136.5
Lateral No Depth	73	66	139	133	69.5	136.0
T30T90T50 With Lat	73	67	141	136	70	138.5

Table 7.2: Table of position resolutions measured from the reconstruction of a ^{152}Eu point source positioned at 35 mm from the scatter detector with a detector separation of 52 mm. The gates used have been listed in order of best average FWHM from top to bottom. Units are millimeters.

appeared to provide the best resolution out of the whole group of possible risetime gate combinations, when imaging 344 keV γ rays using the DSSSD/SmartPET system.

An investigation to determine the ability of the DSSSD/SmartPET system to

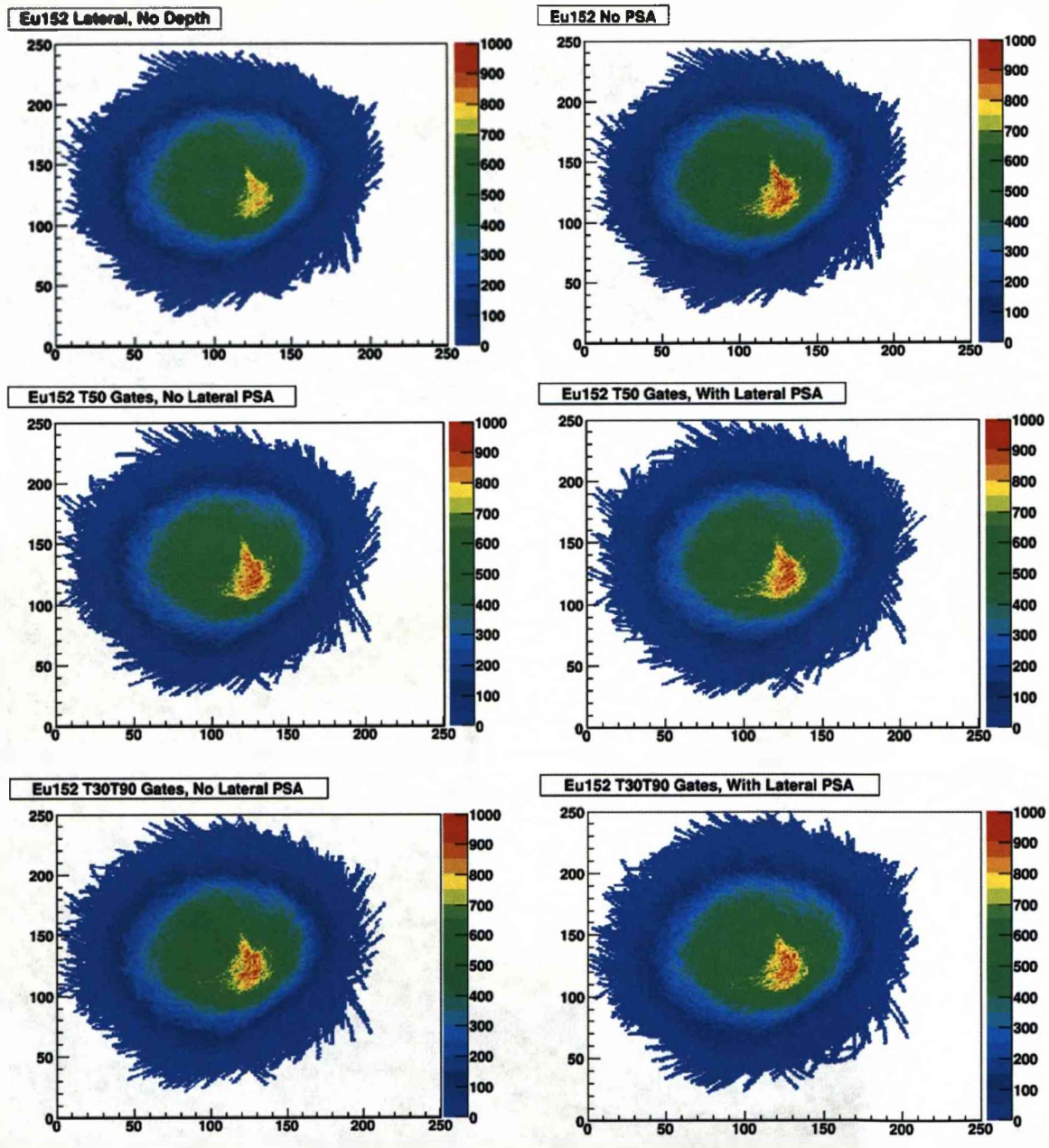

Figure 7.11: Reconstructions of the ^{152}Eu point source using the various combinations of gates. The 344 keV γ ray was used. The source is at a distance of 35mm from the face of the DSSSD, corresponding to z plane 107. All axis units are millimeters

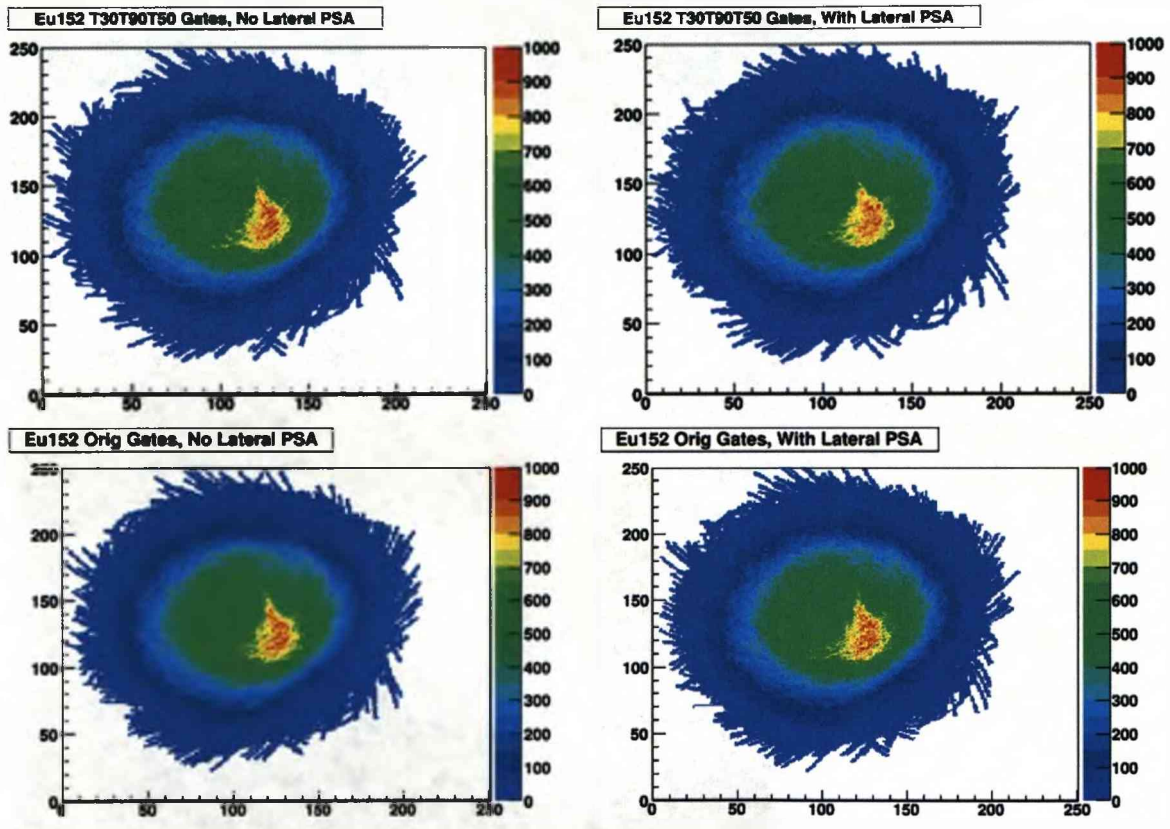

Figure 7.12: Reconstructions of the ^{152}Eu point source using the various combinations of gates. The 344 keV γ ray was used. The source is at a distance of 35mm from the face of the DSSSD, corresponding to z plane 107. All axis units are millimeters

localise the source along the Z axis was attempted. As in Chapter Five, a distribution along the z axis is created by calculating the ratio of the highest number of counts in one element of a plane to the sum of the total counts in that same plane, for each of the two hundred planes. The results for the ^{152}Eu measurement are shown in Figures 7.13 and 7.14. It was expected that the source should be located around the Z projection slice of 107. It can be seen that there were slight increases in statistics around this area for each reconstruction. Due to the low statistics and lack of gaussian shape a quantitative assessment of their performance relative to each other was not possible, however the original T30T90 gates with lateral PSA arguably perform better than the other gates.

From the analysis performed on the ^{152}Eu data recorded using the DSSSD/SmartPET Compton camera it has been found that the T30T90 gates with no lateral PSA provide the best resolution from images created in the xy plane. The distributions used to locate the source along the z axis were not suitable to quantify the performance of each combination of gates used, however it can be observed that the original gates with lateral PSA applied appeared to provide greater localisation than the other gates.

7.2.4 ^{137}Cs Point Source Measurement

Data were next collected with the DSSSD/SmartPET Compton camera system of a 0.273 MBq ^{137}Cs point source. The source was mounted at a distance of 33 mm from the DSSSD, and was centrally located with respect to the crystal face. No shield was required for this measurement as the 32 keV x ray associated with ^{137}Cs was not a high enough energy to trigger the system (40 keV CFD threshold) so the source was now situated 2mm closer than for the ^{152}Eu measurement. The detectors were separated by a distance of 52 mm. The data acquired totaled 15 GB and was collected over a 102 hour period. This collection time was determined via the use of an online addback energy spectrum used to observe the number of counts within the 662 keV peak. As with the previous measurement, the acquisition was left to run until there were over

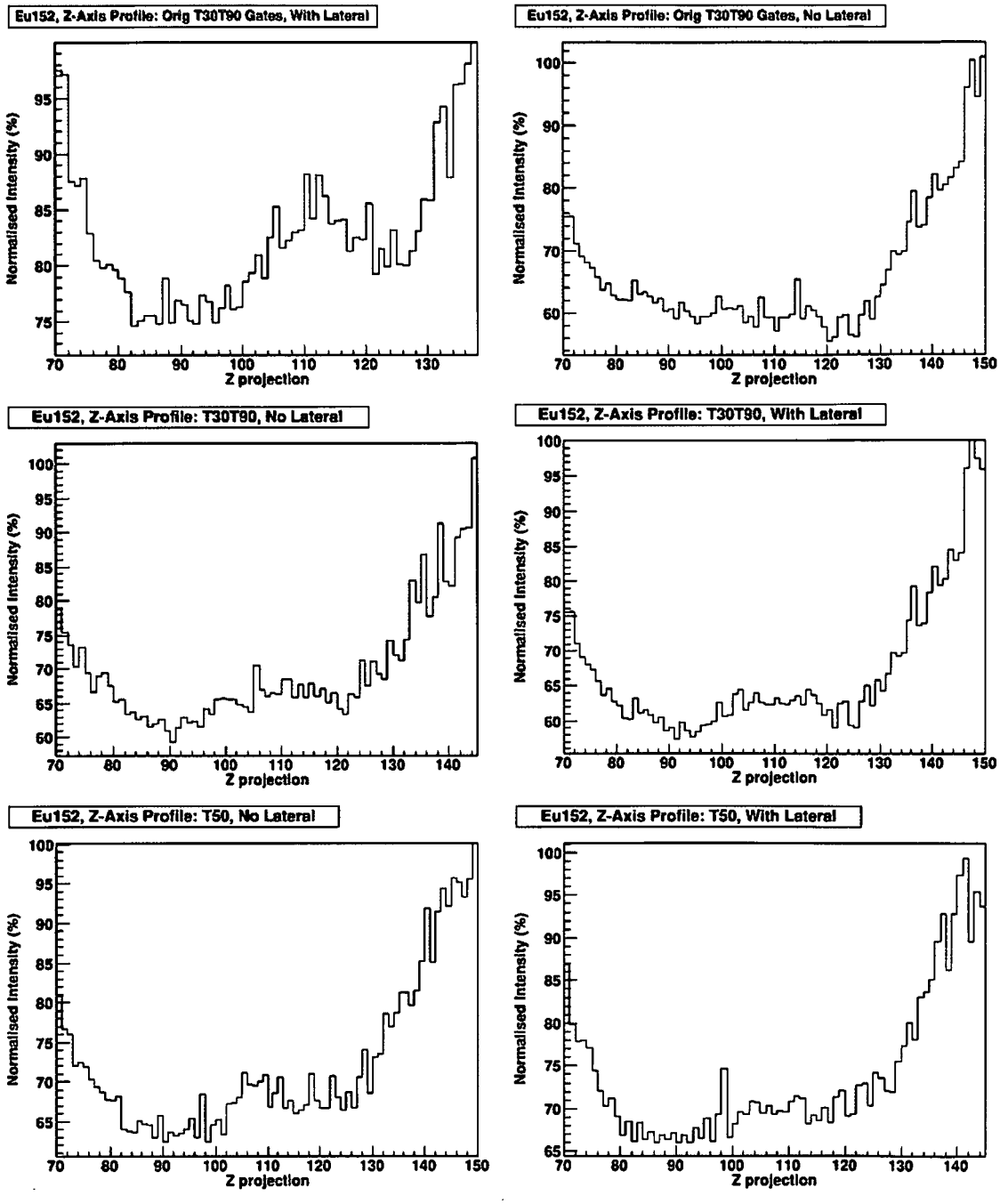

Figure 7.13: Distributions used to determine the localisation of the source along the z axis. The distributions are created by calculating the ratio of the highest number of counts in one element of a plane to the sum of the total counts in that same plane, for each of the two hundred planes. The source was estimated to be around z plane 107 from experimental measurement. Due to the poor statistics and lack of gaussian shape it was not possible to perform a quantitative comparison of their performance relative to each other, although the original T30T90 gates with lateral PSA appear superior to the other gates.

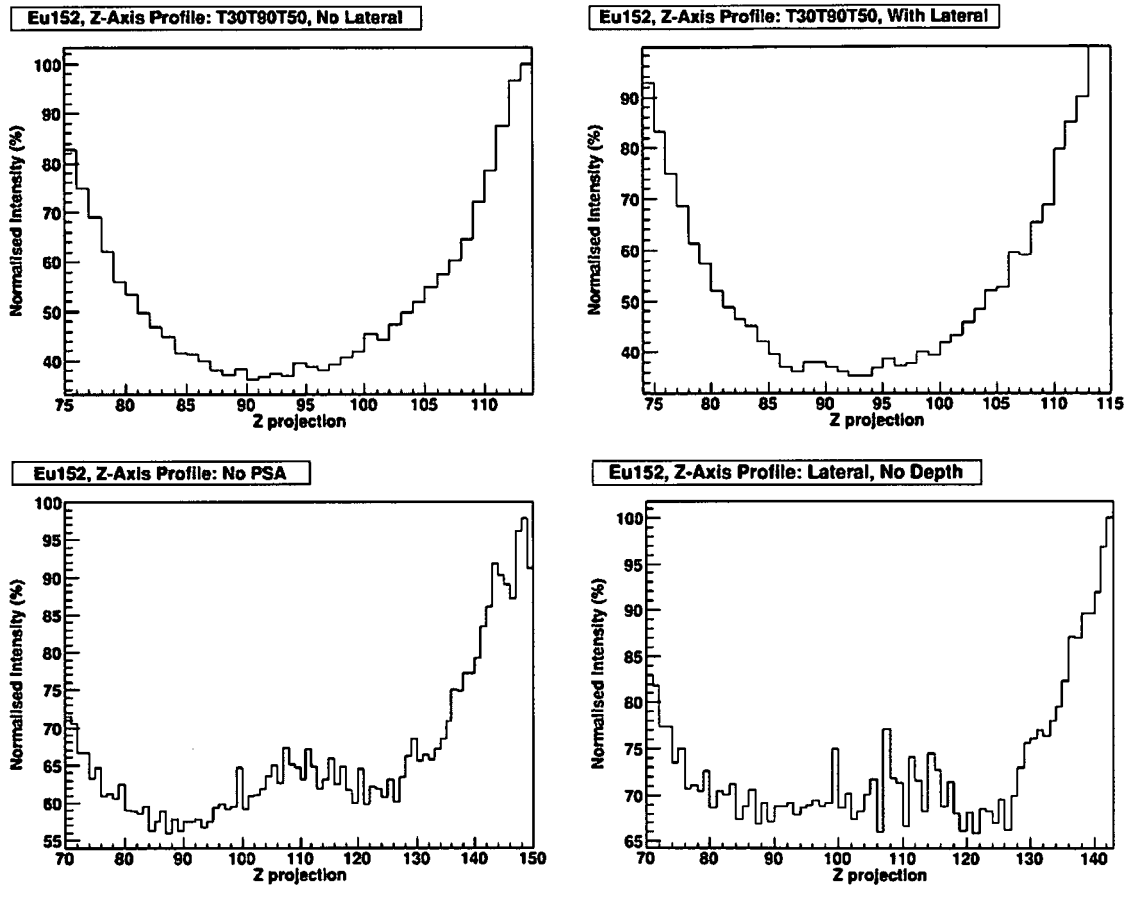

Figure 7.14: Distributions used to determine the localisation of the source along the z axis. The source was estimated to be around z plane 107 from experimental measurement. The distributions from using no PSA and lateral PSA but no depth information exhibit an increase in intensity around the expected region. The distributions from the T30T90T50 gates show no such trend.

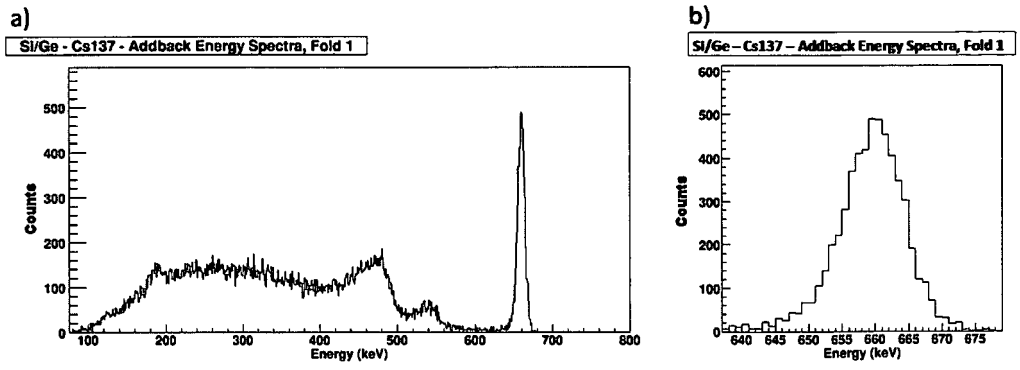

Figure 7.15: Addback spectrum from the DSSSD and SmartPET detector of the ^{137}Cs point source. Part a) shows the addback spectrum obtained by summing the energies recorded from each detector. Part b) shows a magnified view of the 662 keV photopeak that will be used for the reconstructions. A high energy shoulder can again be observed resulting from multiple fold events in the detectors, probably as a result of cross talk between the strips. The FWHM of this addback peak is 11 keV.

5000 counts in the 662 keV addback peak, with a fold 1 condition in each detector.

The total number of events in the addback spectra with no fold gate was 1807158 events, of which 297367 were in the photopeak. The photopeak is defined between the energies 650 and 670 keV. Figure 7.15 part a) shows the addback spectrum obtained by summing the energies recorded from each detector. Figure 7.15 part b) shows a magnified view of the 662 photopeak. The presence of a high energy shoulder on the photopeak can be seen, as in the SmartPET1/SmartPET2 fold 1 addback spectra, due to multiple fold events in the detectors resulting in cross talk effects between strips. The cross talk is the result of undesired coupling between the detector electrodes. Figure 7.16 shows the energies from the DSSSD plotted against the energies in SmartPET 1, where events sharing their full energy between the two detectors fall along the diagonal lines between the 662 keV markers on each axis. As in Figure 7.6, there are no events below 40 keV on the DSSSD axis due to the CFD threshold being set at that value. The region displaying the higher intensity (coloured red in Figure

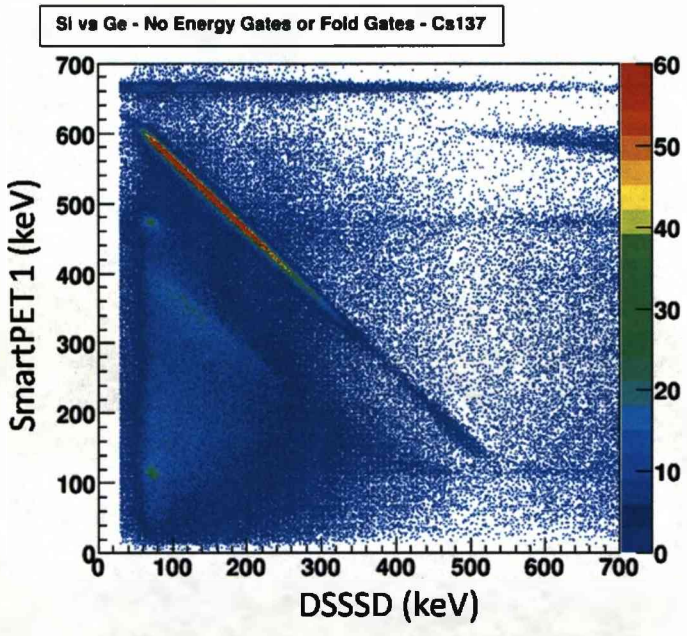

Figure 7.16: Plot of the energies recorded from the DSSSD (x axis) plotted against the energies from SmartPET 1 (y axis), where events sharing their full energy between the two detectors fall along the diagonal line between 662 keV along the two axis.

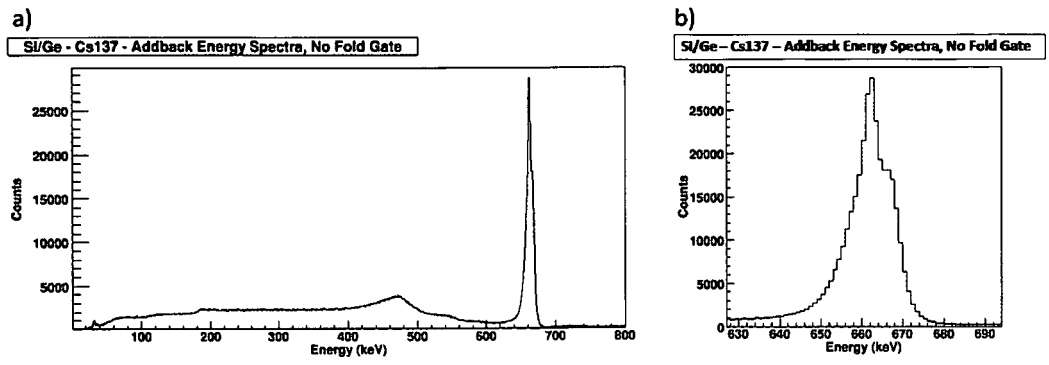

Figure 7.17: Addback spectrum from the two detectors of the ^{137}Cs point source with a fold 1 criteria applied. Part a) shows the addback spectrum after a fold 1 condition is applied to both detectors. Part b) zooms in on the photopeak. It can be seen that the fold 1 condition has removed the high energy shoulder which is attributed to multiple fold events in SmartPET 1. The FWHM of this peak is 10 keV.

7.16) of events whose energy is shared between the detectors deposits between 70 keV and approximately 250 keV. These energies correspond to common scattering angles of between 25^0 and 58^0.

Applying a fold 1 requirement to the data results in a total of 62807 events in the addback spectrum (Figure 7.17), with 5452 of those events occurring in the photopeak. Part a) shows the addback spectrum after a fold 1 condition was applied to both detectors. Figure 7.17 b) shows a magnified view of the 662 keV photopeak showing that the high energy shoulder present in multiple fold addback spectrum has been removed. There is an unexpected bump present between the photopeak and the high energy Compton edge in the spectra between the energies 520 keV and 560 keV. This can also be seen the multi fold addback spectrum (Figure 7.15) but is far less prominent. A proposed scenario to explain this is the 662 keV photons passing through the DSSSD without interacting, backscattering (180^0) off the SmartPET detector, depositing approximately 478 keV. If the backscattered photon is then incident on the DSSSD and also backscatters (depositing 77 keV), this sums to 555 keV. Obviously,

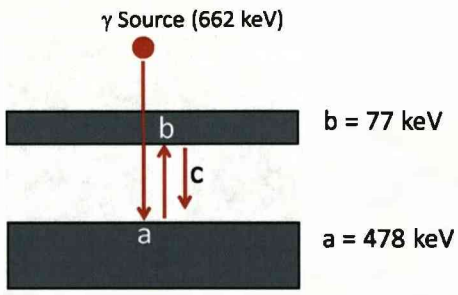

Figure 7.18: Diagram to show the proposed sequence of interactions responsible for the bump seen in the fold 1 addback spectra between the photopeak and the Compton edge (Figure 7.17. The 662 keV photons pass through the DSSSD without interacting, backscatter (180^0) off the SmartPET detector and depositing approximately 478 keV. If the backscattered photon is then incident on the DSSSD and also backscatters (depositing 77 keV), this sums to 555 keV. Obviously, slightly shallower scatters will deposit slightly less energy, resulting in the range of energies seen within the bump between 520 and 560 keV.

slightly shallower scatters will deposit slightly less energy, resulting in the range of energies seen between 520 and 560 keV. This suggested sequence of events is illustrated in Figure 7.18.

Figure 7.19 shows the energies from the DSSSD plotted against the energies in SmartPET 1. Those events deemed usable fall along the 662 keV diagonal line between the two axis. The energies at which the intensity of events in the DSSSD drops appears to be between 80 and 200 keV, corresponding to a range of possible scatter angles from 27^0 to 48^0. For each reconstruction 5452 events were used. The same events were used each time.

7.2.5 ^{137}Cs Point Source Reconstruction

The images for the ^{137}Cs source were created using each of the PSA combinations and can be seen in Figures 7.20 and 7.21. As shown in the ^{152}Eu reconstructions, it can be seen that all reconstructions displayed good localisation in the xy plane.

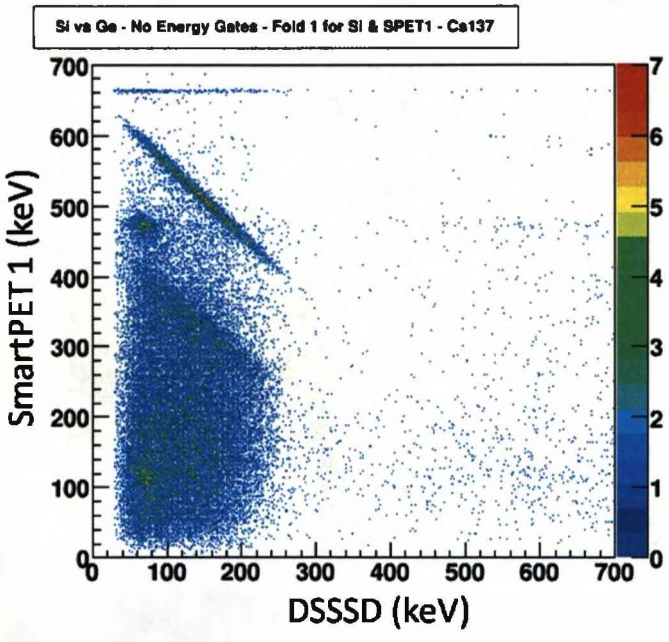

Figure 7.19: Plot showing energies from the DSSSD plotted against the energies in Smart-PET 1, where the potentially usable events (full energy shared between the detectors via a fold 1 interaction in each detector), fall along the diagonal line between 662 keV.

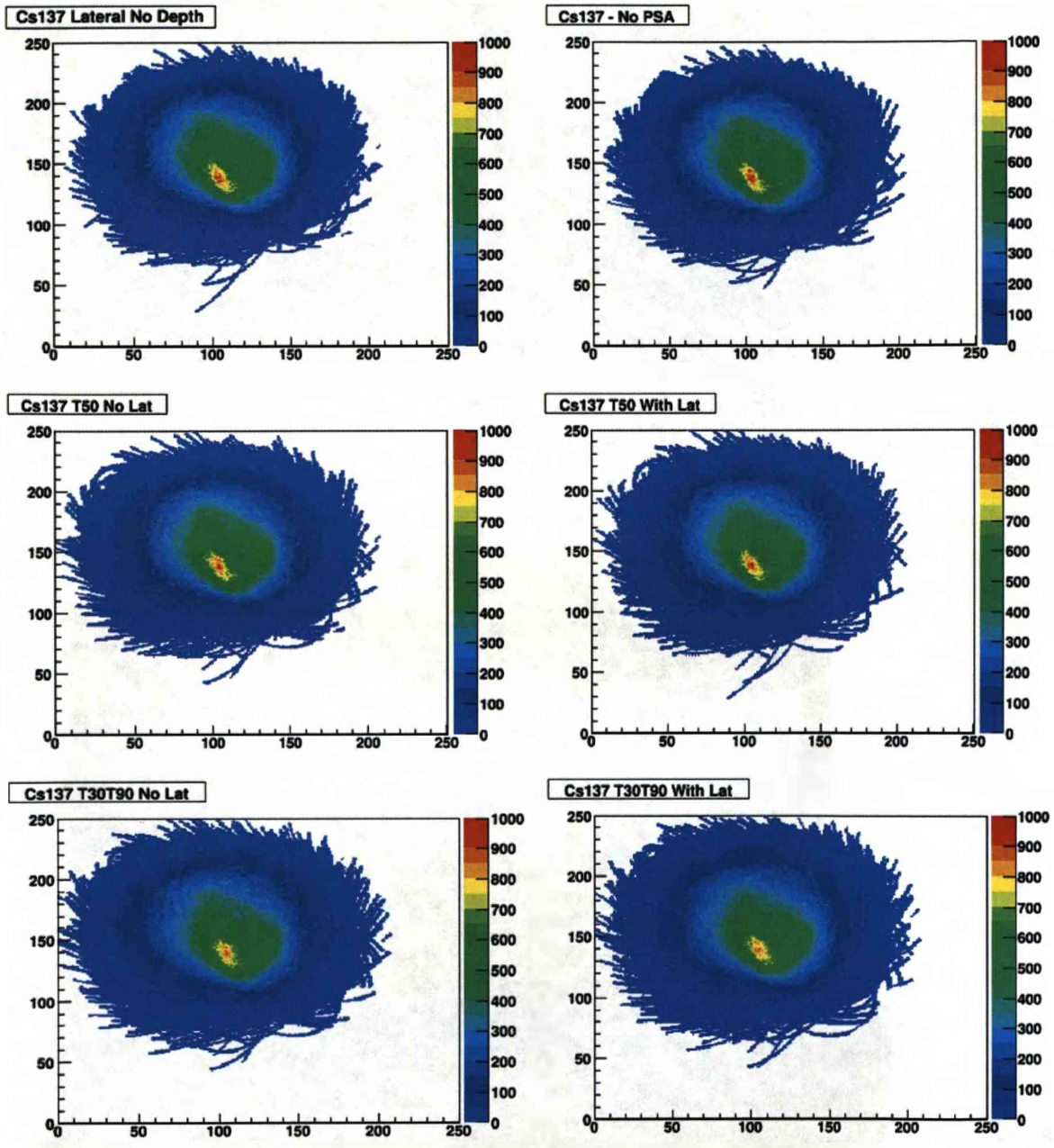

Figure 7.20: Reconstruction of the ^{137}Cs point source using the various combinations of gates. The source is at a distance of 33mm from the face of the DSSSD. All axis units are millimeters.

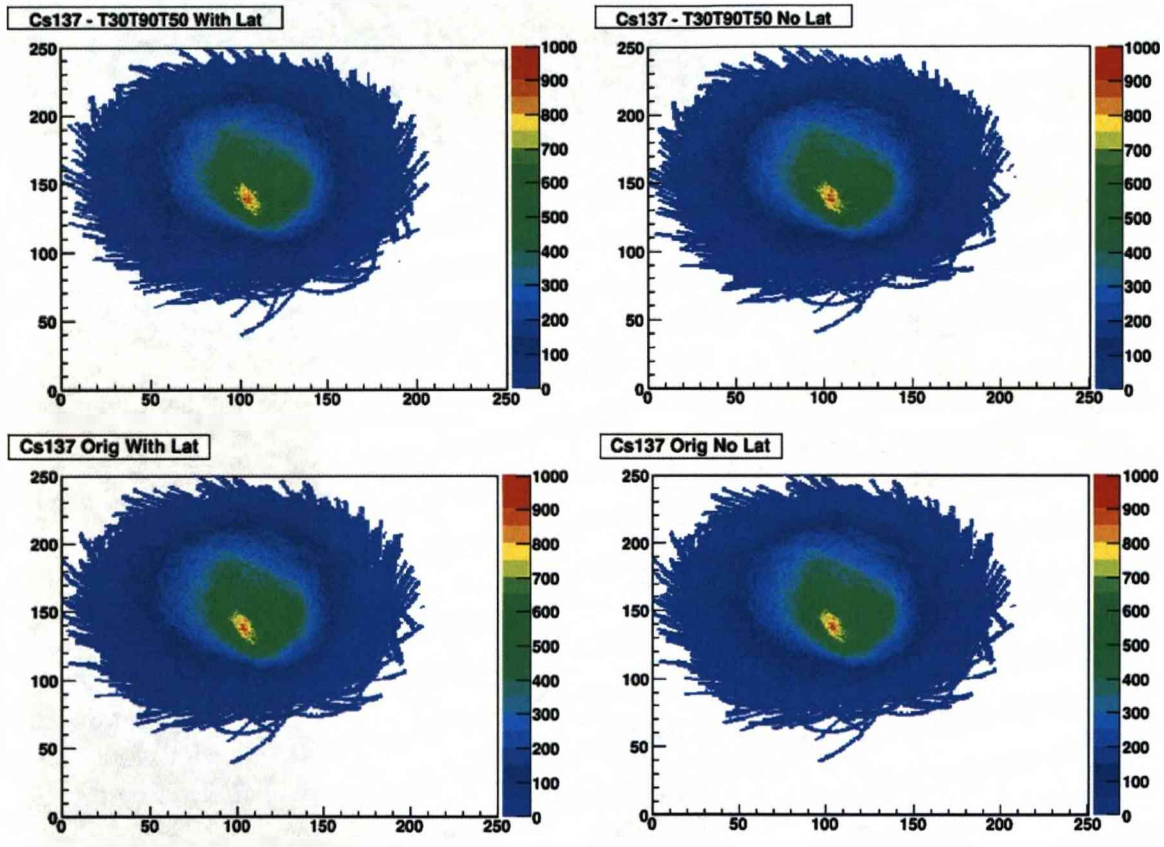

Figure 7.21: Reconstruction of the ^{137}Cs point source using the various combinations of gates. The source is at a distance of 33mm from the face of the DSSSD. All axis units are millimeters

Table 7.3 summarises the resolutions in terms of FWHM and FWTM derived from the ^{137}Cs images. The average values are displayed in Figure 7.22. The optimum PSA based on the FWHM was the original T30T90 gates no lateral PSA applied, which achieved an average resolution of 24 mm. Based on the FWTM the best average resolution was from the T30T90 gates with lateral PSA applied, with a resolution of 76 mm.

The final aspect of the analysis was to quantify the systems ability to localise the source in the z plane. The ^{152}Eu data showed some slight gain in intensity around the expected region but the statistics proved too low to quantify the level of localisation. Figures 7.23 and 7.24 show the distributions which are used to localise the source along the Z axis by applying each of the PSA gates combinations. From experimental measurement the source should be situated around 105 mm. Unfortunately for this set of reconstructions no increase in intensity is present around the expected area, implying that no localisation along the z axis was possible for this data set. This is suspected to result from a combination of factors; incorrect identification of events (scatters from higher energy photons being identified as that of 344 keV) and low number of total events with respect to the data sets for the SmartPET1/SmartPET2 system.

The work in this chapter has obtained images from two point sources. The 2d images in the xy plane from the ^{152}Eu source found that the PSA that achieved the finest resolution, both FWHM and FWTM, was the T30T90 gates with no lateral PSA applied when imaging 344 keV γ rays. The values of the resolutions were 54 mm for the FWHM and 130 mm for the FWTM. No quantification of the localisation performance could be made along the z axis due to poor statistics and the lack of a gaussian shape. From the reconstructions of the ^{137}Cs source the optimum PSA to be applied differed depending on whether FWHM or FWTM resolution parameters were chosen. For the FWHM parameter, the original T30T90 gates no lateral PSA applied were the best performing gates, achieving an average position resolution of 24 mm.

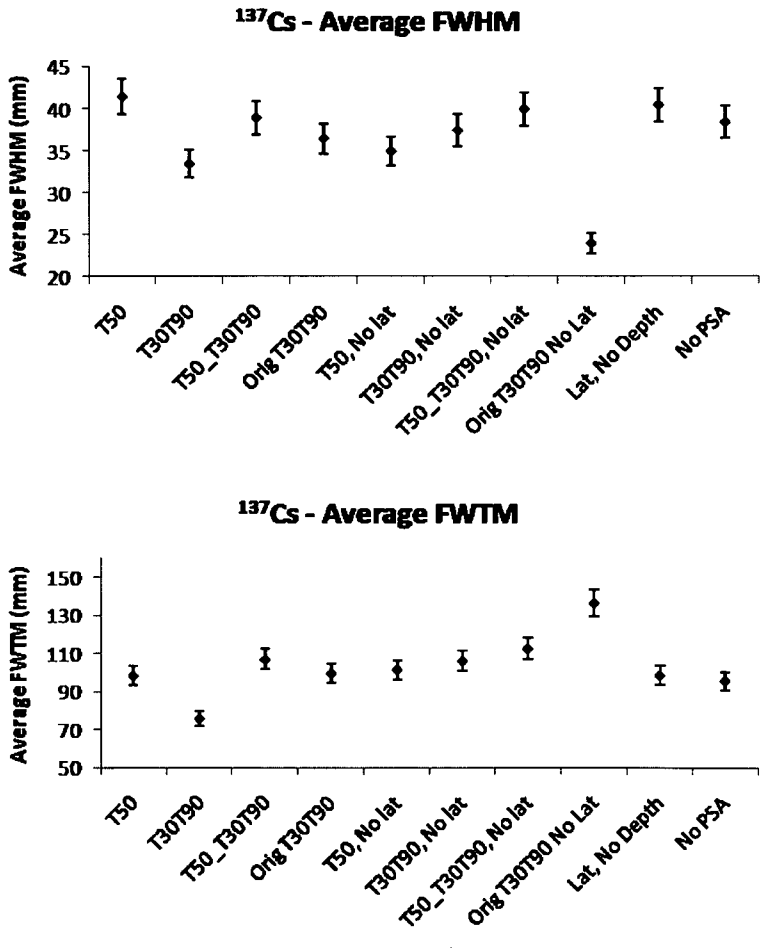

Figure 7.22: Average resolutions in the xy plane of the ^{137}Cs point source reconstructions presented with a 5 percent error.

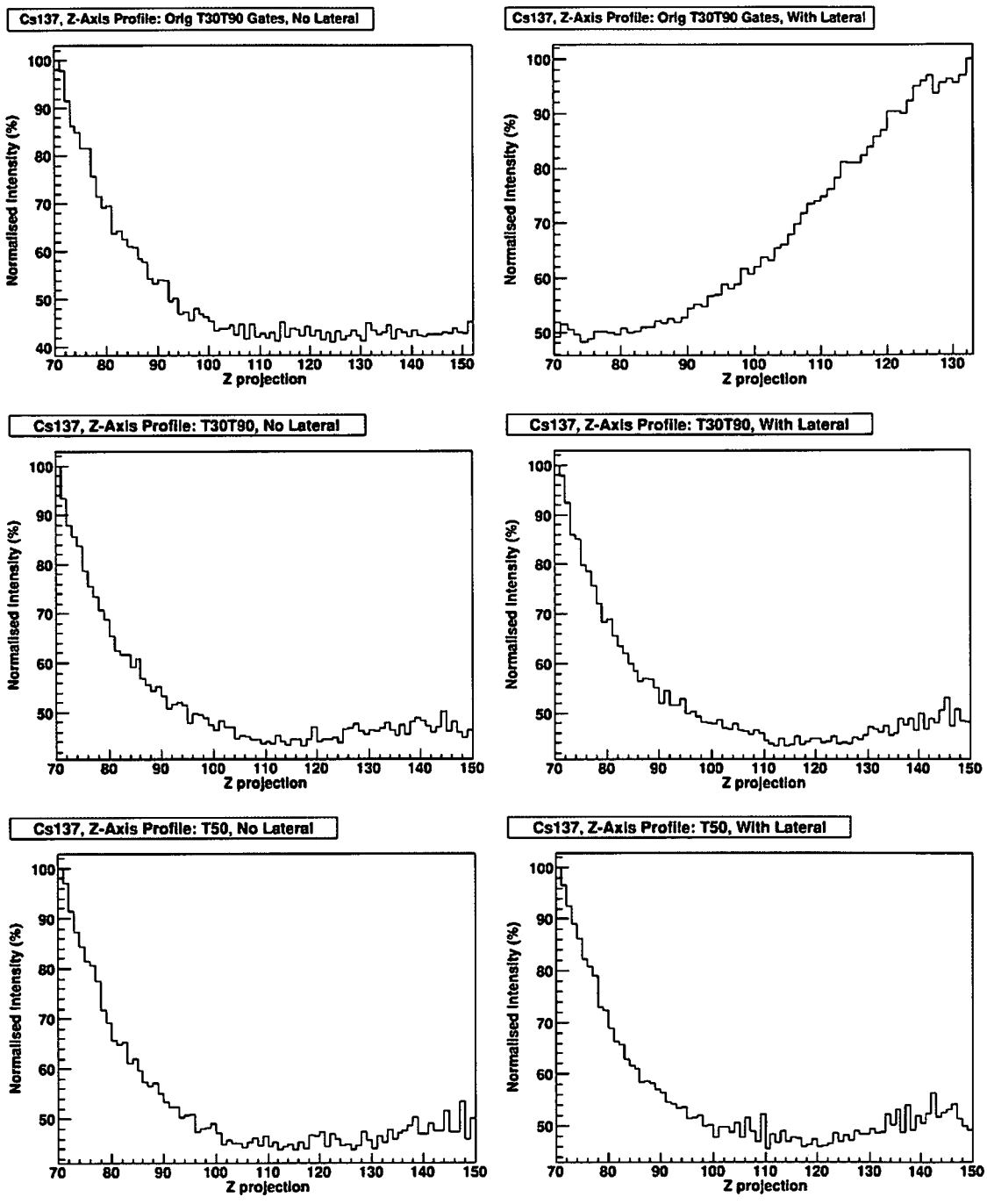

Figure 7.23: Distributions used to determine the localisation of the source along the z axis. The distributions are created by calculating the ratio of the highest number of counts in one element of a plane to the sum of the total counts in that same plane, for each of the two hundred planes. The source was estimated to be around z plane 105 from experimental measurement. The distributions show no discernible increase in intensity around the expected region from any of the reconstructions.

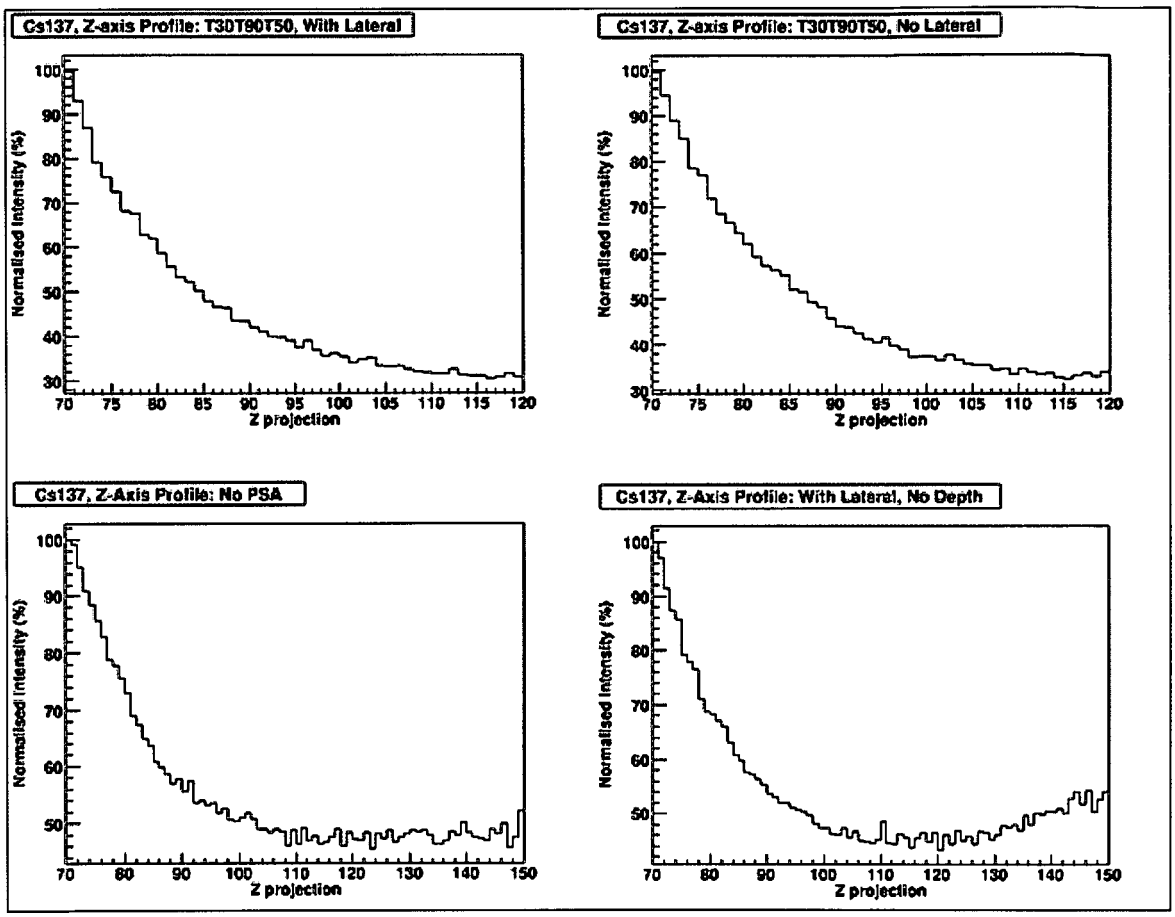

Figure 7.24: Distributions used to determine the localisation of the source along the z axis. The source was estimated to be around z plane 105 from experimental measurement. The distributions show no discernible increase in intensity around the expected region from any of the reconstructions.

PSA Gates	FWHM X	FWHM Y	FWTM X	FWTM Y	Average FWHM	Average FWTM
Orig T30T90 No Lat	23	25	138	135	24	136.5
T30T90 With Lat	32	35	57	95	33.5	76
T50 No Lat	40	30	113	90	35	101.5
Orig T30T90 With Lat	39	34	112	87	36.5	99.5
T30T90 No Lat	45	30	117	95	37.5	106
No PSA	37	40	101	90	38.5	95.5
T30T90T50 With Lat	43	35	103	111	39	109
T30T90T50 No Lat	42	38	108	117	40	112.5
Lateral No Depth	46	35	107	90	40.5	98.5
T50 With Lat	43	40	107	90	41.5	98.5

Table 7.3: Table of resolutions measured from the reconstruction of a ^{137}Cs point source positioned at 33 mm from the scatter detector with a detector separation of 52 mm. The gates used have been listed in order of best average FWHM from top to bottom. Units are millimeters.

Based on the FWTM, the best average resolution was from the T30T90 gates with lateral PSA applied, obtaining a position resolution of 76 mm. No z localisation at all could be seen for this data set.

Chapter 8

Summary and Future Prospects

8.1 Summary

Four principle aims of this work were outlined in Chapter One:- to improve the 4 mm localisation of a photon interaction through the depth, to quantify the effect of any improved depth localisation on image quality, to collect Compton camera data at low photon energies by the introduction of a thin, double sided silicon strip detector (DSSSD) and to evaluate the performance of the system based on the experimental measurements taken and analysis performed. The steps taken in order to realise these targets involved SmartPET 1 characterisation, collection and imaging of Compton camera data using the two SmartPET detectors, characterisation of a DSSSD, integration of the DSSSD into the Compton camera system and subsequently the collection and image reconstruction of Compton camera data using the DSSSD and SmartPET 1.

8.1.1 SmartPET Characterisation

Prior to this work, the position sensitivity of a γ-ray interaction in the SmartPET detector could be located to a $1\times1\times4\,\mathrm{mm}^3$ volume. The initial objective was to improve the sensitivity through the depth by locating the interaction position to within

1 mm as opposed to 4 mm. By performing a finely collimated scan over the side of the detector (corresponding to the depth) the pulse shape response of the interaction was used to assign its distance from the collecting contacts. Two methods were investigated; the constant fraction (T30T90) method and the T50 time difference method. The T30T90 time difference method proved to be the most successful at achieving 1 mm sensitivity through the depth, localising almost 20 percent of incident photons to within 1 mm when using the DC response.

It was observed that the sensitivity of both methods degrades toward each of the faces. For the AC response the sensitivity near the DC face was particularly bad, typically offering between 7 and 8 mm sensitivity, whereas the DC response was good (usually 1 mm sensitivity) all the way up to the face. It was also observed that the response from the DC face allowed smaller risetime gates to be created than the AC face i.e. the DC face was more sensitive. It is thought that this difference is due to the possibility the the SmartPET detector is not at saturation voltage, which will effect the transport of the holes to the AC face to a greater degree than the electrons to the DC face.

It was observed that the pulse shape response differs toward the edges of the detector, possibly due to a changing electric field toward the edges of the crystal. A 7 mm detector guard ring was put in place around to the active area in an attempt to maintain the electric field uniformity and avoid edge effects (i.e. different responses at the edges of the detector due to differing electric field). The area defined by the outer two strips in the active volume produced a response different from that observed in the centre strips implying that a guard ring of 7 mm width is not sufficient. It is recommended that any further planar germanium strip detectors have the equivalent of a 17 mm wide guard ring (10 mm from the two edges strips and the current 7 mm guard ring) or be prepared to provide individual characterisation for strips in this region.

8.1.2 SmartPET Compton Imaging

Images of both a ^{137}Cs point source and a ^{22}Na source have been created using gates constructed from risetime parameters derived from the pulse shape response of the detector. A back projection reconstruction algorithm was applied to data acquired from the SmartPET Compton camera. The optimum PSA was determined in each dimension, where the position resolution of the image was evaluated in terms of FWHM and FWTM in the xy plane and in terms of FWHM, FWTM and FWTQM in the z plane. It was found that in the xy plane, the PSA analysis providing the best position resolution for the ^{137}Cs point source was using the T30T90 gates determined in Chapter Four for the depth localisation, without any PSA for the lateral localisation. This provided an average FWHM of 18.5 mm in the xy plane. In the z dimension, it was shown that the original T30T90 gates (4 mm sensitivity) provided the best resolution, with a FWTQM of 17 mm and a FWHM of 37 mm. When imaging the ^{22}Na distributed line source it was seen that the application of PSA does not improve the image obtained from the reconstruction in any of the 3 dimensions. It is not clear why this is the case, as the application of PSA to the ^{137}Cs point source data improved the localisation of the source. A higher number of statistics may be required as only 50 K events were used, compared to 30 K for the point source. It is also possible that complications in the reconstruction can occur due to the distributed nature of the source. This is manifested in the form of an increased possibility of false intersections, as cones from different regions of the source will form an overlap with each other more often than if they were emitted from a single point. The presence of a higher 1274 keV energy γ-ray also has the potential to complicate the reconstruction, as scatters from these photons could potentially be present in the 511 keV addback peak, creating false cones and degrading the image. It would be of interest to observe the images produced by utilising the higher energy 1274 keV γ-rays which would not suffer from this effect.

For both sets of images it was shown that the application of the lateral PSA degraded the position resolution of the reconstruction. This is contrary to expectations and further investigation is required.

8.1.3 DSSSD Characterisation

It was evident from previous work [Gil06] that the 20 mm thickness of the SmartPET detector was too great to allow γ rays with energies much lower than 300 keV to scatter through to the absorber detector. This prompted the introduction of a double sided silicon strip detector (DSSSD) which, as it was both thinner and less dense than the SmartPET germanium detector, should facilitate the Compton scatter of photons to the absorber detector. The DSSSD and its associated electronics were designed for higher energy charged particle detection, and as such the noise present (generally between 30 to 40 keV) was too large to allow scatters of photons with energies comparable to those used in medicine (141 keV) to be detected. This high level of noise also proved to be prohibitive in the search for transient charges in adjacent strips, making the application of lateral PSA to refine the location of an interaction within a strip impossible.

8.1.4 DSSSD/SmartPET Compton Imaging

The DSSSD was integrated to the Compton camera system as a scatter detector, with SmartPET 1 as the absorber detector. Analogue electronics were used in conjunction with the DSSSD as no PSA could be applied, making the need for digital electronics in conjunction with the DSSSD unnecessary.

Two data sets were collected, one using a ^{152}Eu point source and the other using a ^{137}Cs point source. Reconstructions were created for each of the data sets using each combination of PSA applied to SmartPET 1. When considering the images in the xy plane from the ^{152}Eu source, it was found that the PSA that achieved the

finest resolution, both FWHM and FWTM, was the T30T90 gates with no lateral PSA applied. The 344 keV γ-rays from ^{152}Eu were used in the reconstruction. The values of the resolutions were 54 mm for the FWHM and 130 mm for the FWTM. No quantification of the localisation performance could be made along the z axis due to poor statistics and the lack of a Gaussian shape. From the reconstructions of the ^{137}Cs source the optimum PSA to be applied differed depending on whether FWHM or FWTM resolution parameters were chosen. For the FWHM parameter, the original T30T90 gates with no lateral PSA applied were the best performing gates, achieving an average resolution of 24 mm. Based on the FWTM, the best average resolution was from the T30T90 gates with lateral PSA applied, obtaining a resolution of 76 mm. No z localisation at all could be seen for this data set which is suspected to be a result of low statistics.

8.2 Future Work

8.2.1 SmartPET Characterisation

The characterisation of SmartPET through depth was performed by scanning a highly collimated beam of photons over the side of the detector. The most common interaction of 662 keV γ rays with germanium is Compton scattering. The fold 1 requirement potentially removes a great deal of the scattering, however it is still possible for Compton scattering to occur within the volume defined by a strip on each face, thus fulfilling the fold 1 requirement whilst still undergoing a Compton scatter. This type of event will cause a discontinuity on the leading edge of the pulse [Scr07] and yield risetimes uncharacteristic of an absorption interaction at that position. One solution to this problem for future detector characterisation would be to be perform a coincidence scan, discussed in Chapter Four.

The reconstructions provided some unexpected results with respect to the application of PSA to the Compton camera data. In all cases, the application of lateral PSA, which utilises the transient charges observed in neighbouring strips to localise the position of interaction within a strip, degraded the measured resolution of the image. As the positions of interaction are necessary to position the reconstruction cone which will contribute to the location of the source, it is unlikely that this knowledge, if correct, would degrade the image. It is probably the case that the boundaries of the asymmetry distribution (discussed in Chapter Three) which determine the lateral position of interaction and were created during the original characterisation are not correct. It would be advisable to check that these parameters still represent the correct areas of the asymmetry distribution for each of the strips and recalculate if necessary, prior to any further work requiring lateral PSA in the SmartPET detectors.

8.2.2 SmartPET Compton Imaging

This work has demonstrated Compton imaging for a ^{137}Cs point source and a ^{22}Na distributed line source. Analysis was only conducted for each of the sources in a single position and orientation and the detectors at a fixed separation. It was briefly mentioned in Chapter Two that the geometry of the system, i.e. the source to detector distance and the detector separation, can affect the angular uncertainty of the system. For a more complete evaluation of the imaging performance of the SmartPET Compton camera imaging, data would need to be analysed from different system geometries.

The ability of the system to resolve two point sources has not been investigated. It would be desirable to be able to quantify how close two sources can be and still be resolved from each other.

It was suggested that potential problems were occurring in the ^{22}Na reconstructions due to the presence of a higher energy γ ray (1274 keV). It is not known how much of an effect this contributed to the final image, however this should be quantified when

implementing a future study involving multiple energies.

It was observed that a higher resolution image was produced when no PSA was applied to the ^{22}Na data set. This is contrary to what was expected. It has already been mentioned that he lateral PSA does not seem to be effective and work must be done to investigate, and hopefully correct, this aspect of the PSA. What is surprising is that no method to localise the position of interaction through the depth improved the image as it did for the point source. As the line source is distributed, it is suggested that a greater number of events would be needed to provide an image comparable to the point source. Although more events were used (50 K for the line source as opposed to 30 K for the point source) it is likely that many more would need to be included to conduct a more rigorous test of the PSA with respect to the imaging of a distributed source. It may be that the higher energy 1274 keV γ ray would provide a more positive response to the application of PSA. This investigation was prohibited in this due to time constraints both in acquisition time and analysis/reconstruction time.

8.2.3 Implementation of a DSSSD

Silicon remains the semiconductor material of choice for low energy Compton camera imaging due to both its reduced Doppler broadening contribution and its increased likelihood of the low energy photons undergoing a Compton scatter interaction rather than photoelectric absorption. It is recommended that any future detector and its associated preamplifiers should be designed to exhibit extremely low noise characteristics, low enough to allow the small energies (approximately a few keV - see Table 7.1 in Chapter Seven) deposited from Compton scatters of photons in the energy region of the 141 keV photons currently used in SPECT scans. A further benefit of a low noise DSSSD would be an investigation into the presence of transient charges in strips adjacent to the hit strip, and whether they can be utilised to refine the position of interaction beyond that of the hit strip's width.

8.2.4 DSSSD/SmartPET Compton Imaging

In terms of the imaging, very little can be gained from the work presented in this thesis. The detector and preamplifiers were completely unsuitable for low energy Compton imaging. It could not image energies any lower than when the SmartPET detector was implemented as a scatter detector, because these lower energies did not deposit enough energy during a Compton scatter to trigger the system. In addition, the poor efficiency for Compton scatters of the higher energy photons lead to a low number of events (approximately 5 K) available for reconstruction. It was not possible to obtain higher statistics in the allotted time frame as the count rate was so low.

The ultimate goal of the Compton camera with respect to medical imaging, is to improve on the current systems in place to perform SPECT. This requires a high resolution image collected in a relatively short time. In order to achieve this, the Compton camera system must possess low uncertainty in the measurements and be highly efficient. Problems can arise when seeking these targets. For example, a large separation in the scatter and absorber detector provides a reduced angular uncertainty, however this larger separation will inevitably result in diminished efficiency, and vice versa. The choice of scatter detector is extremely important, as it is responsible for determining the angle of scatter and favouring Compton scattering for the incident photons. It must also be able to locate the position of interaction to a high degree of accuracy.

There exists a large number of variables which must be optimised in order for any particular Compton camera to be successful. Any Compton camera will be specific to the particular situation it is intended to be employed in, potentially placing emphasis on certain variables above others e.g. energy of the photons to be imaged, time available for imaging, degree of image resolution required, etc. The only realistic way of addressing all of the variables and determining the optimum Compton camera system for specific application is by performing Monte Carlo simulations. Future work

should involve imaging from data produced by simulations of different Compton camera systems to evaluate which arrangement is most suited to the individual imaging requirements. Simulations will allow the factor most detrimental to the image quality to be identified (e.g. Doppler broadening from the scatter detector material, energy resolution of the scatter detector, position of interaction sensitivity, system geometry) allowing the best system within the given constraints to be identified.

Bibliography

[Amm00] M. Amman and P.N. Luke *et.al*, *Three-dimensional position sensing and field shaping in orthogonal-strip germanium gamma-ray detectors*, NIM A452 (2000) 155-166

[Amp08] http://www.amptek.com/a250.html

[Ang58] H.O. Anger, *Scintillation Camera*, Review of Scientific Instrumentation, Vol 29, p. 27 - 33, (1958)

[Bos06] *Orthogonal Strip HPGe Planar SmartPET Detectors in Compton Configuration*, H.C. Boston *et al*, Nuclear Science Symposium Conference Record, 2006. IEEE Volume 6, Oct. 29 2006-Nov. 1 2006 Page(s):3884 - 3887

[Bos09] *Characterisation of the first SmartPET planar germanium detector*, H.C. Boston-Scraggs *et.al*, In preparation, NIM A.

[Coo07] R.J. Cooper,*Performance of the SmartPET Positron Emission Tomography System for Small Animal Imaging*, PhD Thesis 2007, Department of Physics, University of Liverpool, UK

[Dav52] *Gamma-Ray absorption Coefficients Reviews Modern Physics*, C.M. Davisson and R.D. Evans Vol 24, No.2. p. 82 - 94, (1952)

[Dav07] DSSSD detector loaned to Liverpool's Department of Physics by Tom Davinson, School of Physics and Astronomy, The University of Edinburgh, September 2007 - April 2008

[Des02] M. Descovich *et al.*, Nucl. Inst. Meth. **A553** (2005) 535

[Geo93] *Digital Pulse Processing in High Resolution, High Throughput Gamma-Ray Spectroscopy*, U. Georgiev, and W. Gast, IEEE Transactions on Nuclear Science, (1993) Vol. 40, No.4, p. 770-779.

[Gil06] *Development of Electronic Collimation for Nuclear Imaging*, J. Gillam, PhD Thesis 2006, School of Physics, Monash University, Australia

[Fan47] U. Fano Phys. Rev. 72 (1947), 26

[Kno00] G.F. Knoll, *Radiation Detection and Measurement*, John Wiley and Sons (1989)

[Kro99] R.A. Kroeger *et al.*,*Charge spreading and position sensitivity in a segmented planar germanium detector*, NIM A422 (1999) 206-210.

[Laz01] I.H. Lazarus *et al.*, IEEE Transactions on Nuclear Science **48** 567 (2001)

[Laz04] I.H. Lazarus *et al.*, IEEE Transactions on Nuclear Science **NS-51**, 4, 1353.(2004)

[Leo93] W.R Leo *Techniques for Nuclear and Particle physics experiments* (1993), Ch2 p37

[Lie01] R.M. Lieder *et al.*, *The TMR network project: Development of ã-ray tracking detectors*, Nuc. Phys. A 682 (2001) 279c-285c.

[Los05] A.S. Hoover *et al. Performance of the Los Alamos Compton Gamma-ray Imager*, Los Alamos National Laboratory, IEEE 2005 NSS Conference

[Mat06] A.R. Mather *Evaluation of the Planar Germanium SmartPET system for use in Positron Emission Imaging*, PhD Thesis 2006, Department of Physics, University of Liverpool, UK

[Mic09] http://www.micronsemiconductor.co.uk/

[Mih04] L. Mihailescu *et al.*, *SPIER: A Ge Compton Camera*, Lawrence Livermore National Laboratory, (2004)

[Ord98] C. Ordonez *et al. Doppler Broadening of Energy Spectra in Compton Cameras*, Dept. of Medical Physics, St Luke's Medical Centre, IEEE Trans Nucl Sci, (1998), p1361 - 1365

[Ord99] C. Ordonez *et al. Angular uncertainties due to geometry and spatial resolution in Compton cameras*, Dept. of Medical Physics, St Luke's Medical Centre, IEEE Trans Nucl Sci, (1999), vol. 46,

[Oxl09] D.C. Oxley, Private communication of GEANT 4 SmartPET sidescan simulations, University of Liverpool, (2009)

[Peh69] R.H. Pehl and F.S. Goulding, *UCRL* **19530**, 333 (1969)

[Rad88] V. Radeka, Ann, Rev. Nucl. Part. Sci 38, 224 (1988)

[Ram39] S. Ramo *Currents induced by electron motion*, Proceedings of the I.R.E, September 1939, p. 584

[ROO07] ROOT Analysis Package, http://root.cern.ch/drupal/

[Scr07] D.P. Scraggs, Digital Signal Processing Techniques for Semiconductor Compton Cameras, PhD Thesis 2007, Department of Physics, University of Liverpool, UK

[Sho38] W. Shockley *Currents to conductors induced by a moving point charge*, J. Appl. Phys. 9 (1938) 635

[Sin83] M. Singh and D. Doria, *An electronically collimated gamma camera for single photon emission computed tomography. Part 1: Theoretical considerations and design criteria*, Med. Phys, Vol 10, No.4. P421 - 427, (1983)

[Sze01] S.M. Sze *Semiconductor Devices, Physics and Technology*, 2nd Edition (Wiley 2001), Chapter 2 P33

[Tod74] R.W. Todd, J.M. Nightingale and D.B. Everett *A proposed gamma cammera*, Nature 251, 132 - 134, (1974)

[Tur06] G.H.B Turk, The characterisation of the first SmartPET HPGe planar detector, PhD Thesis 2006, Department of Physics, University of Liverpool, UK

[Tho90] S.L. Thomas, Nuclear Instruments and Methods in Physics Research **A288** 212 - 218 (1990)

[Vet00] K. Vetter, NIM A 452 (2000) 223

[Web88] S. Webb *The Physics of Medical Imaging*, (Wiley 1988)

[Wer04a] M. Wernick and J. Aarsvold *Emission Tomography: The Fundamentals of PET and SPECT*, (Dawson Books 2004), Ch2 P84

[Wer04b] M. Wernick and J. Aarsvold *Emission Tomography: The Fundamentals of PET and SPECT*, (Dawson Books 2004), Ch7 P150

[Wul02] E.A. Wulf *et al*, Transactions on Nuclear Science, 2002. IEEE Volume 49, No.4, Aug. 29 2002 Page(s):1876 - 1880

[Zog03] A. Zoglaur an Gottfri Kanbah, *Doppler Broadening as a Lower Limit to the Angular Resolution of Next Generation of Compton Telescopes*, SPIE Vol. 4851 (2003)

[Zul70] H.R. Zulliger and D.W. Aikten, *IEEE Trans. Nucl. Sci.* **NS-17**(3), 187 (1970)